The present work was submitted to the Institute of Applied Mechanics (IFAM)

Rheinisch-Westfälische Technische Hochschule Aachen (RWTH)

Master's Thesis

Gradient-Extended Damage Modeling Of Heterogeneous Microstructures Using The Fast Fourier Transforms Method

---

Author:
Jaeyong Jung

Supervisor:
Prof. Roger A. Sauer Ph.D.
Prof. Dr.-Ing. Stefanie Reese

A thesis submitted in fulfilment of the requirements
for the degree of M.Sc.

in the

Department of Civil and Environmental Engineering
Institute of Applied Mechanics (IFAM)

Aachen, 1. March, 2018

Rheinisch-Wesfälische Technische Hochschule Aachen (RWTH)

Abstract

Faculty Name
Institute of Applied Mechanics (IFAM)

M.Sc.

Gradient-Extended Damage Modeling Of Heterogeneous Microstructures Using The Fast Fourier Transforms Method

by Jaeyong Jung

In the last decades, fiber reinforced composites have gained popularity in the applications of light-weight designs. Inside composites, fibers are aligned in a certain direction for reinforcement, and matrix material surrounds the fibers. It is advantageous that the composite has high stiffness and yield strength compared to its weight. That is because those fibers are stronger than matrix materials, and they carry mechanical loads in that certain direction. On the other hand, that composite is weak in directions orthogonal to that direction for reinforcement since matrix material is loaded mostly in that case. Consequently, the mechanical response of such composites should be investigated before the composites are applied in real engineering applications. Since experimental studies of composites are costly and take much time to manufacture specimens, a fast numerical method is required as an alternative option. Thus, the aim of this research is to develop a numerical method to predict the mechanical response of composites containing cylindrical inclusions. In this work, the Fast Fourier Transform-based (FFT-based) homogenization method of Moulinec and Suquet [1] is introduced. Also, the reformulated FFT-based scheme for large deformation problems by Eisenlohr et al [2] is discussed and chosen for the current research. To predict a mechanical failure, the thermodynamics framework is used to derive the isotropic damage model. In order to circumvent the ill-posedness of the local continuum damage model, the gradient-extended damage model based on the micromorphic approach is proposed. After that, coupling schemes to calculate the interaction between the field of local damage variable and that of nonlocal damage variable will be discussed. The simultaneous scheme will be proved to be a not only stable but also fast coupling strategy. Finally, applications of the FFT-based scheme, combined with the gradient-extended damage model and the simultaneous scheme, will be tested on the composites made of cylindrical inclusions, and the result will be analyzed.

Acknowledgements

This thesis for the degree of Master of Science is written during my stay at Institut Für Angewandte Mechanik (IFAM) at RWTH Aachen University under the supervisions of Prof. Roger A. Sauer and Prof. Stefanie Reese. I appreciate the opportunity and technical supports to conduct researches at IFAM. Thanks to the opportunity, I could find and develop my inherent research potentials at most, and I have enjoyed that.

Especially, I would like to thank Julian Kochmann, M. Sc. and Dipl.-Ing. Tim Brepols for answering my various questions arising in the course of the research. They gave me a lot of help to get into the fields of Damage Mechanics and simulation techniques. Definitely, discussions that I had with them were fruitful and helped me to have better understanding in theories. Moreover, their helps made me to shape my own idea as well. At the same time, I would like to appreciate Mr. Axel Mittendorf's technical support for using computing facilities and software when I need him.

Finally, I would like to thank my family for encouraging and supporting me to study abroad. Their supports have led me to overcome difficulties that I had in my life, and without them non of this would have been possible.

Contents

Abstract i

Acknowledgements ii

Contents iii

List of Figures vi

List of Tables vii

Abbreviations viii

Symbols ix

1 Introduction 1
- 1.1 The Object and Scope of the Research 1
- 1.2 Structure of the Paper 2

2 The FFT-based Scheme for Finite Strain Model 4
- 2.1 Kinematics of Deformations 4
- 2.2 The Representative Volume Element and the Periodic Boundary-Value Problem 5
  - 2.2.1 The Concept of Representative Volume Element 5
  - 2.2.2 The Periodic Boundary-Value Problem 6
- 2.3 The Homogenization Technique and Lippmann-Schwinger Equation 7
- 2.4 The Periodic Lippmann-Schwinger Equation in Fourier Space 9
  - 2.4.1 The Formulation of Solution Technique 9
  - 2.4.2 The Reference Material for a Large Deformation Problem 10
  - 2.4.3 The Fast Fourier Transform and Discretization of RVE 11
- 2.5 The Algorithm of the FFT-based Scheme for Inelastic Behaviors 13
- 2.6 The Defects of the Conventional FFT-based Scheme and Remedy 14

3 Damage Mechanics 15
- 3.1 Local Continuum Damage Model 15
  - 3.1.1 Thermodynamics Framework for Isotropic Damage Model 15
  - 3.1.2 Damage Loading Condition 17
  - 3.1.3 Numerics for Damage Variable Calculation 17
  - 3.1.4 Validation of the Implementation of the Local Damage Model 18

3.2 Gradient-Extended Damage Model 20
3.2.1 Micromorphic Approach 21
3.2.2 Extension of Thermodynamics Framework using Micromorphic Approach 23

4 Coupling Schemes **25**
4.1 Introduction of Coupling Schemes 26
4.1.1 Partitioned Approach 26
4.1.1.1 Pros and Cons of the Partitioned Approach 26
4.1.1.2 Staggered Scheme 26
4.1.1.3 Instability of the Staggered Scheme 27
4.1.1.4 Iteratively Staggered Scheme 28
4.1.2 Simultaneous Scheme 29
4.1.2.1 The Reason Why the Simultaneous Scheme Can Be Faster 30
4.2 Combination of the FFT-based Scheme and the Coupling Schemes 31
4.3 Implementations of the Coupling Schemes 32
4.3.1 Staggered Scheme 32
4.3.1.1 Basic Idea 32
4.3.1.2 The Spectral Method to Solve the Micromorphic Balance Equation Defined on a RVE 33
4.3.1.3 The Return-Mapping Algorithm for the Nonlocal Damage Model 33
4.3.1.4 The Algorithm 34
4.3.2 Iteratively Staggered Scheme 34
4.3.2.1 Basic Idea and Algorithm 34
4.3.3 Simultaneous Scheme 36
4.3.3.1 Basic Idea 36
4.3.3.2 Formulations of the Residual Vector and the Vector of Increments 36
4.3.3.3 Application of the Newton-Raphson Method 38
4.3.3.4 Calculations of the Residual Vector and the Jacobian Matrix 39
4.3.3.5 Application of a Sparse Matrix Form and the Schur Complement Method 42
4.3.3.6 The General Case of a Damage Evolution 44
4.3.3.7 The Choice of an Iterative Solver 45
4.3.3.8 The Algorithm of Simultaneous Scheme 45
4.4 Validations of the Implementations of the Coupling Schemes 46
4.4.1 Comparison of the Results 47
4.4.2 The Reason Why the Partitioned Approaches Are Slow 49

5 Numerical Examples **51**
5.1 Parametric Studies of the Local Damage Model 51
5.1.1 Effect of the damage parameter r 52
5.1.2 Effect of the exponential damage parameter s 52
5.2 Problem of a Single Inclusion 53
5.2.1 Local Damage Model 55
5.2.2 Nonlocal Damage Model 56
5.3 Problem of Multiple Inclusions 58
5.3.1 Uniaxial Stretch in X-Direction 59

5.3.1.1 Stress Curves 59
5.3.1.2 Fractured Configurations 61
5.3.2 Uniaxial Stretch in Y-Direction 63
5.3.2.1 Stress Curves 63
5.3.2.2 Fractured Configurations 65
5.3.3 Shear Deformation 67
5.3.3.1 Stress Curves 67
5.3.3.2 Fractured Configurations 69

6 Conclusions **71**
6.1 Summary of Major Investigations 71

A The Sparse Matrix Format **73**

Bibliography **75**

List of Figures

1.1 Visualizations of a composite with a cylindrical inclusion. 1

2.1 Microstructure and its RVE. 6

3.1 Comparison between the results of the nonlinear solver using MATLAB and the implementation of algorithm (2) in the FFT-based scheme. 20

4.1 Stencil of the central finite difference scheme (4.20). 40
4.2 Blue dots represent nonzero entities in the Jacobian matrix $\frac{d\boldsymbol{r}}{d\boldsymbol{x}}$ in equation (4.17). Each submatrix in a quadrant corresponds to $\frac{\partial \boldsymbol{r}_1}{\partial \Delta \boldsymbol{\lambda}}$, $\frac{\partial \boldsymbol{r}_1}{\partial \Delta \bar{\boldsymbol{D}}}$, $\frac{\partial \boldsymbol{r}_2}{\partial \Delta \bar{\boldsymbol{D}}}$, and $\frac{\partial \boldsymbol{r}_2}{\partial \Delta \boldsymbol{\lambda}}$. 42
4.3 Comparison between the solution of the local damage model and that of the nonlocal damage model with different coupling schemes. 48
4.4 The iteratively staggered scheme takes up the largest amount of runtime. The simultaneous scheme is the fastest one among those coupling schemes. . . 49

5.1 The influence of r on the effective material response at fixed Y_0 and s. . . . 52
5.2 The influence of s while Y_0 and r are fixed. 53
5.3 Visualizations of an RVE with a cylindrical inclusion. 54
5.4 Simulations of the local damage model with different discretization. 55
5.5 Fractured configurations of the local damage model. There are 32×32, 64×64, 128×128, and 256×256 grid points in each quadrant. The contour interval of the damage variable is 0.2. 56
5.6 Simulations of the nonlocal damage model with different discretizations. . . 57
5.7 Fractured configurations of the nonlocal damage model. There are 32×32, 64×64, 128×128, and 256×256 grid points in each quadrant. The contour interval of damage variable is 0.2. 58
5.8 Visualizations of RVEs with multiple cylindrical inclusions. 58
5.9 The effective response of the damage models under the uniaxial stretch in x-direction. 60
5.10 There are 64×64, 128×128, and 256×256 points in each quadrant. The principal stretch is 1.02. The contour interval of the damage variable is 0.2. . 62
5.11 The effective response of the damage models under the uniaxial stretch in y-direction. 64
5.12 There are 64×64, 128×128, and 256×256 points in each quadrant. The principal stretch is 1.02. The contour interval of the damage variable is 0.2. . 66
5.13 The effective response of the damage models under the shear deformation. 68
5.14 There are 64×64, 128×128, and 256×256 points in each quadrant. The principal stretch is 1.02. The contour interval of the damage variable is 0.2. . 70

List of Tables

2.1 RVE's properties as 3D grid. 12

3.1 Material parameters for elastic-damage model 19

4.1 Field quantities and equations at each step in algorithm 3 28
4.2 Submatrices of the Jacobian matrix $\frac{d\boldsymbol{r}}{d\boldsymbol{x}}$. 41
4.3 Similarities between equations (4.16) and (4.28). 43
4.4 Modifications of terms when an elastic-loading takes place at a grid point, (i, j, k). 44
4.5 Elastic-damage material parameters 47
4.6 The runtime of simulations with different schemes. 48

5.1 Elastic-damage material parameters 51
5.2 Elastic-damage material parameters 54

A.1 The representation of the matrix B in the CSR format. 74

Abbreviations

RVE	**R**epresentative **V**olume **E**lement
FEM	**F**inite **E**lement **M**ethod
FEA	**F**inite **E**lement **A**nalysis
FFT	**F**ast **F**ourier **T**ransforms
KKT	**K**arush **K**uhn **T**ucker
CSR	**C**ompressed **S**parse **R**ow
CSC	**C**ompressed **S**parse **C**olumn

Symbols

$\boldsymbol{X}$	initial position vector
$\boldsymbol{x}$	current position vector
$\boldsymbol{u}(\boldsymbol{x})$	displacement of grid point at position $\boldsymbol{x}$
$\tilde{\boldsymbol{u}}(\boldsymbol{x})$	fluctuation field of displacement at position $\boldsymbol{x}$
Div	divergence operator in a reference configuration
$\mathbf{I}$	second-order identity tensor
$\mathbb{C}^0$	reference material's stiffness tensor
$\mathbb{C}(\boldsymbol{x})$	local stiffness tensor at position $\boldsymbol{x}$
$\mathbf{G}^0$	acoustic tensor
$\mathbf{F}$	deformation gradient tensor
$\mathbf{F}_0$	macroscopic deformation gradient tensor
$\mathbf{P}$	first Piola-Kirchhoff stress tensor
$\mathbf{S}$	second Piola-Kirchhoff stress tensor
$\mathbf{E}$	Green-Lagrangian strain tensor
$\mathbf{C}$	right Cauchy-Green deformation tensor
$\mathbf{H}$	displacement gradient
$\tilde{\mathbf{H}}$	fluctuation field of displacement gradient
i	complex number
N_x, N_y, N_z	the number of grid points in each direction
N_x, N_y, N_z	length of a RVE in each direction
dx, dy, dz	grid spacing in each direction
D	damage variable
r, s	damage hardening parameters
$f(D)$	damage function
Y, q_d	thermodynamic conjugate forces to damage and damage hardening

Y_0	initial damage threshold
g_{int}	internal virtual work
g_{ext}	external virtual work
$\bar{D}$	nonlocal damage variable
H	penalty term
A	parameter of the influence of the gradient in a material
$\mathbf{J}$	Jacobian matrix
r_1	residual of the micromorphic balance equation
r_2	residual of the damage loading function
$\boldsymbol{\epsilon}$	small strain tensor
$\boldsymbol{\sigma}$	Cauchy stress tensor
$\boldsymbol{\tau}$	polarization stress field over a RVE
Ω	domain of a RVE
Ω_0	reference configuration
$\mathbb{\Gamma}^0$	Green operator
Λ, μ	Lamé constants
Λ_0, μ_0	reference material's Lamé constants
$\boldsymbol{\xi}$	wave vector
Ψ	Helmholtz free energy potential
ξ	damage hardening variable
ϕ_d	damage loading function
λ	damage multiplier
α	internal length scale
∇^2	Laplacian

I would appreciate my family for their endless love, support and encouragement throughout my life. Especially, this humble thesis is dedicated to my mother for her dedication.

Chapter 1

Introduction

1.1 The Object and Scope of the Research

The aim of the research is to develop a numerical technique to predict the mechanical response of a composite, made of a matrix material and cylindrical inclusions. The composite with cylindrical inclusions is the interest of the current research because this kind of geometry is widely used in designs of composites, e.g. Fiber-Reinforced Polymers. An example of that composite's microstructure containing a single cylindrical inclusion is shown in Figure 1.1

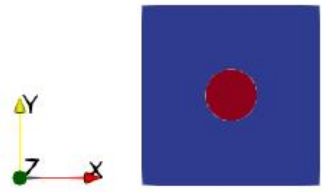

(A) A composite having a cylindrical inclusion in -Z direction.

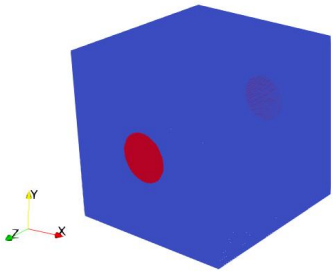

(B) Wireframe model of the composite.

FIGURE 1.1: Visualizations of a composite with a cylindrical inclusion.

In general, the materials of inclusions are more stiff and durable than matrix materials. Those inclusions are installed inside the matrix in the direction of reinforcement depending on the purpose of engineering design. This makes the composite more stiff and durable in the inclusion's direction. On the other hand, that composite is weak at shear deformations and deformations in the direction orthogonal to a direction of inclusions. That is because matrix materials surrounding fibers carry mechanical loads in this case. Consequently, when a composite goes through processes of large deformation in the weak directions, it is likely

to fail. Thus, the mechanical strength of a composite in the orthogonal direction should be investigated before an engineering design is carried out. In order to predict the mechanical strength of a composite, the aim of the current research is focused on the investigations of an elastic-damage behavior of the composite under uniaxial stretch in the orthogonal direction to cylindrical inclusions.

The difficulty of solving the problem of a composite arises from the fact that different material phases are distributed inside a composite. Because of this, numerical methods are preferred over analytical methods. H. Moulinec and P. Suquet proposed the scheme making use of the Fast Fourier Transforms (FFT) to solve a mechanical problem under the periodic-boundary condition, [1]. This method avoids difficulties in meshing. Instead, this method requires a discretization on a grid of regular spacing. Formulations of stiffness matrix are unnecessary and those are replaced by iterative procedures of the forward and backward FFT operations using the Green operator. The iterative procedure solves the momentum balance equation in Fourier space to estimate a deformation gradient at each grid point. By letting state variables of irreversible processes to be updated after deformation gradients are updated, inelasticities of solid can be calculated. In summary, the FFT-based scheme has the advantage in the process of discretization and is easy to be implemented with inelastic material behaviors. The FFT-based scheme is chosen as the numerical platform of the current research.

In the case of large deformations taking place, there are several nonlinear and inelastic material behaviors involved in a composite, such as a process of damage evolution or plastic deformations. Since most of the mechanical responses of brittle materials can be represented using an isotropic elastic-damage model, for the sake of simplicity, an isotropic elastic-damage model is used for defining constitutive laws of a matrix material and inclusions. As an inelastic behavior is likely to occur when a material goes through a process of large deformation, a constitutive law of a material is constructed based on a finite strain model in this paper. Therefore, the scope of the research is a mechanical boundary-value problem of a composite under the process of elastic-damage loading.

1.2 Structure of the Paper

This paper is organized as follows. Chapter 2 gives the fundamental understanding of kinematics of the finite strain model for the FFT-based scheme. The concept of Representative Volume Element (RVE) is introduced to represent a microstructure of a composite easily. The homogenization techniques and the procedure of formulating the algorithm of the FFT-based scheme are introduced. The mathematical descriptions in Chapter 2 are taken from papers written by P. Eisenlohr et al [2] and M. Kabel et al [3]. Chapter 3 presents

the thermodynamics framework of damage models. The basic idea of the local continuum damage model is introduced. On top of that, the concept of the thermodynamics framework is extended using the micromorphic approach to construct a gradient-extended damage model, [4, 5]. The gradient-extended damage model is expected to remedy the ill-posedness of the local continuum damage model. In chapter 4, the backgrounds of the partitioned approaches (staggered scheme and iteratively staggered scheme) and the simultaneous scheme are discussed. Also, the implementations and validations of those schemes are demonstrated. In Chapter 5, parametric studies and numerical examples using the FFT-based scheme with the gradient-extended damage model are presented. At last, the summary of important investigations and remarks are presented in Chapter 6. Moreover, further research topics to improve numerical stability and efficiency of the current research to achieve more realistic simulations are introduced.

Chapter 2

The FFT-based Scheme for Finite Strain Model

In this chapter, the FFT-based scheme to solve the mechanical boundary-value problem defined as a strong form of the momentum balance equation under periodic boundary condition will be discussed. From the macroscopic point of view, a composite can be regarded as homogeneous material when it is composed of much smaller microstructures which are randomly distributed. A Representative Volume Element (RVE) is a volume element of a composite's microstructure which exhibits the same effective response of a real composite at the macroscale. The concept of RVE can be incorporated to reduce the spatial size of a composite at the macroscale to that of an RVE at the microscale. By solving the problem of each RVE, the solution of an entire composite can be attained because a composite can be regarded as a homogeneous material showing the same mechanical response of an RVE. In this context, the FFT-based scheme suggested by Moulinec and Suquet will be introduced, [1]. According to Moulinec and Suquet, the equation of the periodic boundary-value problem can be classified as a problem of the Lippmann–Schwinger equation. With the help of the FFT, the convolution in real space can be easily solved in Fourier space. The formulation of the FFT-based schemed for a finite deformation problem is suggested by P. Eisenlohr et al, [2], and will be employed in this paper.

2.1 Kinematics of Deformations

Kinematics is a mathematical theory to relate the motion and the deformation of a body. At the initial position of a material in the reference configuration Ω_0 where time $t = 0$, the position of a material point is described using the initial position vector $\boldsymbol{X}$. As time goes on, a body may go through a rigid body motion, such as translation or rotation. On top of that,

it is possible for a body to deform. At time t, the position vector $\boldsymbol{x}$ is introduced to express the current position of a material point in the current configuration Ω_t. The current position $\boldsymbol{x}$ can be expressed in terms of the initial position $\boldsymbol{X}$ and time t. The displacement vector $\boldsymbol{u}$ is defined as the gap between the current position vector $\boldsymbol{x}$ and the initial position vector $\boldsymbol{X}$, and it reads as follows:

$$\boldsymbol{u} = \boldsymbol{x} - \boldsymbol{X} \tag{2.1}$$

The deformation gradient $\mathbf{F}$ reads as follows:

$$\mathbf{F} = \frac{\partial \boldsymbol{x}}{\partial \boldsymbol{X}} \tag{2.2}$$

Equation (2.1), leads to $\boldsymbol{x} = \boldsymbol{u} + \boldsymbol{X}$, and

$$\begin{aligned} \mathbf{F} = \frac{\partial(\boldsymbol{u} + \boldsymbol{X})}{\partial \boldsymbol{X}} = \frac{\partial \boldsymbol{u}}{\partial \boldsymbol{X}} + \mathbf{I} = \mathbf{H} + \mathbf{I} \\ \mathbf{H} = \frac{\partial \boldsymbol{u}}{\partial \boldsymbol{X}} \end{aligned} \tag{2.3}$$

where $\mathbf{H}$ is called the displacement gradient. In the case of a finite deformation problem, the Green-Lagrange strain tensor is employed to measure strain quantity. The Green-Lagrange strain tensor is expressed in terms of the deformation gradient and reads as follows:

$$\mathbf{E} = \frac{1}{2}(\mathbf{F}^T\mathbf{F} - \mathbf{I}) = \frac{1}{2}(\mathbf{C} - \mathbf{I}) \tag{2.4}$$

The right Cauchy-Green deformation tensor is also one of strain measurements and it is given by:

$$\mathbf{C} = \mathbf{F}^T\mathbf{F} \tag{2.5}$$

2.2 The Representative Volume Element and the Periodic Boundary-Value Problem

2.2.1 The Concept of Representative Volume Element

In general, material phases are randomly distributed over a composite. As multiple inclusions with different shapes can be included in a composite, it takes enormous amounts of effort and computer memory to represent and save every detail of a composite's microstructure. In order to simplify the representation of a microstructure, it is assumed that there is a volume element that has the same effective mechanical response of a composite at the macroscale. This postulation is valid when the distribution of microstructures in a composite is statistically random enough. This class of volume element at the microscale is called

Representative Volume Element (RVE). The concept of RVE is frequently used in multiscale simulations to make use of a standard microstructure. To give an example, a composite's microstructure made of a periodically distributed RVE is presented in Figure 2.1:

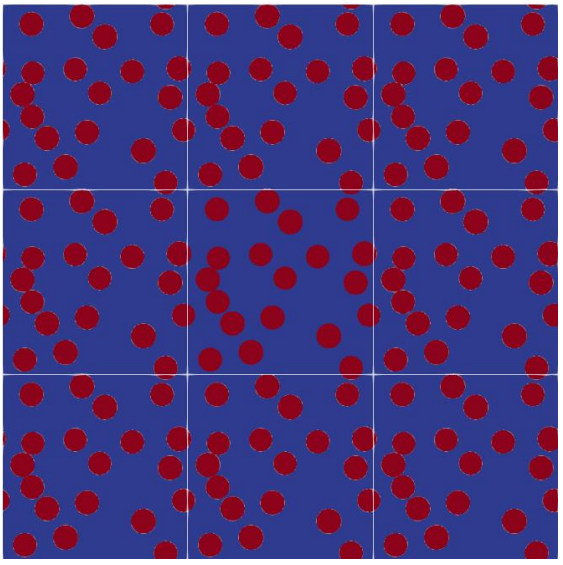

(A) Periodic distribution of 9 RVEs at the microscale.

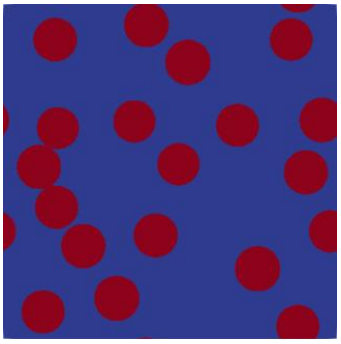

(B) The RVE of a composite at the microscale.

FIGURE 2.1: Microstructure and its RVE.

2.2.2 The Periodic Boundary-Value Problem

The periodic boundary condition on boundaries of an RVE implies that field quantities and the geometry of an RVE are periodically distributed over a composite. From a macroscopic point of view, an RVE seems to be a homogeneous material point with the overall deformation gradient $\mathbf{F_0}$. At the microscale, on the other hand, the overall deformation gradient $\mathbf{F_0}$ is regarded as the average of the deformation gradient field. The deformation gradient field $\mathbf{F}(\boldsymbol{x})$ is expressed in terms of the macroscopic deformation gradient $\mathbf{F_0}$ and a fluctuation field $\tilde{\mathbf{H}}(\boldsymbol{x})$ that arises from the heterogeneities of a microstructure. The deformation gradient field can be expressed as follows:

$$\mathbf{F}(\boldsymbol{x}) = \mathbf{F_0} + \tilde{\mathbf{H}}(\boldsymbol{x}) \tag{2.6}$$

The fluctuation field is given by:

$$\tilde{\mathbf{H}}(\tilde{\boldsymbol{u}}(\boldsymbol{x})) = \nabla_0 \tilde{\boldsymbol{u}}(\boldsymbol{x}) \tag{2.7}$$

The entire displacement field in microscale reads as follows:

$$\boldsymbol{u}(\boldsymbol{x}) = \mathbf{F_0}\boldsymbol{x} + \tilde{\boldsymbol{u}}(\boldsymbol{x}) \tag{2.8}$$

The periodicity of $\boldsymbol{u}$ in microscopic domain implies the following averages over a whole RVE should vanish

$$\begin{aligned} < \tilde{\boldsymbol{u}}(\boldsymbol{x}) >= \frac{1}{\Omega}\int_{\Omega} \tilde{\boldsymbol{u}}(\boldsymbol{x})\, dV = \mathbf{0} \\ < \tilde{\mathbf{H}}(\boldsymbol{x}) >= \frac{1}{\Omega}\int_{\Omega} \tilde{\mathbf{H}}(\boldsymbol{x})\, dV = \mathbf{0} \end{aligned} \tag{2.9}$$

At the microscale, Ω stands for the spatial domain of an RVE. The strong form of the momentum balance equation reads as follows:

$$\operatorname{Div} \mathbf{P}(\boldsymbol{x}) = \mathbf{0} \quad \boldsymbol{x} \operatorname{in} \Omega \tag{2.10}$$

where $\mathbf{P}(\boldsymbol{x})$ stands for the first Piola-Kirchhoff stress tensor. The followings are the summary of equations that should be satisfied in an RVE and at its boundaries

$$\begin{aligned} \operatorname{Div} \mathbf{P} = \mathbf{0} \quad \boldsymbol{x} \operatorname{in} \Omega \\ \mathbf{F} = \mathbf{F_0} + \tilde{\mathbf{H}} \quad \boldsymbol{x} \operatorname{in} \Omega \\ \tilde{\mathbf{H}} \quad \text{periodic} \quad \boldsymbol{x} \operatorname{on} \partial\Omega \end{aligned} \tag{2.11}$$

2.3 The Homogenization Technique and Lippmann-Schwinger Equation

The complexity of the boundary-value problem (2.11) arises from the fact that a field of local stiffness tensor $\mathbb{C}(\boldsymbol{x})$ is varying in the spatial domain of an RVE, Ω. In order to circumvent the difficulty, the homogenization approaches are used to transform the boundary-value problem in a heterogeneous microstructure (2.11) into one in a homogeneous one. The very first idea goes back to Eshelby, [6]. He solved this problem by the means of a simple set of imaginary cutting, straining, and welding operations. The problem of a heterogeneous microstructure, including matrix materials and inclusions, could be split into homogeneous microstructures with the help of the imaginary procedures. Consequently, the transformation of a heterogeneous problem into a homogeneous problem simplified the solution technique. The concept of homogenization was developed further by Dederichs and Zeller, [7], for estimating bounds for the effective elastic constants of polycrystals. An auxiliary problem was formulated in a homogeneous elastic medium in order to take away the local dependence of the stiffness tensor $\mathbb{C}(\boldsymbol{x})$. In this context, the homogenization approach is employed to construct a numerical scheme to find a solution of the boundary-value problem (2.11). The mathematical formulations and descriptions came from the literature [8].

A stress field can be expressed in terms of a homogeneous reference material's constant

stiffness tensor $\mathbb{C}^0$ and the polarization stress $\boldsymbol{\tau}(\boldsymbol{x})$

$$\mathbf{P}(\boldsymbol{x}) = \mathbb{C}^0 : \mathbf{F}(\boldsymbol{x}) + \boldsymbol{\tau}(\boldsymbol{x}) \tag{2.12}$$

By using equation (2.12), the divergence free condition in equation (2.11) is replaced by the following equivalent form:

$$\mathrm{Div}(\mathbb{C}^0 : \mathbf{F}(\boldsymbol{x}) + \boldsymbol{\tau}(\boldsymbol{x})) = 0 \quad \boldsymbol{x} \,\mathrm{in}\, \Omega \tag{2.13}$$

By transferring the divergence of polarization term to the right hand side, the following statements are valid in the spatial domain Ω:

$$\begin{aligned} \mathrm{Div}(\mathbb{C}^0 : \mathbf{F}) &= -\mathrm{Div}(\boldsymbol{\tau}) \quad \boldsymbol{x} \,\mathrm{in}\, \Omega \\ \mathbf{F} &= \mathbf{F_0} + \tilde{\mathbf{H}} \quad \boldsymbol{x} \,\mathrm{in}\, \Omega \\ \tilde{\mathbf{H}} &\quad \mathrm{periodic} \quad \boldsymbol{x} \,\mathrm{on}\, \partial\Omega \end{aligned} \tag{2.14}$$

The mechanical boundary-value problem of a heterogeneous RVE (2.11) is equivalent to the homogenized problem (2.14). The homogenized problem can be interpreted that external body force $\mathrm{Div}(\boldsymbol{\tau}(\boldsymbol{x}))$ is acting on a homogeneous material with stiffness $\mathbb{C}^0$ in Ω while the periodic boundary condition of $\boldsymbol{u}(\boldsymbol{x})$ is fulfilled at the boundaries $\partial\Omega$. In equation (2.14), the divergence of polarization field plays the role of an external body force. As a result, the heterogeneous problem is reinterpreted as a simple homogeneous problem acted on by the external force $\mathrm{Div}(\boldsymbol{\tau}(\boldsymbol{x}))$.

The solution of such problem can be described using the Green's operator $\mathbb{\Gamma}^0$ which is associated to the reference material, [7]. The fluctuation field of the deformation gradient $\tilde{\mathbf{H}}(\boldsymbol{x})$ is expressed using the convolution of the Green's operator with the polarization field

$$\tilde{\mathbf{H}}(\boldsymbol{x}) = -(\mathbb{\Gamma}^0 * \boldsymbol{\tau})(\boldsymbol{x}) \tag{2.15}$$

where the convolution operator denoted by '$*$' is given by:

$$(\mathbb{\Gamma}^0 * \boldsymbol{\tau})(\boldsymbol{x}) = \int_\Omega \mathbb{\Gamma}^0(\boldsymbol{x}, \boldsymbol{y}) : \boldsymbol{\tau}(\boldsymbol{y})\, dV \tag{2.16}$$

The Green's operator $\mathbb{\Gamma}^0$ has a nonlocal character which couples two points $\boldsymbol{x}$ and $\boldsymbol{y}$ at the microscale. By using the equation of the deformation gradient field $\mathbf{F}(\boldsymbol{x})$ in equation (2.6), the solution of the deformation gradient field can be written

$$\mathbf{F} = \mathbf{F}_0 - \mathbb{\Gamma}^0 * \boldsymbol{\tau} \tag{2.17}$$

The class of this problem reduces to the Lippmann-Schwinger equation in elasticity, attributed to Lippmann and Schwinger, [9]. In general, the convolution between two field quantities is not easily calculated in real space. Nevertheless, a convolution term can be easily solved in Fourier space since the convolution operator transforms into scalar products in Fourier space. The above relation (2.17) can be expressed in Fourier space and reads as follows:

$$\hat{\mathbf{F}}(\boldsymbol{\xi}) = -\hat{\mathbb{\Gamma}}^0(\boldsymbol{\xi}) : \hat{\boldsymbol{\tau}}(\boldsymbol{\xi}) \quad \forall \boldsymbol{\xi} \neq \mathbf{0}, \quad \hat{\mathbf{F}}(\mathbf{0}) = \mathbf{F}_0 \tag{2.18}$$

Finally, the original strong form of the equation for a heterogeneous problem (2.10) can be solved using the technique of homogenization and the Fourier transform (2.18).

2.4 The Periodic Lippmann-Schwinger Equation in Fourier Space

The solution of the periodic boundary-value problem in a homogeneous domain (2.14) can be obtained using the Fourier transforms. In this context, the FFT-based scheme was developed by Moulinec and Suquet, [1], to solve the periodic boundary-value problem of a heterogeneous material by means of the homogenization technique. In Fourier space, differential operators of partial-differential equation turn into linear operators so that it makes the problem to be easily solved.

2.4.1 The Formulation of Solution Technique

The field variables of the boundary-value problem described in equation (2.11) are periodic. Considering the fact that the periods of field variables are equal to those of an RVE at the microscale, those field variables can be also expressed in Fourier space. A displacement field $\boldsymbol{u}(\boldsymbol{x})$ in Fourier space reads as follows:

$$\hat{\boldsymbol{u}}(\boldsymbol{\xi}) = \frac{1}{\Omega} \int_{\Omega} \boldsymbol{u}(\boldsymbol{x}) \exp(-i\boldsymbol{\xi} \cdot \boldsymbol{x}) \, d\boldsymbol{x} \tag{2.19}$$

where the complex number is $i = \sqrt{-1}$. The wave vector is denoted as $\boldsymbol{\xi}$. On the other hand, the inverse Fourier transform of $\hat{\boldsymbol{u}}(\boldsymbol{\xi})$ yields $\boldsymbol{u}(\boldsymbol{x})$ back

$$\boldsymbol{u}(\boldsymbol{x}) = \int_{\Omega} \hat{\boldsymbol{u}}(\boldsymbol{\xi}) \exp(i\boldsymbol{\xi} \cdot \boldsymbol{x}) \, d\boldsymbol{\xi} \tag{2.20}$$

One important feature of an expression in Fourier space is that a function with zero wave vector in Fourier space represents the average of that function in real space. In the case of the fields of displacement and the deformation gradient, that feature is given by the following

definitions:

$$\begin{aligned}\hat{\boldsymbol{u}}(\boldsymbol{\xi}=\mathbf{0}) &= \frac{1}{\Omega}\int_{\Omega}\boldsymbol{u}(\boldsymbol{x})\,d\boldsymbol{x}\\ \hat{\mathbf{F}}(\boldsymbol{\xi}=\mathbf{0}) &= \frac{1}{\Omega}\int_{\Omega}\mathbf{F}(\boldsymbol{x})\,d\boldsymbol{x}\end{aligned} \tag{2.21}$$

The gradient of the displacement field in real space $\nabla_0\boldsymbol{u}(\boldsymbol{x})$ can be simply expressed in Fourier space

$$\hat{F}_{mn}(\boldsymbol{\xi}) = i\hat{u}_m(\boldsymbol{\xi})\xi_n \tag{2.22}$$

The construction of the FFT-based scheme starts from the Fourier transform of the stress field (2.12)

$$\begin{aligned}\hat{P}_{kl}(\boldsymbol{\xi}) &= \mathbb{C}^0_{klmn} : \hat{F}_{mn}(\boldsymbol{\xi}) + \hat{\tau}_{kl}(\boldsymbol{\xi})\\ &\Longleftrightarrow i\mathbb{C}^0_{klmn}\hat{u}_m\xi_n + \hat{\tau}_{kl}\end{aligned} \tag{2.23}$$

The Fourier transform of the divergence free condition of equation (2.11) reads as follows:

$$i\hat{P}_{kl}\xi_l = \mathbf{0} \tag{2.24}$$

Equation (2.23) can be augmented into equation (2.24) to yield the following form:

$$i\hat{\tau}_{kl}\xi_l = (\hat{G}^0)^{-1}_{km}\hat{u}_m \tag{2.25}$$

where $(\hat{G}^0)^{-1}_{km} = \mathbb{C}^0_{klmn}\xi_l\xi_n$ is the inverse of the acoustic tensor. Consequently, $\hat{\boldsymbol{u}}$ can be expressed as follows:

$$\hat{u}_m = i\hat{G}^0_{mk}\hat{\tau}_{kl}\xi_l \tag{2.26}$$

The expression of the displacement field in Fourier space is used to derive the expression of the deformation gradient field in Fourier space. As a result, equations (2.22) and (2.26) are combined to express the deformation gradient field in Fourier space as follows:

$$\begin{aligned}\hat{F}_{kl} = \hat{u}_k(\boldsymbol{\xi})\xi_l &= -\hat{G}^0_{km}\hat{\tau}_{mn}\xi_n\xi_l\\ &\Leftrightarrow -\hat{\mathbb{\Gamma}}^0_{klmn}\hat{\tau}_{mn}\\ \hat{\mathbb{\Gamma}}^0_{klmn} &= \hat{G}^0_{km}\xi_l\xi_n\end{aligned} \tag{2.27}$$

where $\hat{\mathbb{\Gamma}}^0$ is the Green's operator.

2.4.2 The Reference Material for a Large Deformation Problem

According to the M. Kabel's paper, [3], a reference material should be chosen to satisfy the following coercivity condition:

$$\mathbf{F}(\boldsymbol{x}) : \mathbb{C}^0 : \mathbf{F}(\boldsymbol{x}) \geq \mathbf{F}(\boldsymbol{x}) : \mathbf{F}(\boldsymbol{x}) \quad \forall \boldsymbol{x}\,\mathrm{in}\,\Omega \tag{2.28}$$

The coercivity condition is necessary to set the norm of an error to be bounded in the case of a large deformation problem. In this context, a symmetrized linear isotropic material cannot be a reference material. The reason is that a linearly elastic $\mathbb{C}^0$ satisfying minor symmetries violates the coercivity condition (2.28). Instead, M. Kabel chose an isotropic reference material $\mathbf{C}^0_{kLmN} = \Lambda_0 \delta_{kL}\delta_{mN} + 2\mu_0 \delta_{km}\delta_{LN}$, which is a fourth-order tensor, to calculate the stress in a reference material and derive the Green's operator

$$(\hat{G}^0)^{-1}_{km} = \mathbb{C}^0_{klmn}\xi_l\xi_n \tag{2.29}$$

From the definition of the inverse of the acoustic tensor (2.29), the explicit form of acoustic tensor can be derived as follows:

$$(\hat{G}^0)^{-1}_{km} = \Lambda_0 \delta_{kL}\delta_{mN}\xi_L\xi_N + 2\mu_0 \delta_{km}\delta_{LN}\xi_L\xi_N \tag{2.30}$$

$$\hat{\mathbf{G}}^0(\boldsymbol{\xi}) = \frac{(\Lambda_0 + 2\mu_0)|\boldsymbol{\xi}|^2\mathbf{I} - \Lambda_0 \boldsymbol{\xi}\otimes\boldsymbol{\xi}}{2\mu_0(\Lambda_0 + 2\mu_0)|\boldsymbol{\xi}|^4} \tag{2.31}$$

By combining the definition of the Green's operator $\hat{\mathbb{\Gamma}}^0$ (2.27) and the explicit form of the acoustic tensor (2.31), the explicit form of the Green's operator can be derived

$$\hat{\mathbb{\Gamma}}^0_{kLmN}(\xi) = \frac{\delta_{km}\xi_L\xi_N}{2\mu_0|\boldsymbol{\xi}|^2} - \frac{\Lambda_0}{2\mu_0(\Lambda_0 + 2\mu_0)}\frac{\xi_k\xi_L\xi_m\xi_N}{|\boldsymbol{\xi}|^4} \tag{2.32}$$

2.4.3 The Fast Fourier Transform and Discretization of RVE

A 3D image is a group of pixels arranged in a 3D grid and each pixel will have its own color. Analogously, it is possible to imagine that an RVE is a 3D image made of a 3D grid. A color in each pixel of a 3D image is analogous to a material phase at each grid point in an RVE. Therefore, an RVE can be interpreted as a 3D grid having an individual material phase at each point. On top of that, each grid point will contain information of own field variables, such as stress, strain, and state variables of inelasticity. Those state variables are determined by a material constitutive law at each grid point.

The beauty of this approach is that data from digital image processes can be directly utilized, e.g. computer tomography (CT), for defining a distribution of material phases in an RVE. It is advantageous compared to the conventional finite element technology since there is zero effort for mesh generation, and saving a stiffness matrix.

The grid of an RVE has N_x points in x-coordinate, N_y points in y-coordinate, and N_z points in z-coordinate. In total, the grid has $N_x \times N_y \times N_z$ points. The index, the grid size, and the position of each grid point are summarized as follows:

	x-coordinate	y-coordinate	z-coordinate
Number of grid points	N_x	N_y	N_z
Length of RVE	L_x	L_y	L_z
Index	$i = 0, \cdots, N_x - 1$	$j = 0, \cdots, N_y - 1$	$k = 0, \cdots, N_z - 1$
Grid size	$dx = \frac{L_x}{N_x}$	$dy = \frac{L_y}{N_y}$	$dz = \frac{L_z}{N_z}$
Position of grid point	$i \cdot dx$	$j \cdot dy$	$k \cdot dz$

TABLE 2.1: RVE's properties as 3D grid.

The FFT can be used to express the displacement field in Fourier space, [10]. One of the most popular libraries for the FFT is "Fastest Fourier Transform in the West" (FFTW). By using the definitions of parameters in Table 2.1, the wave vector and the position vector at each grid point can be constructed when there is a grid point, P_{ijk}, having indexes i, j, and k in x, y, and z coordinates, it will have the wave vector $\boldsymbol{\xi}_{ijk}$ and the position vector $\boldsymbol{x}_{ijk}$. The definition of these vectors read as follows:

$$\begin{aligned} \boldsymbol{\xi}_{ijk} = [\xi_i, \xi_j, \xi_k] = 2\pi\hat{i}[\frac{i}{L_x}, \frac{j}{L_y}, \frac{k}{L_z}] \\ \boldsymbol{x}_{ijk} = [i \cdot dx, j \cdot dy, k \cdot dz] \end{aligned} \tag{2.33}$$

In FFTW, the forward Fourier transform of field quantity X_{ijk} at P_{ijk} is defined as follows:

$$Y_{ijk} = \sum_{a=0}^{N_x-1} \sum_{b=0}^{N_y-1} \sum_{c=0}^{N_z-1} X_{abc} \exp(-\hat{i}\boldsymbol{\xi}_{ijk} \cdot \boldsymbol{x}_{abc}) \tag{2.34}$$

The inverse Fourier transform of Y_{ijk} reads as follows:

$$Z_{ijk} = \sum_{a=0}^{N_x-1} \sum_{b=0}^{N_y-1} \sum_{c=0}^{N_z-1} Y_{abc} \exp(\hat{i}\boldsymbol{\xi}_{abc} \cdot \boldsymbol{x}_{ijk}) \tag{2.35}$$

In comparison to equation (2.20), the output Y_{ijk} in equation (2.34) is not normalized with respect to the total number of grid points, $N_x \times N_y \times N_z$. It can be deduced that when FFTW is used, an output will be factored by $N_x \times N_y \times N_z$ after a field variable is once forward Fourier transformed and backward Fourier transformed. Thus, at every grid point the following relation holds:

$$Z_{ijk} = (N_x \times N_y \times N_z) X_{ijk} \tag{2.36}$$

It makes a different interpretation of a field quantity with zero wave vector in Fourier space. According to equation (2.21), the function of a field variable with zero wave vector in Fourier space corresponds to the mean value of that function in real space. On the other hand, according to equation (2.33) and (2.34), that function with zero wave vector in Fourier space

is equal to a summation of that function in real space. This feature should be taken into account when the FFT-based scheme is implemented using FFTW.

2.5 The Algorithm of the FFT-based Scheme for Inelastic Behaviors

A material may have nonlinear constituents or inelastic behavior described in terms of stress, strain, and a rate of both of them. The algorithm of the FFT-based scheme for an inelastic material's behavior was introduced by H. Moulinec and P. Suquet, [1]. They suggested the algorithm for the FFT-based scheme with nonlinear constituents and successfully implemented the J_2-flow theory of elastic-plastic behavior. They calculated the fields of stress and plastic strain after the elastic strain field is updated. In the case of elastic-damage behavior, instead of plastic strain, damage and damage hardening variables are updated. The algorithm of the FFT-based scheme in the case of general inelasticities follows:

Algorithm 1 The Algorithm for a Large Deformation with Inelastic Constitutive Laws

1: **procedure** THE FFT-BASED SCHEME
2: **Initialization:** $\mathbf{F}^0(\boldsymbol{x}) = \mathbf{F}_0 \quad \forall \boldsymbol{x} \in \Omega$
3: Calculate $\mathbf{P}^0(\mathbf{F}(\boldsymbol{x}))$ using a constitutive law $\quad \forall \boldsymbol{x} \in \Omega$
4: **Iterate i+1** $\mathbf{F}^i$ and $\mathbf{P}^i$ known at every $\boldsymbol{x}_d$
5: (a) $\hat{\mathbf{P}}^i = \mathrm{FFT}(\mathbf{P}^i)$
6: (b) $\hat{\boldsymbol{\tau}}^i = \mathbb{C}^0 : (\mathbf{F}^i) - (\mathbf{P}^i)$
7: (c) $\hat{\mathbf{F}}^{i+1}(\boldsymbol{\xi}) = -\hat{\mathbb{\Gamma}}^0(\boldsymbol{\xi}) : \hat{\boldsymbol{\tau}}^i(\boldsymbol{\xi}) \quad \forall \boldsymbol{\xi} \neq \mathbf{0}, \quad \hat{\mathbf{F}}^{i+1}(\mathbf{0}) = \mathbf{F}_0$
8: (d) $\mathbf{F}^{i+1}(\boldsymbol{x}_d) = \mathrm{FFT}^{-1}(\hat{\mathbf{F}}^{i+1}(\boldsymbol{\xi})) \quad \forall \boldsymbol{x} \in \Omega$
9: (e) Calculate $\mathbf{P}^{i+1}(\mathbf{F}(\boldsymbol{x}))$ using a constitutive law $\quad \forall \boldsymbol{x} \in \Omega$
10: (f) Check the convergence criterion $\mathrm{Div}(\mathbf{P}^{i+1}(\boldsymbol{x})) = \mathbf{0} \quad \forall \boldsymbol{x} \in \Omega$

For the convergence criterion in step (e), H. Moulinec and P. Suquet proposed to calculate the convergence criterion for a small deformation problem in Fourier space

$$\mathrm{error} = \frac{\Sigma||\hat{\boldsymbol{\sigma}}(\boldsymbol{\xi})\boldsymbol{\xi}||}{N_x N_y N_z ||\hat{\boldsymbol{\sigma}}(\mathbf{0})||} \tag{2.37}$$

where $\boldsymbol{\sigma}$ stands for the Cauchy stress. On the other hand, M. Kabel proposed to evaluate convergence of the L^2-norm of the deformation gradient field in order to reduce memory occupations and computations. The convergence criterion expressed in terms of the deformation gradient reads as follows:

$$\mathrm{error} = \frac{\Sigma||\mathbf{F}^{i+1} - \mathbf{F}^i||}{N_x N_y N_z ||\mathbf{F}_0||} \tag{2.38}$$

2.6 The Defects of the Conventional FFT-based Scheme and Remedy

When it comes to using the FFT-based scheme, heterogeneity of local properties (such as effective stiffness) can lead to discontinuities in field quantities. When it comes to an elastic-damage material's simulation, an increase in the field of damage variable may deteriorate the discontinuity of field variables, such as stress and displacement. When there is an interface between elastic and elastic-damage materials in an RVE, only elastic-damage materials will be damaged and its effective stiffness will decrease further. Evolution of damage variables increases the gap between stiffness of elastic and that of elastic-damage materials. The sharp interface between material phases causes the ringing artifacts and the Gibbs effects because of the non-uniform convergence of Fourier coefficients at the points of loss of differentiability, A. Vidyasagar et al. [11]. This problem can cause differential operators, such as divergence and gradient, to be inaccurate in Fourier space. W. H. Müller introduced a numerical technique to remedy the ringing artifacts by using a modified discrete Fourier transform, [12]. The idea is to enforce the derivative in a domain to be bounded. This idea can be realized by approximating the differential operator by a finite-difference scheme. A. Vidyasagar et al. employed this idea to solve an electromechanical problem of bulk polycrystalline ferroelectric ceramics, [11]. Also, A. Vidyasagar et al. described the modified wave vector by approximating the differential operator using the central-difference scheme in their paper, [11]. According to reference [11], for a 3D problem, a wave vector at a grid point will have three components in spatial coordinates as follows:

$$\boldsymbol{\xi}_{ijk} = [\xi_i, \xi_j, \xi_k] = [\frac{\sin(2\pi/N_x\hat{i})}{dx}, \frac{\sin(2\pi/N_y\hat{j})}{dy}, \frac{\sin(2\pi/N_z\hat{k})}{dz}] \tag{2.39}$$

A. Vidyasagar et al. tested their new wave vector to calculate the derivative of a double step function. They proved that calculating spectral derivative using the new wave vector showed less oscillation compared to the result of the conventional spectral derivative. Therefore, the modified wave vector (2.39) is incorporated in this article.

Chapter 3

Damage Mechanics

3.1 Local Continuum Damage Model

In this section, the local continuum damage model will be described. The notion 'local' means that the thermodynamic state at a material point is totally determined by local quantities at that point, e.g., stress, strain, and internal variables. To begin with, the thermodynamics framework and the definition of the damage variable will be introduced. Next, the Clausius-Duhem inequality is investigated, which every model should satisfy. After that, the isotropic damage model will be formulated in the thermodynamics framework. In order to solve the damage evolution, a return-mapping algorithm will be introduced to calculate the damage variable update in an iterative manner. Finally, the micromorphic approach is used to formulate a gradient-extended damage model.

3.1.1 Thermodynamics Framework for Isotropic Damage Model

Continuum damage theories are usually based on irreversible thermodynamics and the internal state variable theory. One introduces the Helmholtz free energy potential and uses the Clausius-Duhem inequality to express the second law of thermodynamics. Since the second law of thermodynamics is a universal principle, the free energy should change while satisfying the Clausius-Duhem inequality. For an isotropic damage model, a scalar damage variable is sufficient for modeling. On the other hand, tensor valued damage variables (second or fourth-order) are necessary for expressing anisotropic damage processes [13].
In the present study, the Helmholtz free energy Ψ is chosen to be of Neo-Hookean type as

follows:

$$\Psi(\mathbf{C}, D, \xi_d) = f(D)[\frac{\mu}{2}\{\mathrm{tr}\mathbf{C} - 3 - \ln(\det\mathbf{C})\} + \frac{\Lambda}{4}\{\det\mathbf{C} - 1 - \ln(\det\mathbf{C})\}] + r\{\xi_d + \frac{\exp(-s\xi_d) - 1}{s}\} \qquad (3.1)$$
$$f(D) = (1 - D)^2$$

Here, $\mathbf{C}$ is the right Cauchy-Green tensor, $D \in [0, 1)$ is the damage variable, and ξ_d is the damage-hardening variable. The Lamé constants are μ and Λ. Damage material parameters are r and s. The function $f(D)$ expresses the influence of damage on the free energy. When a material is undamaged, $f(D)$ is one. For a fully damaged material with $D = 1$, $f(D)$ becomes zero. The Clausius-Duhem inequality is given by

$$-\dot{\Psi} + \mathbf{S} : \dot{\mathbf{E}} \geq 0 \qquad (3.2)$$

where $\mathbf{S}$ is the second Piola-Kirchhoff stress and $\mathbf{E}$ is the Green-Lagrange strain tensor. The Helmholtz free energy formula (3.1) can be plugged into the Clausius-Duhem inequality (3.2) which leads to

$$-\big(\frac{\partial\Psi}{\partial\mathbf{C}} : \dot{\mathbf{C}} + \frac{\partial\Psi}{\partial D}\dot{D} + \frac{\partial\Psi}{\partial\xi_d}\dot{\xi}_d\big) + \mathbf{S} : \dot{\mathbf{E}} \geq 0 \qquad (3.3)$$

Considering $\dot{\mathbf{E}} = \frac{1}{2}\dot{\mathbf{C}}$, inequality (3.3) can be further simplified as

$$\big(\mathbf{S} - 2\frac{\partial\Psi}{\partial\mathbf{C}}\big) : \frac{1}{2}\dot{\mathbf{C}} - \frac{\partial\Psi}{\partial D}\dot{D} - \frac{\partial\Psi}{\partial\xi_d}\dot{\xi}_d \geq 0 \qquad (3.4)$$

Since (3.4) has to be valid for arbitrary thermodynamic processes, one obtains

$$\mathbf{S} = 2\frac{\partial\Psi}{\partial\mathbf{C}} = f(D)\{\mu(\mathbf{I} - \mathbf{C}^{-1}) + \frac{\Lambda}{2}(\det\mathbf{C} - 1)\mathbf{C}^{-1}\} \qquad (3.5)$$

which is the stress-strain relationship. The remaining dissipation inequality reads

$$Y\dot{D} - q_d\dot{\xi}_d \geq 0 \qquad (3.6)$$

where

$$Y := -\frac{\partial\Psi}{\partial D} = -f'(D)[\frac{\mu}{2}\{\mathrm{tr}\mathbf{C} - 3 - \ln(\det\mathbf{C})\} + \frac{\Lambda}{4}\{\det\mathbf{C} - 1 - \ln(\det\mathbf{C})\}] \qquad (3.7)$$

$$q_d := \frac{\partial\Psi}{\partial\xi_d} = r\{1 - \exp(-s\xi_d)\} \qquad (3.8)$$

are the thermodynamic conjugate forces to damage and damage hardening, respectively.

3.1.2 Damage Loading Condition

A damage criterion is formulated with the following functional form:

$$\phi_d = Y - (Y_0 + q_d) \leq 0 \tag{3.9}$$

ϕ_d is also called "damage loading function". Y_0 is the initial damage threshold. At the point where an increase of Y leads to the case where the damage loading function becomes zero, damage loading occurs and the damage variable and damage hardening variable should be updated. The evolution of the damage and damage hardening variables is defined by the damage evolution equations

$$\begin{aligned} \dot{D} &= \dot{\lambda}\frac{\partial \phi_d}{\partial Y} = \dot{\lambda} \\ \dot{\xi_d} &= -\dot{\lambda}\frac{\partial \phi_d}{\partial q_d} = \dot{\lambda} \end{aligned} \tag{3.10}$$

where $\dot{\lambda} \geq 0$ is the damage multiplier. The damage loading/unloading conditions are given by the Karush–Kuhn–Tucker (KKT) conditions

$$\dot{\lambda} \geq 0, \quad \phi_d \leq 0, \quad \dot{\lambda}\phi_d = 0 \tag{3.11}$$

Conditions (3.11) are standard for problems involving constraints. The conditions (3.11) imply that when the damage loading function ϕ_d is negative, $\dot{\lambda}$ has to be zero to fulfill $\dot{\lambda}\phi_d = 0$. Then, the damage and damage hardening variables remain constant according to the damage evolution equations (3.10). On the other hand, if damage loading occurs so that $\dot{\lambda}$ is positive, ϕ_d should be zero to fulfill $\dot{\lambda}\phi_d = 0$ in (3.10).

3.1.3 Numerics for Damage Variable Calculation

In this section, the mathematical procedure to solve $\phi_d = 0$ is explained in the case of damage loading. In order to deal with general forms of damage models, a numerical method to solve $\phi_d = 0$ should come into play. The Newton-Raphson method is a good candidate for solving this problem since it is simple to be implemented and has quadratic convergence towards the solution. Quadratic convergence means that the error is proportional to the square of the previous error, [14].

Suppose that the simulation is at n-th loading step, and the damage and damage hardening variables are sought for the $(n+1)$-th loading step. By multiplying the simulation time step Δt on equations (3.10), the formulation of the damage and damage hardening variables at

the $(n+1)$-th loading step can be derived i.e.,

$$\begin{aligned} D^{n+1} &= D^n + \Delta\lambda \\ \xi_d^{n+1} &= \xi_d^n + \Delta\lambda \end{aligned} \tag{3.12}$$

where an increment of the damage multiplier is denoted as $\Delta\lambda = \dot{\lambda}\Delta t$. The Newton-Raphson method is utilized to estimate the damage and damage hardening variables increment $\Delta\lambda$ in an iterative manner. It starts with an initial guess for $\Delta\lambda$ which is zero. An overview of the Newton-Raphson iteration to estimate $\Delta\lambda$ looks as follows:

Algorithm 2 Algorithm for damage and damage hardening variables

1: **procedure** NEWTON-RAPHSON METHOD
2: **Initialization:** $\Delta\lambda = 0$.
3: $\Delta(\Delta\lambda)_0 = 0$.
4: **Iterate i+1** Seek increment of $\Delta\lambda$ and update D and ξ_d.
5: (a) Update $\Delta\lambda_{i+1} = \Delta\lambda_i + \Delta(\Delta\lambda)_i$.
6: (b) Update D and ξ_d. $D_{i+1} = D^n + \Delta\lambda_{i+1}$, $\xi_{d,i+1} = \xi_d^n + \Delta\lambda_{i+1}$.
7: (c) Calculate residual $\phi_{d,i+1}$.
8: **if** $||\phi_{d,i+1}|| < tolerance$ **then return** D and ξ_d.
9: **else**
10: (d) Calculate $K_{loc} = \frac{\partial\phi_{d,i+1}}{\partial\Delta\lambda} = \frac{\partial Y_{i+1}}{\partial D}\frac{\partial D}{\partial\Delta\lambda} - \frac{\partial q_{d,i+1}}{\partial\xi_d}\frac{\partial\xi_d}{\partial\Delta\lambda}$.
11: (e) Calculate $\Delta(\Delta\lambda)_{i+1} = -\frac{\phi_{d,i+1}}{K_{loc}}$.
12: (f) $i = i+$ and repeat the algorithm from step (a).

This is the so-called return-mapping algorithm which is widely used in computational mechanics.

3.1.4 Validation of the Implementation of the Local Damage Model

Once the algorithm (2) to solve the damage evolution has been implemented, it should be validated whether the implementation yields a correct solution. The problem of the elastic-damage material's damage evolution is defined in terms of the damage loading function (3.9), the evolution laws (3.10) and the KKT conditions (3.11). To make the validation simple, a virtual experiment of uniaxial stretch is performed. The deformation gradient during the uniaxial stretch reads as follows:

$$\mathbf{F} = \begin{pmatrix} l_i & 0 & 0 \\ 0 & \sqrt{l_i} & 0 \\ 0 & 0 & \sqrt{l_i} \end{pmatrix} \quad l_i \in [1, l_f] \tag{3.13}$$

where l_i is the stretch in x-direction at i-th loading step, and l_f is the stretch at the final step. l_i is monotonously increasing from 1 to its final value l_f. $l_i = 1$ means that the body is in an undeformed state. l_f should be chosen large enough in order to observe elastic-damage behavior.

To begin with, the equation (3.9) is solved using MATLAB's built-in nonlinear equation solver. At each loading step, the right Cauchy-Green tensor and its invariants, $\mathrm{tr}(\mathbf{C})$ and $\det(\mathbf{C})$, are calculated. Then the thermodynamic conjugate forces Y and q_d are calculated, (3.7) and (3.8). The damage loading function is calculated and solved for a new value of the damage multiplier when its norm exceeds a prescribed tolerance. Otherwise, the damage multiplier and damage variable remain unchanged. On the other side, the return-mapping algorithm (2) is implemented into the algorithm of the FFT-based scheme (1). For a homogeneous RVE, the deformation gradient at each grid point will be the same as the prescribed macroscopic deformation gradient F_0 in equation (2.7) because there will be no fluctuating field arising from a heterogeneity of the microstructure. The solution obtained from algorithm (2) is compared with the solution derived using MATLAB. The material parameters used in the study are given in Table 3.1.

	Symbol	Value	Unit
Lamé's first parameter	Λ	5000	MPa
Lamé's second parameter	μ	7500	MPa
Initial damage threshold	Y_0	5	MPa
damage parameter	r	50	MPa
exponential damage parameter	s	0.5	-

TABLE 3.1: Material parameters for elastic-damage model

By assigning these parameters at each grid point, a homogeneous RVE is defined. A comparison between the results is shown in Figure 3.1:

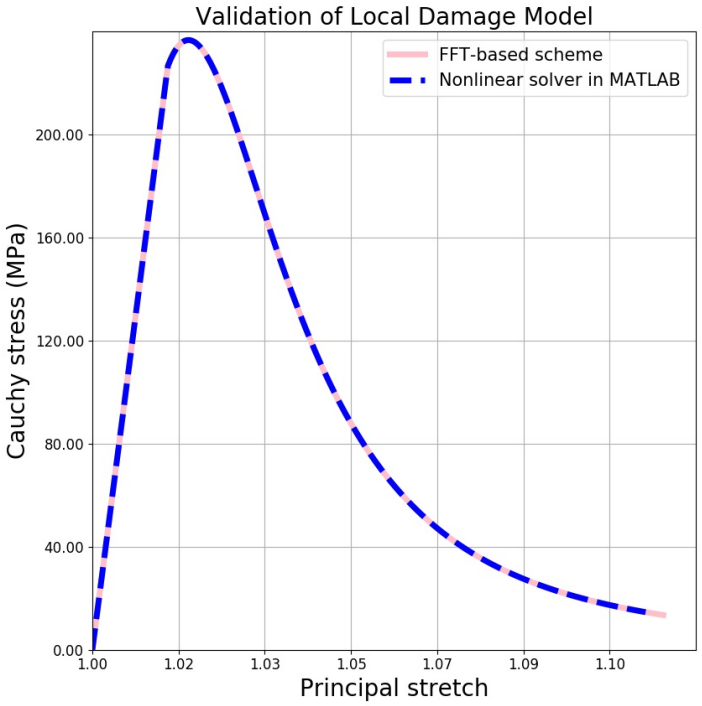

FIGURE 3.1: Comparison between the results of the nonlinear solver using MATLAB and the implementation of algorithm (2) in the FFT-based scheme.

Here, the pink line is the result of the FFT-based scheme and the blue dashed line is the result of the built-in nonlinear solver in MATLAB. As shown in Figure 3.1, those two results match exactly. This is a good indication that the elastic-damage model is implemented correctly.

3.2 Gradient-Extended Damage Model

In recent decades, the defect of local continuum damage models in describing material softening behavior has been discussed. The defect is triggered by a loss of well-posedness of the boundary-value problem beyond a certain level of accumulated damage. As a result, the ill-posedness leads to the problem that the numerical solutions do not converge to a physically reasonable solution upon h-refinement of the spatial discretization, [15–18].
Several authors suggested to discard local action based constitutive laws to fix the problem of ill-posedness. So-called nonlocal continuum damage models have been developed to yield mesh-objective solutions, [15]. Gradient-extended models are especially popular and promising since, while incorporating nonlocal interactions, they still remain local in a mathematical sense which makes their implementation easier and more efficient, [19]. In

the next section, the micromorphic approach as a systematic method to construct gradient-extended nonlocal constitutive models will be described. After a discussion of the general micromorphic approach, its application is shown for the case of a continuum damage model.

3.2.1 Micromorphic Approach

The micromorphic approach in the sense of Samuel Forest is a well-established and systematic procedure to incorporate gradient effects into already existing local material models (for details, see e.g. Forest [4]). In the case of an isotropic damage model as considered in this study, one introduces a so-called micromorphic damage variable $\bar{D}$ into the formulation which has the meaning of an additional internal degree of freedom of the material (similar, e.g., to the temperature in case of a thermomechanically coupled model). A coupling of $\bar{D}$ to the corresponding local damage variable D is then enforced by postulating a direct dependence of the free energy on the difference between the two quantities, i.e., $(D - \bar{D})$. The starting point of the micromorphic approach is usually the principle of virtual work. Assuming a geometrically nonlinear, quasi-static and purely mechanical framework, the expressions for the internal (g_{int}) and external (g_{ext}) virtual work can, for example, be formulated with respect to quantities defined in the reference configuration B_0 of the body as follows:

$$g_{int} = \int_{B_0} \mathbf{S} : \delta\mathbf{E}\, dV + \int_{B_0} (a_{0i}\delta\bar{D} + \boldsymbol{b}_{0i} \cdot \nabla_0\delta\bar{D})\, dV$$
$$g_{ext} = \int_{B_0} \boldsymbol{f}_0 \cdot \delta\boldsymbol{u}\, dV + \int_{\partial B_{0_t}} \boldsymbol{t}_0 \cdot \delta\boldsymbol{u}\, dA + \int_{B_0} (a_{0e}\delta\bar{D} + \boldsymbol{b}_{0e} \cdot \nabla_0\delta\bar{D})\, dV + \int_{\partial B_{0c}} a_{0c}\delta\bar{D}\, dA \tag{3.14}$$

Here, dV and dA stand for volume and surface integrals of the initial domain, respectively. The Green-Lagrange strain tensor is denoted as $\mathbf{E}$, $\mathbf{S}$ is the second Piola-Kirchhoff stress, $\boldsymbol{u}$ is the displacement, a_{0i} and $\boldsymbol{b}_{0i}$ are internal forces associated with $\bar{D}$. Likewise, a_{0e} and $\boldsymbol{b}_{0e}$ are generalized volume forces associated with $\bar{D}$. $\boldsymbol{f}_0$ is the mechanical body force acting in the initial configuration. Quantities $\boldsymbol{t}_0$ and a_{0c} are tractions on boundaries ∂B_{0_t} and ∂B_{0_c}. The test function $\delta\mathbf{E}$ can be represented in terms of $\mathbf{F}$ and $\delta\boldsymbol{u}$ as:

$$\delta\mathbf{E} = \frac{1}{2}\big(\mathbf{F}^T\nabla_0(\delta\boldsymbol{u}) + \nabla_0(\delta\boldsymbol{u})^T\mathbf{F}\big) \tag{3.15}$$

With the help of simple algebraic manipulations, one can then write:

$$\mathbf{S} : \delta\mathbf{E} = (\mathbf{F}\mathbf{S}) : \nabla_0\delta\boldsymbol{u} \tag{3.16}$$

Consequently, there are two test functions $\delta\boldsymbol{u}$ and $\delta\bar{D}$, and they should be zero on Dirichlet boundaries ∂B_{0_u} and $\partial B_{0_{\bar{\phi}}}$, respectively. From the principle of virtual work, i.e.,

$$g_{int} - g_{ext} = 0 \tag{3.17}$$

the strong form of the equation for the micromorphic variable $\bar{D}$ will be derived. By incorporating (3.14) and (3.16) into (3.17), it follows:

$$\begin{aligned}\int_{B_0} (\mathbf{FS}) : \nabla_0 \delta\boldsymbol{u}\, dV + \int_{B_0} [(a_{0i} - a_{0e})\delta\bar{D} + (\boldsymbol{b}_{0i} - \boldsymbol{b}_{0e}) \cdot \nabla_0 \delta\bar{D}]\, dV - \int_{B_0} \boldsymbol{f}_0 \cdot \delta\boldsymbol{u}\, dV \\ - \int_{\partial B_{0_t}} \boldsymbol{t}_0 \cdot \delta\boldsymbol{u}\, dA - \int_{\partial B_{0c}} a_{0c}\delta\bar{D}\, dA = 0\end{aligned} \tag{3.18}$$

The first term should be expanded using the following formula, [20],

$$\begin{aligned}\mathrm{Div}(\delta\boldsymbol{u}(\mathbf{FS})) &= \mathrm{Div}(\mathbf{FS}) \cdot \delta\boldsymbol{u} + (\mathbf{FS}) : \nabla_0(\delta\boldsymbol{u}) \\ \Leftrightarrow (\mathbf{FS}) : \nabla_0(\delta\boldsymbol{u}) &= \mathrm{Div}(\delta\boldsymbol{u}(\mathbf{FS})) - \delta\boldsymbol{u} \cdot \mathrm{Div}(\mathbf{FS})\end{aligned} \tag{3.19}$$

Analogously, it holds

$$(\boldsymbol{b}_{0i} - \boldsymbol{b}_{0e}) \cdot \nabla_0 \delta\bar{D} = \mathrm{Div}((\boldsymbol{b}_{0i} - \boldsymbol{b}_{0e})\delta\bar{D}) - \mathrm{Div}(\boldsymbol{b}_{0i} - \boldsymbol{b}_{0e})\delta\bar{D}. \tag{3.20}$$

Inserting (3.19) and (3.20) into (3.18) yields

$$\begin{aligned}\int_{B_0} [\mathrm{Div}(\delta\boldsymbol{u}(\mathbf{FS})) - (\mathrm{Div}(\mathbf{FS}) + \boldsymbol{f}_0) \cdot \delta\boldsymbol{u}]\, dV - \int_{\partial B_{0_t}} \boldsymbol{t}_0 \cdot \delta\boldsymbol{u}\, dA \\ + \int_{B_0} [(a_{0i} - a_{0e})\delta\bar{D} + \mathrm{Div}((\boldsymbol{b}_{0i} - \boldsymbol{b}_{0e})\delta\bar{D}) - \mathrm{Div}(\boldsymbol{b}_{0i} - \boldsymbol{b}_{0e})\delta\bar{D}]\, dV - \int_{\partial B_{0c}} a_{0c}\delta\bar{D}\, dA = 0\end{aligned} \tag{3.21}$$

The test functions $\delta\boldsymbol{u}$ and $\delta\bar{D}$ vanish on Dirichlet boundaries. Furthermore, by using the divergence theorem to convert the volume integration of divergence terms into surface integration over ∂B_{0_t} and ∂B_{0_c}, [20], one obtains:

$$\begin{aligned}\int_{B_0} \mathrm{Div}(\delta\boldsymbol{u}(\mathbf{FS}))\, dV = \int_{\partial B_{0_t}} (\delta\boldsymbol{u}(\mathbf{FS})) \cdot \boldsymbol{n}_0\, dA = \int_{\partial B_{0_t}} ((\mathbf{FS})\boldsymbol{n}_0) \cdot \delta\boldsymbol{u} dA \\ \int_{B_0} \mathrm{Div}((\boldsymbol{b}_{0i} - \boldsymbol{b}_{0e})\delta\bar{D})\, dV = \int_{\partial B_{0_c}} (\boldsymbol{b}_{0i} - \boldsymbol{b}_{0e})\delta\bar{D} \cdot \boldsymbol{n}_0\, dA = \int_{\partial B_{0_c}} (\boldsymbol{b}_{0i} - \boldsymbol{b}_{0e}) \cdot \boldsymbol{n}_0 \delta\bar{D}\, dA\end{aligned} \tag{3.22}$$

where n_0 is a normal to the boundary ∂B_0. Now, (3.21) can be expressed as

$$\begin{aligned}\int_{B_0} (-\mathrm{Div}(\mathbf{FS}) - \boldsymbol{f_0}) \cdot \delta\boldsymbol{u}\, dV + \int_{\partial B_{0_t}} ((\mathbf{FS})\boldsymbol{n}_0 - \boldsymbol{t}_0) \cdot \delta\boldsymbol{u}\, dA \\ + \int_{B_0} \{(a_{0i} - a_{0e}) - \mathrm{Div}(\boldsymbol{b}_{0i} - \boldsymbol{b}_{0e})\}\delta\bar{D}\, dV + \int_{\partial B_{0c}} \{(\boldsymbol{b}_{0i} - \boldsymbol{b}_{0e}) \cdot \boldsymbol{n}_0 - a_{0c}\}\delta\bar{D}\, dA = 0\end{aligned} \tag{3.23}$$

Because equation (3.23) should be valid for arbitrary test functions, the following equations can be derived:

$$\mathrm{Div}(\mathbf{FS}) + \boldsymbol{f}_0 = \boldsymbol{0} \quad in \quad B_0 \tag{3.24a}$$

$$(\mathbf{FS})\boldsymbol{n}_0 = \boldsymbol{t}_0 \quad on \quad \partial B_{0_t} \tag{3.24b}$$

$$\boldsymbol{u} = \boldsymbol{u}_D \quad on \quad \partial B_{0_u} \tag{3.24c}$$

$$\mathrm{Div}(\boldsymbol{b}_{0i} - \boldsymbol{b}_{0e}) = a_{0i} - a_{0e} \quad in \quad B_0 \tag{3.24d}$$

$$(\boldsymbol{b}_{0i} - \boldsymbol{b}_{0e}) \cdot \boldsymbol{n}_0 = a_{0c} \quad on \quad \partial B_{0c} \tag{3.24e}$$

$$\bar{D} = \bar{D}_D \quad on \quad \partial B_{0_{\bar{D}}} \tag{3.24f}$$

Here, $\boldsymbol{u}_D$ and $\bar{D}_D$ are prescribed values at the Dirichlet boundaries B_{0_u} and $B_{0_{\bar{D}}}$. As a result, the equations (3.24a) and (3.24d) are strong forms of (3.18). Corresponding Neumann boundary conditions are (3.24b) and (3.24e). Dirichlet boundary conditions are (3.24c) and (3.24f). Expression (3.24f) is a Dirichlet boundary condition for $\bar{D}$ (which is, however, not considered in the present work).

3.2.2 Extension of Thermodynamics Framework using Micromorphic Approach

The Helmholtz free energy (3.1) can be extended to a micromorphic damage model in the following way:

$$\begin{aligned}\Psi(\mathbf{C}, D, \xi_d, \bar{D}) = f(D)[\frac{\mu}{2}\{\mathrm{tr}\mathbf{C} - 3 - \ln(\det\mathbf{C})\} + \frac{\Lambda}{4}\{\det\mathbf{C} - 1 - \ln(\det\mathbf{C})\}] \\ + r\{\xi_d + \frac{\exp(-s\xi_d) - 1}{s}\} + \frac{1}{2}H(D - \bar{D})^2 + \frac{1}{2}A\nabla_0\bar{D} \cdot \nabla_0\bar{D} \\ f(D) = (1 - D)^2\end{aligned} \tag{3.25}$$

Here, H is a penalty term, supposed to be a large value, and A is a parameter which describes the influence of the gradient in the material. The penalty term, H, can be any value which is a large enough value such that D and $\bar{D}$ are closely related to each other, [4]. On the other hand, A can be regarded as a material parameter. In the following, generalized external forces are neglected. By plugging (3.25) into an extended form of the Clausius-Duhem inequality, one obtains:

$$\begin{aligned} -\dot{\Psi} + \mathbf{S} : \dot{\mathbf{E}} + a_{0i}\dot{\bar{D}} + \boldsymbol{b}_{0i} \cdot \nabla_0\dot{\bar{D}} \geq 0 \\ \Leftrightarrow -\big(\frac{\partial\Psi}{\partial\mathbf{C}} : \dot{\mathbf{C}} + \frac{\partial\Psi}{\partial D}\dot{D} + \frac{\partial\Psi}{\partial\xi_d}\dot{\xi}_d + \frac{\partial\Psi}{\partial\bar{D}}\dot{\bar{D}} + \frac{\partial\Psi}{\partial\nabla\bar{D}} : \nabla_0\dot{\bar{D}}\big) + \mathbf{S} : \frac{1}{2}\dot{\mathbf{C}} + a_{0i}\dot{\bar{D}} + \boldsymbol{b}_{0i} \cdot \nabla_0\dot{\bar{D}} \geq 0 \\ \Leftrightarrow \big(\mathbf{S} - 2\frac{\partial\Psi}{\partial\mathbf{C}}\big) : \frac{1}{2}\dot{\mathbf{C}} + \big(a_{0i} - \frac{\partial\Psi}{\partial\bar{D}}\big)\dot{\bar{D}} + \big(\boldsymbol{b}_{0i} - \frac{\partial\Psi}{\partial\nabla_0\bar{D}}\big) \cdot \nabla_0\dot{\bar{D}} - \frac{\partial\Psi}{\partial D}\dot{D} - \frac{\partial\Psi}{\partial\xi_d}\dot{\xi}_d \geq 0. \end{aligned} \tag{3.26}$$

The terms $\left(\mathbf{S} - 2\frac{\partial \Psi}{\partial \mathbf{C}}\right), \left(a_0 - \frac{\partial \Psi}{\partial \bar{D}}\right)$, and $\left(\boldsymbol{b}_0 - \frac{\partial \Psi}{\partial \nabla_0 \bar{D}}\right)$ are assumed to vanish identically. Consequently, the following relations hold:

$$\begin{aligned} \mathbf{S} &= 2\frac{\partial \Psi}{\partial \mathbf{C}} \\ a_0 = \frac{\partial \Psi}{\partial \bar{D}} &= -H(D - \bar{D}) \\ \boldsymbol{b_0} = \frac{\partial \Psi}{\partial \nabla_0 \bar{D}} &= A \nabla_0 \bar{D} \end{aligned} \tag{3.27}$$

The thermodynamic conjugate forces of the system are,

$$\begin{aligned} Y := -\frac{\partial \Psi}{\partial D} = -f'(D)[\frac{\mu}{2}\{\mathrm{tr}\mathbf{C} - 3 - \ln(\det\mathbf{C})\} + \frac{\Lambda}{4}\{\det\mathbf{C} - 1 - \ln(\det\mathbf{C})\}] - H(D - \bar{D}) \\ q_d := \frac{\partial \Psi}{\partial \xi_d} = r\{1 - \exp(-s\xi_d)\} \end{aligned} \tag{3.28}$$

Finally, by inserting a_{0i} and $\boldsymbol{b}_{0i}$ in (3.27) into (3.24d), the micromorphic balance equation for the micromorphic damage variable is derived,

$$\begin{aligned} &\mathrm{Div}(A \nabla_0 \bar{D}) + H(D - \bar{D}) = 0 \\ \Leftrightarrow\ &A\mathrm{Div}(\nabla_0 \bar{D}) + H(D - \bar{D}) = 0 \\ \Leftrightarrow\ &A \nabla_0^2 \bar{D} + H(D - \bar{D}) = 0 \\ \Leftrightarrow\ &\bar{D} - \frac{A}{H}\nabla_0^2 \bar{D} = D \\ \Leftrightarrow\ &\bar{D} - \alpha \nabla_0^2 \bar{D} = D, \quad \alpha = \frac{A}{H} \end{aligned} \tag{3.29}$$

Chapter 4

Coupling Schemes

In this chapter, the concepts of coupling strategies are introduced to calculate the fields of the local and the nonlocal damage variables. In the thermodynamics framework based on the micromorphic approach, two governing laws to be fulfilled. One is given by the Karush–Kuhn–Tucker (KKT) conditions (3.11), and the other one is by the micromorphic balance equation (3.29). In general, a coupling scheme is necessary to find a solution satisfying multiple numerical models. To be more specific, in this case, a coupling scheme is necessary to find the solution of the local and nonlocal damage fields, which satisfies both the KKT conditions and the micromorphic balance equation. In this context, the partitioned approaches and simultaneous approach (scheme) are presented. The staggered scheme and iteratively staggered scheme belong to the class of partitioned approaches. The staggered scheme can be unstable in a certain case where multiple numerical models in a system cannot be treated individually. On the contrary, the iteratively staggered scheme yields a stable solution for a coupled problem, but it can be too much time-consuming. The simultaneous scheme can be an alternative method to remedy defects of those two partitioned approaches. These three coupling schemes are described and implemented to calculate the local and nonlocal damage variables which satisfy both the KKT conditions and the micromorphic balance equation. Finally, after the implementations of the coupling schemes are tested using a homogeneous problem, it is concluded that the simultaneous scheme is not only stable but also runs faster than the others do. In conclusion, the simultaneous scheme is employed for the current research.

4.1 Introduction of Coupling Schemes

4.1.1 Partitioned Approach

The partitioned approach is the numerical method to split a group of numerical models of field quantities into isolated ones. The interactions between numerical models of field quantities are regarded as forcing effects that are communicated between the individual components [21]. In the category of partitioned approaches, the staggered and the iteratively staggered schemes are widely known and used.

4.1.1.1 Pros and Cons of the Partitioned Approach

The key favors of the partitioned approach are an independent modeling and modularity, [21].

Independent Modeling. The partitioned approach facilitates the use of different numerical models. For instance, when it comes to a fluid-structure interaction problem, the meshes of structure and fluid do not necessarily coincide at their interface. This inconsistency lying on that interface gives rise to difficulties in the analysis of complex systems such as aircraft or submarine. Individual model can be devised by individual design team to get rid of the difficulties arising from the non-matching interfaces.

Modularity. New models can be incorporated in a modular platform depending on project needs. For example, a new local nonlinear effect can be included while keeping the rest the same. Implementation, testing, validation, and analysis of individual changes can be carried out.

Nevertheless, these benefits do not come for free. The partitioned approach necessitates delicate formulation and implementation to prevent degradation in stability and accuracy. Parallelization of code should be carefully implemented. Gains of computational efficiency with respect to a simultaneous approach are not always granted. If an interaction between multiple fields occurs through a volume, such as thermal and electromagnetic fields, efficiency in parallelization can be lost.

4.1.1.2 Staggered Scheme

The staggered scheme is one of the most favored partitioned approaches. When there are multiple numerical models involved in a system, a staggered scheme is used to split and solve them one by one. At the beginning, an initial guess of the solution of field quantities is estimated. Next, one numerical model is solved for one corresponding field quantity while

the other field quantities are kept constant. That field quantity is updated and the same solution procedure is applied for the other numerical models. After every numerical model is solved, the staggered scheme terminates.

In order to have a clear idea of staggered schemes, an example of a two-field coupled problem is given:

$$\begin{aligned} f_1(u,\phi) &= 0 \quad \text{in}\,\Omega \\ f_2(u,\phi) &= 0 \quad \text{in}\,\Omega \end{aligned} \tag{4.1}$$

where u and ϕ are scalar field quantities in domain Ω. $f_1(u,\phi)$ and $f_2(u,\phi)$ are scalar quantities as well. However, u, ϕ, $f_1(u,\phi)$, and $f_2(u,\phi)$ could be vectors in more general cases, and the following coupling schemes would still be valid. In order to solve problem (4.1), the Newton-Raphson method can be used to solve $f_1(u,\phi) = 0$ and $f_2(u,\phi) = 0$ individually. The Newton-Raphson method is implemented based on a staggered scheme to solve problem (4.1) as described in algorithm 3. In algorithm 3, the increment of u is calculated firstly. Then, u is updated with u^{n+1} and used to solve the second numerical model $f_2(u^{n+1},\phi^n) = 0$. Finally, the second model is solved, and ϕ is updated with ϕ^{n+1}. Algorithm 3 summarizes the process of the staggered scheme.

Algorithm 3 The algorithm of Staggered Scheme

1: **procedure** STAGGERED SCHEME USING THE NEWTON-RAPHSON METHOD
2: **Initialization:** Load previous values ϕ^n and u^n.
3: (a) Solve $\frac{\partial f_1(u^n,\phi^n)}{\partial u}\Delta u = -f_1(u^n,\phi^n)$ for Δu.
4: (b) Update $u^{n+1} = u^n + \Delta u$.
5: (c) Solve $\frac{\partial f_2(u^{n+1},\phi^n)}{\partial \phi}\Delta \phi = -f_2(u^{n+1},\phi^n)$ for $\Delta \phi$.
6: (d) Update $\phi^{n+1} = \phi^n + \Delta \phi$.
7: **Return**

4.1.1.3 Instability of the Staggered Scheme

Instabilities can arise in staggered schemes when interactions between numerical models are highly nonlinear. In the literature [21], it is described that, in the case of more general problems, particularly those modeled by oscillatory second order ordinary-differential equations, the stability can heavily be spoiled. A staggered scheme is highly effective for first-order parabolic systems, but the stability and the accuracy of a scheme is not guaranteed for general problems.

A general description of the cause of instability in a staggered scheme can be explained by using the aforementioned two-field coupled problem (4.1). In order to visualize changes in the field quantities, the sets of field quantities at each step in algorithm 3 are summarized as follows:

Step	The set of field quantities	Valid equation
Initialization	(u^n, ϕ^n)	-
(a)	(u^n, ϕ^n)	-
(b)	(u^{n+1}, ϕ^n)	$f_1(u^{n+1}, \phi^n) = 0$
(c)	(u^{n+1}, ϕ^n)	-
(d)	(u^{n+1}, ϕ^{n+1})	$f_2(u^{n+1}, \phi^{n+1}) = 0$

TABLE 4.1: Field quantities and equations at each step in algorithm 3

At step (d) in Table 4.1, the set of field quantities (u^{n+1}, ϕ^{n+1}) is calculated and satisfies the second equation $f_2(u^{n+1}, \phi^{n+1}) = 0$. On the other hand, it is not clear whether the set (u^{n+1}, ϕ^{n+1}) satisfies $f_1(u^{n+1}, \phi^{n+1}) = 0$. At step (b), only the set (u^{n+1}, ϕ^n) is valid for the first equation since it is calculated by solving the equation $f_1(u, \phi) = 0$ for u^{n+1}. Therefore, the set of field quantities (u^{n+1}, ϕ^{n+1}) does not necessarily satisfy $f_1(u^{n+1}, \phi^{n+1})$ and $f_2(u^{n+1}, \phi^{n+1})$ at the same time. Thus, running only one iteration of algorithm 3 fulfills one numerical model, but the other one may not be satisfied.
At the same time, an investigation of the instability of a staggered scheme can be found in a problem of fluid-structure interaction described in the literature [22]. When a staggered scheme is applied to couple fluid field and structure on a wet surface, a destabilizing effect occurs, which is called "artificial added mass" effect. It is observed that the stability of the numerical scheme depends on the combination of temporal discretization and parameters of structure and fluid, such as density and stiffness. Even though decreasing the size of a time step usually leads to an enhanced accuracy of a numerical scheme, decreasing the size of a time step here rather causes the instability to occur earlier. The instability cannot be healed by increasing the accuracy in temporal discretization since the instability arises from an inherent instability of the staggered scheme. This drawback of staggered schemes motivates to use iteratively staggered schemes which avoid instability while keeping the advantages of partitioned approaches.

4.1.1.4 Iteratively Staggered Scheme

While each numerical model is solved only once during a time step in a staggered scheme, a staggered scheme is repetitively executed until a convergence criterion is satisfied in an iteratively staggered scheme. In problem (4.1), by iterating algorithm 3 until the set of field quantities fulfills every numerical model, the instability of the staggered scheme is removed. The convergence criterion for an iteratively staggered scheme is called "coupling condition". A coupling condition should be defined to ensure that a set of field quantities satisfies every

numerical model. The algorithm of the iteratively staggered scheme for problem (4.1) is given as follows:

Algorithm 4 The algorithm of Iteratively Staggered Scheme

1: **procedure** ITERATIVELY STAGGERED SCHEME
2: **Initialization:** Load previous values for initial guesses, $\phi_0^{n+1} = \phi^n$ and $u_0^{n+1} = u^n$.
3: **Repeat:**
4: (a) Solve $\frac{\partial f_1(u_i^{n+1}, \phi_i^{n+1})}{\partial u} \Delta u = -f_1(u_i^{n+1}, \phi_i^{n+1})$.
5: (b) Update $u_{i+1}^{n+1} = u_i^{n+1} + \Delta u$.
6: (c) Solve $\frac{\partial f_2(u_{i+1}^{n+1}, \phi_i^{n+1})}{\partial \phi} \Delta \phi = -f_2(u_{i+1}^{n+1}, \phi_i^{n+1})$.
7: (d) Update $\phi_{i+1}^{n+1} = \phi_i^{n+1} + \Delta \phi$.
8: **if** Coupling condition ($||f_1(u_{i+1}^{n+1}, \phi_{i+1}^{n+1})|| <= \text{tol}$ && $||f_2(u_{i+1}^{n+1}, \phi_{i+1}^{n+1})|| <= \text{tol}$) is fulfilled **then**
9: **return** u_{i+1}^{n+1} and ϕ_{i+1}^{n+1}.
10: **else**
11: (c) $i = i + 1$ and go to step (a).

After step (d), the convergence is validated by using the coupling condition in algorithm 4. If the coupling condition is fulfilled, the set of field quantities $(u_{i+1}^{n+1}, \phi_{i+1}^{n+1})$ is returned. Otherwise, the solution procedure restarts from step (a).

The iteratively staggered scheme is the easiest way to avoid the drawback of the staggered scheme. Furthermore, it is an efficient tool to keep advantage of modular programming. Nevertheless, depending on the problem, an iteratively staggered scheme might be too time-consuming for solving coupled problems. In order to speed up the simulation, the simultaneous scheme can be a better option.

4.1.2 Simultaneous Scheme

Instead of solving numerical models individually, the idea of solving all of the numerical models for a time increment is devised. This approach is called "simultaneous approach (scheme)" or "monolithic approach", [21]. In this article, the Newton-Raphson method is employed as a basic methodology to construct the simultaneous scheme. For nonlinear coupling problems, by applying the Newton-Raphson method for every numerical model, a Jacobian matrix can be assembled such that all of the field quantities can be solved and updated simultaneously. Since a simultaneous scheme seeks for a solution which satisfies every numerical model at the same time, it is possible to heal the instability of staggered schemes.

The example problem (4.1) can be solved using the simultaneous scheme. To begin with,

the residual of a set of simultaneous equations should be defined. In equations (4.1), $f_1(u, \phi)$ and $f_2(u, \phi)$ are calculated to define the residual vector. Next, the Jacobian matrix in algorithm 5 is constructed by differentiating the residual vector with respect to unknown variables u and ϕ. The definition of the Jacobian matrix reads as follows:

$$\begin{pmatrix} \frac{\partial f_1}{\partial u} & \frac{\partial f_1}{\partial \phi} \\ \frac{\partial f_2}{\partial u} & \frac{\partial f_2}{\partial \phi} \end{pmatrix} \tag{4.2}$$

Next, the increments of u and ϕ are calculated. Finally, the field quantities of u and ϕ, and the coupling condition is tested. This procedure of the simultaneous scheme is summarized in algorithm 5.

Algorithm 5 The algorithm of Simultaneous Scheme

1: **procedure** SIMULTANEOUS SCHEME
2: **Initialization:** Load previous values for initial guesses, $\phi_0^{n+1} = \phi^n$ and $u_0^{n+1} = u^n$.
3: **Repeat:**
4: (a) Calculate the residuals $f_1(u_i^{n+1}, \phi_i^{n+1})$ and $f_2(u_i^{n+1}, \phi_i^{n+1})$.
5: (b) Calculate the Jacobian matrix $\mathbf{J}_i = \begin{pmatrix} \frac{\partial f_1}{\partial u} & \frac{\partial f_1}{\partial \phi} \\ \frac{\partial f_2}{\partial u} & \frac{\partial f_2}{\partial \phi} \end{pmatrix} \Bigg|_i$.
6: (c) Solve $\mathbf{J}_i \begin{pmatrix} \Delta u \\ \Delta \phi \end{pmatrix} = - \begin{pmatrix} f_1(u_i^{n+1}, \phi_i^{n+1}) \\ f_2(u_i^{n+1}, \phi_i^{n+1}) \end{pmatrix}$ for $\begin{pmatrix} \Delta u \\ \Delta \phi \end{pmatrix}$.
7: (d) Update $u_{i+1}^{n+1} = u_i^{n+1} + \Delta u$ and $\phi_{i+1}^{n+1} = \phi_i^{n+1} + \Delta \phi$.
8: **if** Coupling condition ($||f_1(u_{i+1}^{n+1}, \phi_{i+1}^{n+1})|| <= \text{tol}$ && $||f_2(u_{i+1}^{n+1}, \phi_{i+1}^{n+1})|| <= \text{tol}$) is fulfilled **then**
9: **return** u_{i+1}^{n+1} and ϕ_{i+1}^{n+1}.
10: **else**
11: (c) $i = i + 1$ and go to step (a).

4.1.2.1 The Reason Why the Simultaneous Scheme Can Be Faster

An efficient implementation of a simultaneous scheme can be more efficient than that of an iteratively staggered scheme. That is because it is possible to retain the quadratic rate of convergence towards the solution using the Newton-Raphson method, [14]. This can be described by comparing the solution procedures of a simultaneous scheme and that of an iteratively staggered scheme. An iteratively staggered scheme's Jacobian matrix can be calculated in the manner which is comparable to that of a simultaneous scheme in algorithm 5. More precisely, the linear equation to calculate an increment in the Newton-Raphson

method reads as follows:

$$\begin{pmatrix} \frac{\partial f_1}{\partial u} & \frac{\partial f_1}{\partial \phi} \\ \frac{\partial f_2}{\partial u} & \frac{\partial f_2}{\partial \phi} \end{pmatrix} \begin{pmatrix} \Delta u \\ \Delta \phi \end{pmatrix} = - \begin{pmatrix} f_1(u_i^{n+1}, \phi_i^{n+1}) \\ f_2(u_i^{n+1}, \phi_i^{n+1}) \end{pmatrix} \tag{4.3}$$

In an iteratively staggered scheme, when $f_1(u, \phi)$ is solved for Δu, $\Delta \phi$ is considered as a zero value. As a consequence, $\frac{\partial f_1}{\partial \phi}$ is zero in an iteratively staggered scheme. In the same manner, $\frac{\partial f_2}{\partial u}$ is also regarded as a zero value. The modified linear equation for the iteratively staggered scheme is given by:

$$\begin{pmatrix} \frac{\partial f_1}{\partial u} & 0 \\ 0 & \frac{\partial f_2}{\partial \phi} \end{pmatrix} \begin{pmatrix} \Delta u \\ \Delta \phi \end{pmatrix} = - \begin{pmatrix} f_1(u_i^{n+1}, \phi_i^{n+1}) \\ f_2(u_{i+1}^{n+1}, \phi_i^{n+1}) \end{pmatrix} \tag{4.4}$$

In equation (4.4), the second residual $-f_2(u_{i+1}^{n+1}, \phi_i^{n+1})$ is calculated using u_{i+1}^{n+1} because the first row is solved, and the updated u is used for the second row. The comparison between equations (4.3) and (4.4) proves that the Jacobian matrix in the iteratively staggered scheme has zero values in the second diagonal, equation (4.4). The iteratively staggered scheme discussed in this article can be understood as the Gauss-Seidel-like method, Kay Hameyer [23]. At the same time, an iteratively staggered scheme can be formulated in the Jacobi-like manner, Kay Hameyer [23], but that is not considered in this paper. Therefore, based on the analysis using the Newton-Raphson method, a simultaneous scheme is likely to be faster than an iteratively staggered scheme.

4.2 Combination of the FFT-based Scheme and the Coupling Schemes

In this section, the entire algorithm to combine the algorithm of the FFT-based scheme and that of a coupling scheme is discussed. H. Moulinec and P. Suquet [1] proposed the extension of the FFT-based scheme to incorporate nonlinear constituents. They suggested to couple the FFT-based scheme and nonlinear constituents in an iteratively staggered manner in a loading step. In their work, for a given macroscopic strain ϵ_0, the iteratively staggered scheme is used to update the fields of the strain, stress and the plastic strain. Analogously, in the current research, inside an iterative loop, the FFT-based scheme is used to update the field of the deformation gradient firstly. Secondly, the fields of the nonlocal damage variable $\bar{D}$ and the local one D are updated using one of the aforementioned coupling schemes. Finally, the convergence criteria of the FFT-based scheme and the damage fields are checked. This procedure of the iteratively staggered scheme can be simply summarized as follows:

Algorithm 6 The combination of the FFT-based scheme and a coupling scheme

1: **procedure** FFT-BASED SCHEME + COUPLING SCHEME
2: **Initialization:** Load previous field quantities for initial guesses, $\mathbf{F}_0^{n+1} = \mathbf{F}^n$, $\bar{D}_0^{n+1} = \bar{D}^n$, and $D_0^{n+1} = D^n$.
3: **Repeat:**
4: (a) Run the FFT-based scheme, algorithm 1, to update $\mathbf{F}_{i+1}^{n+1}$.
5: (b) Calculate $\bar{D}_{i+1}^{n+1}$ and D_{i+1}^{n+1} using one of the coupling schemes.
6: (c) Check the convergence criteria: $\mathrm{Div}(\mathbf{P}^{i+1}(\boldsymbol{x})) = \mathbf{0}$ and $\bar{D}^{n+1} - \alpha\nabla^2\bar{D}^{n+1} - D^{n+1} < \mathrm{tol}\ \forall \boldsymbol{x} \in \Omega$.
7: **if** Convergence **then**
8: **return** $\mathbf{F}_{i+1}^{n+1}$, $\bar{D}_{i+1}^{n+1}$, and D_{i+1}^{n+1}.
9: **else**
10: (c) $i = i + 1$ and go to step (a).

4.3 Implementations of the Coupling Schemes

In this section, implementations of the coupling schemes are discussed. The following implementations are supposed to be placed at step (b) in algorithm 6. On top of that, validations and investigations of these coupling schemes are presented.

4.3.1 Staggered Scheme

4.3.1.1 Basic Idea

The basic idea of the staggered scheme is to arrange the solution techniques for the micromorphic balance equation and the KKT conditions in a sequential manner. Since the nonlocal damage variable $\bar{D}$ has an impact on the local damage D, the micromorphic balance equation is solved for the field of $\bar{D}$ firstly while that of D is kept fixed. Then, the solution procedure to solve the KKT conditions for the local damage D follows. The micromorphic balance equation is solved using the spectral method which is presented in the next section. In order to calculate the increment of D at each grid point, the Newton-Raphson method described in algorithm 7 is used.

4.3.1.2 The Spectral Method to Solve the Micromorphic Balance Equation Defined on a RVE

A systematic approach to solve the micromorphic balance equation (3.29) for the nonlocal damage variable $\bar{D}$ is suggested. To solve the equation, M. Boeff et al. used a semi-implicit method to express the nonlocal damage field $\bar{D}$ in terms of the local damage field D in Fourier space, [24]. In the same manner, the micromorphic balance equation can be expressed in Fourier space. The solution procedure is given by:

$$\begin{aligned} \hat{D}(\boldsymbol{\xi}) &= \mathrm{FFT}(D(\boldsymbol{x})) \quad \forall \boldsymbol{x} \in \Omega \\ \hat{\bar{D}}(\boldsymbol{\xi}) &= \frac{1}{1+\alpha|\boldsymbol{\xi}|^2}\hat{D}(\boldsymbol{\xi}) \\ \bar{D}(\boldsymbol{x}) &= \mathrm{FFT}^{-1}(\hat{\bar{D}}(\boldsymbol{\xi})) \quad \forall \boldsymbol{x} \in \Omega \end{aligned} \tag{4.5}$$

where the internal length scale α is a constant in the spatial domain Ω. The definition of the wave vector $\boldsymbol{\xi}$ comes from equation (2.33). After the nonlocal damage field is solved in Fourier space, a backward fast Fourier transform is performed on the nonlocal damage field to express it in real space. Finally, the solution of the micromorphic balance equation $\bar{D}$ is obtained in real space.

4.3.1.3 The Return-Mapping Algorithm for the Nonlocal Damage Model

The KKT conditions are expressed in terms of the thermodynamic conjugate forces and the damage loading function. The thermodynamic conjugate forces for the micromorphic approach in equation (3.28) are used to define the damage loading function ϕ_{nloc} for the nonlocal model. The thermodynamic conjugate forces for the nonlocal model in equation (3.28) are denoted by Y_{nloc} and q_d respectively. In algorithm 7, these thermodynamic forces and the damage loading function are used for calculating an increment of the damage multiplier. The return-mapping algorithm for the local damage model, algorithm 2, is extended to the case of the nonlocal damage model. The return-mapping algorithm for the nonlocal damage model, algorithm 7, is introduced as follows:

Algorithm 7 The Return-Mapping Algorithm for the Nonlocal Damage Model

procedure NEWTON-RAPHSON METHOD
  Initialization: Load previous state variables.
    $\Delta\lambda = 0.$
    $\Delta(\Delta\lambda)_0 = 0.$
    $D_0^{n+1} = D.$
    $\xi_{d,0}^{n+1} = \xi_d.$
    $\bar{D} = \bar{D}.$
  Iterate i+1 Seek the increment of $\Delta\lambda$ and update D and ξ_d.
    (a) Update $\Delta\lambda_{i+1} = \Delta\lambda_i + \Delta(\Delta\lambda)_i$.
    (b) Update D and ξ_d. $D_{i+1}^{n+1} = D_0^{n+1} + \Delta\lambda_{i+1}$, $\xi_{d,i+1}^{n+1} = \xi_d^{n+1} + \Delta\lambda_{i+1}$.
    (c) Calculate the residual $||\phi_{nloc,i+1}(D_{i+1}^{n+1}, \xi_{i+1}^{n+1}, \bar{D})|| = Y_{nloc} - q_d$
  if $||\phi_{nloc,i+1}|| < \text{tolerance}$ **then return** D_{i+1}^{n+1} and ξ_{i+1}^{n+1}.
  else
    (d) Calculate $K_{nloc} = \frac{\partial \phi_{nloc,i+1}}{\partial \Delta\lambda} = \frac{\partial Y_{nloc,i+1}}{\partial D}\frac{\partial D}{\partial \Delta\lambda} - \frac{\partial q_{d,i+1}}{\partial \xi_d}\frac{\partial \xi_d}{\partial \Delta\lambda}$.
    (e) Calculate $\Delta(\Delta\lambda)_{i+1} = -\frac{\phi_{nloc,i+1}}{K_{nloc}}$.
    (f) $i = i + 1$ and repeat the algorithm from step (a).

4.3.1.4 The Algorithm

By combining algorithm 7 and the FFT-based solution technique for the micromorphic equation (4.5), the staggered scheme for coupling the micromorphic balance equation and the KKT conditions is given as follows:

Algorithm 8 Staggered Scheme for coupling of damage fields

procedure STAGGERED SCHEME
  Initialization: Load previous values of $D, \bar{D}$.
    (a) Solve equation $\bar{D}^{n+1} - \alpha\nabla^2\bar{D}^{n+1} = D^{n+1}$ for $\bar{D}^{n+1}$ using equations (4.5).
    (b) Run algorithm 7 to check and update local damage evolution, D^{n+1}.
    (c) Return $\bar{D}^{n+1}$ and D^{n+1}.

4.3.2 Iteratively Staggered Scheme

4.3.2.1 Basic Idea and Algorithm

An iteratively staggered scheme can be constructed by iterating the staggered scheme 8 until a coupling condition is satisfied. The coupling conditions should be set to ensure that

all of the coupled fields satisfy every numerical model. The coupling condition at every step in the iteratively staggered scheme reads as follows:

$$\begin{aligned} \phi_d &< \text{tolerance} \quad \text{in}\,\Omega \\ \bar{D} - \alpha\nabla^2\bar{D} - D &< \text{tolerance} \quad \text{in}\,\Omega \end{aligned} \tag{4.6}$$

where Ω is the spatial domain of a RVE and tolerance is a small positive value. The coupling conditions should be valid for every grid point in a RVE. However, the coupling condition can be further simplified. In order to simplify the coupling condition, the KKT conditions are solved firstly, and then the solution of the micromorphic balance equation is computed. When the sequence of solutions is arranged in this manner, the convergence of the local damage field yields the convergence of the nonlocal damage field. At the end of i-th step in the iteratively staggered scheme, the following relation is valid in Fourier space

$$\hat{\bar{D}}_i = \frac{1}{1+\alpha|\boldsymbol{\xi}|^2}\hat{D}_i \tag{4.7}$$

When the local damage field is converged at the $(i+1)$-th step, $\hat{D}_i$ and $\hat{D}_{i+1}$ are the same. Likewise, in Fourier space, the following relation is satisfied:

$$\hat{\bar{D}}_{i+1} = \frac{1}{1+\alpha|\boldsymbol{\xi}|^2}\hat{D}_{i+1} \tag{4.8}$$

As α and $\boldsymbol{\xi}$ are the same in the i-th and the $(i+1)$-th step, $\hat{\bar{D}}_{i+1}$ and $\hat{\bar{D}}_i$ are the same as well. Thus, it is only necessary to check the convergence of the local damage field. The simplified coupling condition reads as follows:

$$\phi_d < \text{tolerance} \quad \text{in}\,\Omega \tag{4.9}$$

The algorithm of the iteratively staggered scheme reads as follows:

Algorithm 9 Iteratively Staggered Scheme for Coupling Damage Fields

1: **procedure** ITERATIVELY STAGGERED SCHEME
2: **Initialization:** Take initial guesses from previous values $D_0^{n+1} = D$, $\xi_0^{n+1} = \xi$, and $\bar{D}_0^{n+1} = \bar{D}$.
3: **Repeat:**
4: (a) Run algorithm (7) to calculate $(D_{i+1}^{n+1}, \xi_{d,i+1}^{n+1})$ from $(D_i^{n+1}, \xi_{d,i}^{n+1}, \bar{D}_i^{n+1})$.
5: (b) Solve equation $\bar{D}_{i+1}^{n+1} - \alpha\nabla^2\bar{D}_{i+1}^{n+1} = D_{i+1}^{n+1}$ for $\bar{D}_{i+1}^{n+1}$ using equations (4.5).
6: **if** Coupling condition (4.9) is fulfilled **then**
7: **return** $(D_{i+1}^{n+1}, \xi_{d,i+1}^{n+1}, \bar{D}_{i+1}^{n+1})$.
8: **else**
9: (c) $i = i+1$ and repeat the algorithm from step (a).

4.3.3 Simultaneous Scheme

4.3.3.1 Basic Idea

Finally, the simultaneous scheme comes into play in order to calculate the increments of the local and the nonlocal damage variables satisfying the KKT conditions (3.11) and the micromorphic balance equation (3.29) at the same time. A set of simultaneous equations can be constructed from these two models in order to calculate the fields of local and nonlocal damage. In general, for a heterogeneous microstructure, there are two elastic-damage loading scenarios. One is that damage-loading takes place at every grid point. The other one is the case where damage-loading takes place only at certain grid points while other points are going through purely elastic deformations. For clear explanations, firstly, the implementation of the simultaneous scheme is introduced for the first scenario. Next, the implementation for the second scenario is discussed.

4.3.3.2 Formulations of the Residual Vector and the Vector of Increments

To begin with, the first scenario that damage-loading takes place at every grid point is investigated. Two types of residuals are derived from the micromorphic balance equation (3.29) and the KKT conditions (3.11). At every grid point, one residual denoted as r_1 can be formulated from the micromorphic balance equation. The other one denoted as r_2 is derived from the damage loading function in the KKT conditions since the damage loading function should be zero when damage evolution takes place. The definitions of the thermodynamic conjugate forces for the nonlocal damage model are given in equation (3.28). The thermodynamic conjugate forces are denoted by Y_{nloc} and q_d in this section. At each grid point going through a damage-loading process, these two residuals are given by:

$$\begin{aligned} r_1(D, \bar{D}) &= \bar{D} - \alpha \nabla^2 \bar{D} - D = 0 \\ r_2(D, \xi_d, \bar{D}) = \phi_{nloc} &= Y_{nloc}(D, \bar{D}) - (Y_0 + q_d(\xi_d)) = 0 \end{aligned} \tag{4.10}$$

In the above equations (4.10), three state variables D, ξ_d and $\bar{D}$ are involved in r_1 and r_2. The number the increments of the state variables can be further reduced to two, $\Delta\bar{D}$ and $\Delta\lambda$. The damage evolution equations (3.10) are reviewed below:

$$\begin{aligned} \dot{D} &= \dot{\lambda} \frac{\partial \phi_d}{\partial Y} = \dot{\lambda} \\ \dot{\xi_d} &= -\dot{\lambda} \frac{\partial \phi_d}{\partial q_d} = \dot{\lambda} \end{aligned} \tag{4.11}$$

The damage evolution equations (3.10) imply that the increments of D and ξ_d are the same with that of λ. By taking this into account, the damage and damage hardening variables at $(n+1)$-th loading step are expressed in terms of those at n-th loading step

$$\begin{aligned} D^{n+1} &= D^n + \Delta D = D^n + \Delta\lambda \\ {\xi_d}^{n+1} &= {\xi_d}^n + \Delta\xi_d = {\xi_d}^n + \Delta\lambda \end{aligned} \tag{4.12}$$

where ΔD, $\Delta\xi_d$, and $\Delta\lambda$ are the increments of D, ξ_d, and λ respectively. By using equations (4.12), the increments of D and ξ_d are simply expressed in terms of $\Delta\lambda$. At the same time, $\bar{D}$ at $(n+1)$-th step can be expressed in the same manner

$$\bar{D}^{n+1} = \bar{D}^n + \Delta\bar{D} \tag{4.13}$$

Consequently, the simultaneous scheme is constructed to calculate $\Delta\lambda$ and $\Delta\bar{D}$ in order to update the state variables.

The indexing of each grid point follows the notations in Table 2.1. Residuals at a grid point, $r_{1,(i,j,k)}$ and $r_{2,(i,j,k)}$, can be assembled into one residual vector. The definition of the residual vector of an entire spatial domain reads as follows:

$$\boldsymbol{r}(\bar{\boldsymbol{D}}, \boldsymbol{D}, \boldsymbol{\xi_d}) = \begin{pmatrix} \boldsymbol{r}_1 \\ \boldsymbol{r}_2 \end{pmatrix} = \begin{pmatrix} r_{1,(0,0,0)} \\ r_{1,(0,0,1)} \\ \vdots \\ r_{1,(0,0,N_z-1)} \\ \vdots \\ r_{1,(N_x-1,N_y-1,N_z-1)} \\ \cdots\cdots\cdots \\ r_{2,(0,0,0)} \\ r_{2,(0,0,1)} \\ \vdots \\ r_{2,(0,0,N_z-1)} \\ \vdots \\ r_{2,(N_x-1,N_y-1,N_z-1)} \end{pmatrix} \in \mathbb{R}^{2(N_x N_y N_z)} \tag{4.14}$$

Likewise, the increment vector of state variables $\boldsymbol{x}$ can be represented as follows:

$$\boldsymbol{x} = \begin{pmatrix} \boldsymbol{\Delta \bar{D}} \\ \boldsymbol{\Delta \lambda} \end{pmatrix} = \begin{pmatrix} \Delta \bar{D}_{(0,0,0)} \\ \Delta \bar{D}_{(0,0,1)} \\ \vdots \\ \Delta \bar{D}_{(0,0,N_z-1)} \\ \vdots \\ \Delta \bar{D}_{(N_x-1,N_y-1,N_z-1)} \\ \cdots\cdots\cdots \\ \Delta \lambda_{(0,0,0)} \\ \Delta \lambda_{(0,0,1)} \\ \vdots \\ \Delta \lambda_{(0,0,N_z-1)} \\ \vdots \\ \Delta \lambda_{(N_x-1,N_y-1,N_z-1)} \end{pmatrix} \in \mathbb{R}^{2(N_x N_y N_z)} \tag{4.15}$$

The increment vector $\boldsymbol{x}$ is composed of the increment vector of the nonlocal damage variable $\Delta \bar{\boldsymbol{D}}$ and that of the damage multiplier $\Delta \boldsymbol{\lambda}$. As a result, the solution of the coupled problem is defined as the increment vector $\boldsymbol{x}$ (4.15) which makes the residual vector $\boldsymbol{r}$ (4.14) a zero vector.

4.3.3.3 Application of the Newton-Raphson Method

The Newton-Raphson method is used to find the increments of the state variables satisfying the equation $\boldsymbol{r}(\Delta \bar{\boldsymbol{D}}, \Delta \boldsymbol{\lambda}) = \boldsymbol{0}$. The initial guess of the increment vector $\boldsymbol{x}_0$ is initialized with a zero vector. In the iterative procedure of the Newton-Raphson method, at i-th step, the residual vector $\boldsymbol{r}_i$ is calculated using the increment vector $\boldsymbol{x}_i$. The partial derivative of $\boldsymbol{r}_i$ with respect to $\boldsymbol{x}_i$ should be calculated to construct a Jacobian matrix $\left.\frac{d\boldsymbol{r}}{d\boldsymbol{x}}\right|_i$ which is necessary to calculate an increment of the increment vector $\Delta \boldsymbol{x}_i$. The increment vector at $(i+1)$-th step is calculated by adding $\Delta \boldsymbol{x}_i$ to $\boldsymbol{x}_i$, $\boldsymbol{x}_{i+1} = \boldsymbol{x}_i + \Delta \boldsymbol{x}_i$. Then, the residual vector $\boldsymbol{r}_{i+1}$ is calculated, and the convergence is checked. The aforementioned relations

are summarized as follows:

$$\begin{aligned}
\boldsymbol{x}_0 &= \mathbf{0} \\
\boldsymbol{x}_{i+1} &= \boldsymbol{x}_i + \Delta\boldsymbol{x}_i \\
\boldsymbol{r}_{i+1} &= \boldsymbol{r}_i + \left(\frac{d\boldsymbol{r}}{d\boldsymbol{x}}\right)\Big|_i \Delta\boldsymbol{x}_i = \mathbf{0} \\
\Delta\boldsymbol{x}_i &= -\left(\frac{d\boldsymbol{r}}{d\boldsymbol{x}}\right)^{-1}\Big|_i \Delta\boldsymbol{r}_i \\
\Delta\boldsymbol{x}_i = \begin{pmatrix} \Delta(\Delta\bar{\boldsymbol{D}}) \\ \Delta(\Delta\boldsymbol{\lambda}) \end{pmatrix}\Bigg|_i &= -\begin{pmatrix} \frac{\partial \boldsymbol{r}_1}{\partial \Delta\bar{\boldsymbol{D}}} & \frac{\partial \boldsymbol{r}_1}{\partial \Delta\boldsymbol{\lambda}} \\ \frac{\partial \boldsymbol{r}_2}{\partial \Delta\bar{\boldsymbol{D}}} & \frac{\partial \boldsymbol{r}_2}{\partial \Delta\boldsymbol{\lambda}} \end{pmatrix}^{-1}\Bigg|_i \begin{pmatrix} \boldsymbol{r}_1 \\ \boldsymbol{r}_2 \end{pmatrix}\Bigg|_i
\end{aligned} \tag{4.16}$$

The Jacobian matrix $\frac{d\boldsymbol{r}}{d\boldsymbol{x}}\Big|_i$ can be split into four submatrices. The Jacobian matrix and its submatrices are described as follows:

$$\frac{d\boldsymbol{r}}{d\boldsymbol{x}}\Big|_i = \begin{pmatrix} \frac{\partial \boldsymbol{r}_1}{\partial \Delta\bar{\boldsymbol{D}}} & \frac{\partial \boldsymbol{r}_1}{\partial \Delta\boldsymbol{\lambda}} \\ \frac{\partial \boldsymbol{r}_2}{\partial \Delta\bar{\boldsymbol{D}}} & \frac{\partial \boldsymbol{r}_2}{\partial \Delta\boldsymbol{\lambda}} \end{pmatrix}\Bigg|_i \in \mathbb{R}^{(2N_xN_yN_z)\times(2N_xN_yN_z)} \tag{4.17}$$

where these four submatrices in equation (4.17) are $(N_xN_yN_z)$ by $(N_xN_yN_z)$ matrices. In equation (4.17), $\boldsymbol{r}_1$, $\boldsymbol{r}_2$, $\Delta\bar{\boldsymbol{D}}$, and $\Delta\boldsymbol{\lambda}$ are vectors of corresponding residuals and the increments in equations (4.14) and (4.15) respectively.

4.3.3.4 Calculations of the Residual Vector and the Jacobian Matrix

Firstly, at each grid point, the partial derivatives of r_1 with respect to $\Delta\bar{D}$ and $\Delta\lambda$ are investigated. At a grid point with index (i, j, k), the residuals are written as follows:

$$r_1(D_{(i,j,k)}, \bar{D}_{(i,j,k)}) = \bar{D}_{(i,j,k)} - \alpha\nabla^2\bar{D}_{(i,j,k)} - D_{(i,j,k)} = 0 \tag{4.18}$$

$$r_2(D_{(i,j,k)}, \xi_{d,(i,j,k)}, \bar{D}_{(i,j,k)}) = \phi_{nloc,(i,j,k)} = Y_{nloc,(i,j,k)} - (Y_{0,(i,j,k)} + q_{d,(i,j,k)}) = 0 \tag{4.19}$$

In order to calculate the value of r_1 and the derivative of r_1 with respect to $\Delta\bar{D}$, the Laplacian ∇^2 should be approximated using the central finite difference scheme. In three-dimensional space, the approximation of $\nabla^2\bar{D}_{(i,j,k)}$ reads as follows:

$$\begin{aligned}
\nabla^2\bar{D}_{(i,j,k)} = \frac{\bar{D}_{(i-1,j,k)} - 2\bar{D}_{(i,j,k)} + \bar{D}_{(i+1,j,k)}}{dx^2} + \frac{\bar{D}_{(i,j-1,k)} - 2\bar{D}_{(i,j,k)} + \bar{D}_{(i,j+1,k)}}{dy^2} \\
+ \frac{\bar{D}_{(i,j,k-1)} - 2\bar{D}_{(i,j,k)} + \bar{D}_{(i,j,k+1)}}{dz^2}
\end{aligned} \tag{4.20}$$

where dx, dy, and dz stand for grid spacing in each direction, Table 2.1. The visualization of the stencil of the approximation (4.20) is found in reference [25]:

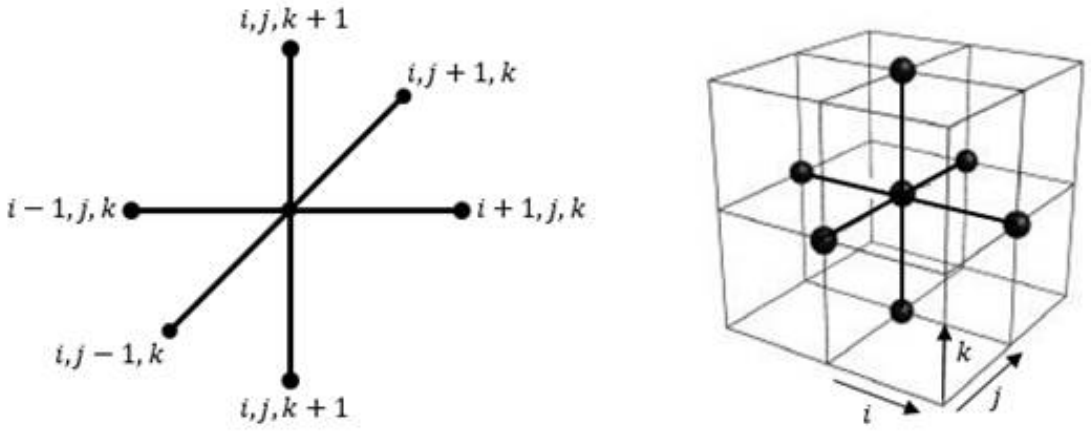

FIGURE 4.1: Stencil of the central finite difference scheme (4.20).

By plugging (4.20) into (4.18), r_1 at a grid point (i, j, k) reads as follows:

$$\begin{aligned} r_{1,(i,j,k)} = -\alpha\Big(&\frac{\bar{D}_{(i-1,j,k)} + \bar{D}_{(i+1,j,k)}}{dx^2} + \frac{\bar{D}_{(i,j-1,k)} + \bar{D}_{(i,j+1,k)}}{dy^2} \\ &+ \frac{\bar{D}_{(i,j,k-1)} + \bar{D}_{(i,j,k+1)}}{dz^2}\Big) + \Big(1 + \frac{2\alpha}{dx^2} + \frac{2\alpha}{dy^2} + \frac{2\alpha}{dz^2}\Big)\bar{D}_{(i,j,k)} - D_{(i,j,k)} \end{aligned} \tag{4.21}$$

where the approximation of $-\alpha\nabla^2\bar{D}_{(i,j,k)}$ reads as follows:

$$\begin{aligned} -\alpha\nabla^2\bar{D}_{(i,j,k)} \approx -\alpha\Big(&\frac{\bar{D}_{(i-1,j,k)} + \bar{D}_{(i+1,j,k)}}{dx^2} + \frac{\bar{D}_{(i,j-1,k)} + \bar{D}_{(i,j+1,k)}}{dy^2} \\ &+ \frac{\bar{D}_{(i,j,k-1)} + \bar{D}_{(i,j,k+1)}}{dz^2}\Big) + \Big(\frac{2\alpha}{dx^2} + \frac{2\alpha}{dy^2} + \frac{2\alpha}{dz^2}\Big)\bar{D}_{(i,j,k)} \end{aligned} \tag{4.22}$$

Each row of the submatrix $\frac{\partial \boldsymbol{r}_1}{\partial \Delta \bar{\boldsymbol{D}}}$ can be derived from differentiating $r_{1,(i,j,k)}$ with respect to $\Delta\bar{D}_{(i,j,k)}, \Delta\bar{D}_{(i+1,j,k)}, \Delta\bar{D}_{(i-1,j,k)}, \cdots$, and $\Delta\bar{D}_{(i+1,j+1,k+1)}$. The shape of $\frac{\partial \boldsymbol{r}_1}{\partial \Delta \bar{\boldsymbol{D}}}$ is generated from the approximation of the Laplacian using the central finite difference scheme. Considering (4.21), the partial derivative of $r_{1,(i,j,k)}$ with respect to $\Delta\bar{D}_{(i,j,k)}$ forms an identity matrix $\mathbf{I}$ in the submatrix $\frac{\partial \boldsymbol{r}_1}{\partial \Delta \bar{\boldsymbol{D}}}$. In general, since the Laplacian is always symmetric and negative-definite, $\frac{\partial \boldsymbol{r}_1}{\partial \Delta \bar{\boldsymbol{D}}} = \mathbf{I} - \alpha\nabla^{\mathbf{2}}$ should be a symmetric and positive-definite matrix when the internal length scale α is a positive constant over a RVE. That is because $\mathbf{I}$ and $-\alpha\nabla^{\mathbf{2}}$ are positive-definite matrices. From equations (4.12) and the chain rule, the following relations at every grid point can be derived:

$$\begin{aligned} \frac{\partial D}{\partial \Delta\lambda} &= 1 \\ \frac{\partial \xi_d}{\partial \Delta\lambda} &= 1 \\ \frac{\partial r_1}{\partial \Delta\lambda} = \frac{\partial r_1}{\partial D}\frac{\partial D}{\partial \Delta\lambda} &= -1 \end{aligned} \tag{4.23}$$

Therefore, the submatrix $\frac{\partial \boldsymbol{r}_1}{\partial \Delta \boldsymbol{\lambda}}$ is a scalar matrix where the main diagonal entries are -1. Two submatrices derived by differentiating $\boldsymbol{r}_1$ are summarized as follows:

$$\begin{aligned} \frac{\partial \boldsymbol{r}_1}{\partial \Delta \bar{\boldsymbol{D}}} &= \mathbf{I} - \alpha \nabla^{\mathbf{2}} \\ \frac{\partial \boldsymbol{r}_1}{\partial \Delta \boldsymbol{\lambda}} &= -\mathbf{I} \end{aligned} \tag{4.24}$$

In order to formulate submatrices which are the partial derivatives of $\boldsymbol{r_2}$, the definitions of the thermodynamic conjugate forces are revisited. In equation, (3.28), the thermodynamic conjugate forces are defined as follows:

$$\begin{aligned} Y_{nloc} := -\frac{\partial \Psi}{\partial D} = -f'(D)[\frac{\mu}{2}\{\mathrm{tr}\mathbf{C} - 3 - \ln(\mathrm{det}\mathbf{C})\} + \frac{\Lambda}{4}\{\mathrm{det}\mathbf{C} - 1 - \ln(\mathrm{det}\mathbf{C})\}] - H(D - \bar{D}) \\ q_d := \frac{\partial \Psi}{\partial \xi_d} = r\{1 - \exp(-s\xi_d)\} \end{aligned} \tag{4.25}$$

At each grid point, the partial derivatives of r_2 with respect to the vectors, $\Delta \bar{\boldsymbol{D}}$ and $\Delta \boldsymbol{\lambda}$, can be derived by the following procedure:

$$\begin{aligned} \frac{\partial r_{2,(i,j,k)}}{\partial \Delta \bar{\boldsymbol{D}}} &= \frac{\partial Y_{nloc,(i,j,k)}}{\partial \Delta \bar{D}_{(i,j,k)}} = H \\ \frac{\partial r_{2,(i,j,k)}}{\partial \Delta \boldsymbol{\lambda}} &= \frac{\partial Y_{nloc,(i,j,k)}}{\partial \Delta \lambda_{(i,j,k)}} - \frac{\partial q_{d,(i,j,k)}}{\partial \Delta \lambda_{(i,j,k)}} = K_{nloc,(i,j,k)} \end{aligned} \tag{4.26}$$

where K_{nloc} is defined at each grid point as follows:

$$\begin{aligned} K_{nloc} &= \frac{\partial Y_{nloc}}{\partial D}\frac{\partial D}{\partial \Delta \lambda} - \frac{\partial q_d}{\partial \xi_d}\frac{\partial \xi_d}{\partial \Delta \lambda} \\ \Leftrightarrow -f''(D)[\frac{\mu}{2}\{\mathrm{tr}\mathbf{C} - 3 - \ln(\mathrm{det}\mathbf{C})\} + \frac{\lambda}{4}\{\mathrm{det}\mathbf{C} - 1 - \ln(\mathrm{det}\mathbf{C})\}] - (rs)\exp(-s\xi_d) - H \end{aligned} \tag{4.27}$$

Finally, it is concluded that $\frac{\partial \boldsymbol{r_2}}{\partial \Delta \bar{\boldsymbol{D}}}$ is a scalar matrix, $H\mathbf{I}$. The last submatrix $\frac{\partial \boldsymbol{r_2}}{\partial \Delta \boldsymbol{\lambda}}$ is a diagonal matrix having K_{nloc} calculated at each grid point. In summary, these four submatrices are summarized as follows:

Submatrix	Definition
$\frac{\partial \boldsymbol{r}_1}{\partial \Delta \bar{\boldsymbol{D}}}$	Approximation of $\mathbf{I} - \alpha\nabla^2$ using the central finite difference scheme
$\frac{\partial \boldsymbol{r}_1}{\partial \Delta \boldsymbol{\lambda}}$	$\frac{\partial \boldsymbol{r}_1}{\partial \Delta \boldsymbol{\lambda}} = \mathrm{diag}(-1)$
$\frac{\partial \boldsymbol{r_2}}{\partial \Delta \bar{\boldsymbol{D}}}$	$\frac{\partial \boldsymbol{r_2}}{\partial \Delta \bar{\boldsymbol{D}}} = \mathrm{diag}(H)$
$\frac{\partial \boldsymbol{r_2}}{\partial \Delta \boldsymbol{\lambda}}$	$\frac{\partial \boldsymbol{r_2}}{\partial \Delta \boldsymbol{\lambda}} = \mathrm{diag}(K_{nloc})$

TABLE 4.2: Submatrices of the Jacobian matrix $\frac{d\boldsymbol{r}}{d\boldsymbol{x}}$.

Only the first submatrix $\frac{\partial \boldsymbol{r}_1}{\partial \Delta \bar{\boldsymbol{D}}}$ is symmetric and positive-definite, and the others are diagonal matrices. For example, the shape of the Jacobian matrix for a one dimensional problem is

displayed

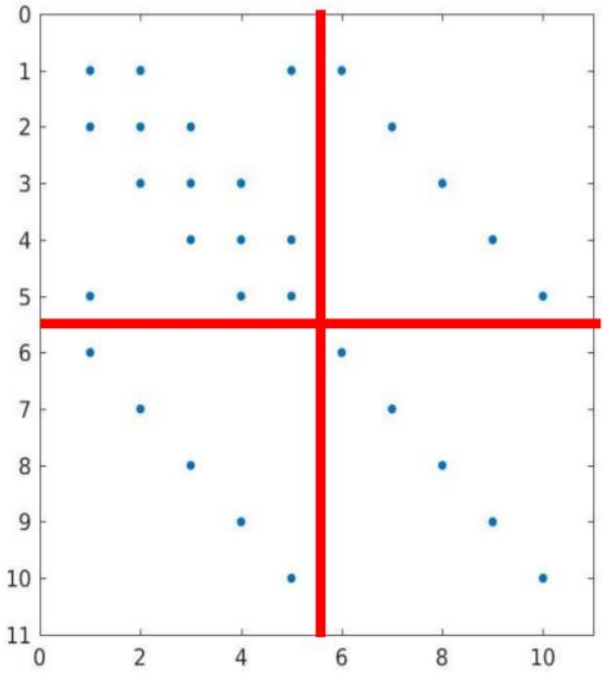

FIGURE 4.2: Blue dots represent nonzero entities in the Jacobian matrix $\frac{d\boldsymbol{r}}{d\boldsymbol{x}}$ in equation (4.17). Each submatrix in a quadrant corresponds to $\frac{\partial \boldsymbol{r}_1}{\partial \Delta \boldsymbol{\lambda}}$, $\frac{\partial \boldsymbol{r}_1}{\partial \Delta \tilde{\boldsymbol{D}}}$, $\frac{\partial \boldsymbol{r}_2}{\partial \Delta \tilde{\boldsymbol{D}}}$, and $\frac{\partial \boldsymbol{r}_2}{\partial \Delta \boldsymbol{\lambda}}$.

where $N_x = 10, N_y = 1, N_z = 1$, and the red cross distinguishes the submatrices.

4.3.3.5 Application of a Sparse Matrix Form and the Schur Complement Method

The simultaneous scheme is developed to solve the linear equation (4.16) in an iterative manner until convergence is achieved. In practice, saving all entities of the Jacobian matrix consumes a huge amount of memory. For example, for a 2D grid having grid points in each dimension $(N_x, N_y, N_z) = (64, 64, 1)$, $(64 \times 64 \times 1 \times 2)^2 \times (8)/2^{20} = 512$ Megabytes are necessary to store the entire Jacobian matrix in double precision. To save memory occupation, expressing the Jacobian matrix in a sparse format will save a huge amount of memory. For this reason, the Compressed Sparse Row (CSR) format comes into play to express the Jacobian matrix in a program. Details of the CSR format can be found in Appendix A.

The Jacobian matrix is asymmetric because $\frac{\partial \boldsymbol{r}_1}{\partial \Delta \boldsymbol{\lambda}}$ and $\frac{\partial \boldsymbol{r}_2}{\partial \Delta \tilde{\boldsymbol{D}}}$ are different. Iterative methods like GMRES can come into play to solve this asymmetric matrix. Nevertheless, considering $\frac{\partial \boldsymbol{r}_1}{\partial \Delta \tilde{\boldsymbol{D}}}$ is symmetric and the other submatrices are diagonal, the Jacobian matrix can be transformed into a smaller symmetric one by means of the Schur complement method. By using the Schur complement method, not only the size of the Jacobian matrix reduces, but

also the symmetric nature can accelerate iterative solvers to converge faster. The general form of the Schur complement method for a linear equation and its solution reads as follows:

$$\begin{aligned} \begin{pmatrix} \mathbf{A}_{11} & \mathbf{A}_{12} \\ \mathbf{A}_{21} & \mathbf{A}_{22} \end{pmatrix} \begin{pmatrix} \boldsymbol{\Delta x}_1 \\ \boldsymbol{\Delta x}_2 \end{pmatrix} &= - \begin{pmatrix} \boldsymbol{r}_1 \\ \boldsymbol{r}_2 \end{pmatrix} \\ \boldsymbol{\Delta x}_1 = \{\mathbf{A}_{11} - \mathbf{A}_{12}(\mathbf{A}_{22})^{-1}\mathbf{A}_{21}\}^{-1}\{-\boldsymbol{r}_1 + \mathbf{A}_{12}(\mathbf{A}_{22})^{-1}\boldsymbol{r}_2\} \\ \boldsymbol{\Delta x}_2 = -(\mathbf{A}_{22})^{-1}(\boldsymbol{r}_2 + \mathbf{A}_{21}\boldsymbol{\Delta x}_1) \end{aligned} \tag{4.28}$$

The matrix $\{\mathbf{A}_{11} - \mathbf{A}_{12}(\mathbf{A}_{22})^{-1}\mathbf{A}_{21}\}^{-1}\{-\boldsymbol{r}_1 + \mathbf{A}_{12}(\mathbf{A}_{22})^{-1}\boldsymbol{r}_2\}$ is called the "Schur complement matrix". Submatrices and vectors in the simultaneous scheme (4.16) can be mapped to those of the Schur complement method (4.28). The corresponding terms are summarized in Table 4.3

Simultaneous scheme	Schur complement method
$\frac{\partial \boldsymbol{r}_1}{\partial \Delta \bar{\boldsymbol{D}}}$	$\mathbf{A}_{11}$
$\frac{\partial \boldsymbol{r}_1}{\partial \Delta \boldsymbol{\lambda}}$	$\mathbf{A}_{12}$
$\frac{\partial \boldsymbol{r}_2}{\partial \Delta \bar{\boldsymbol{D}}}$	$\mathbf{A}_{21}$
$\frac{\partial \boldsymbol{r}_2}{\partial \Delta \boldsymbol{\lambda}}$	$\mathbf{A}_{22}$
$\Delta(\Delta \bar{\boldsymbol{D}})$	$\boldsymbol{\Delta x}_1$
$\Delta(\Delta \boldsymbol{\lambda})$	$\boldsymbol{\Delta x}_2$

TABLE 4.3: Similarities between equations (4.16) and (4.28).

By applying the Schur complement method (4.28), the increment of the increment vector of the nonlocal damage $\Delta(\Delta \bar{\boldsymbol{D}})$ is calculated firstly, and then that of the damage multiplier $\Delta(\Delta \boldsymbol{\lambda})$ is calculated from $\Delta(\Delta \bar{\boldsymbol{D}})$. By using the Schur complement method, $\Delta(\Delta \bar{\boldsymbol{D}})$ is given by:

$$\Delta(\Delta \bar{\boldsymbol{D}}) = \Big\{ \frac{\partial \boldsymbol{r}_1}{\partial \Delta \bar{\boldsymbol{D}}} - \frac{\partial \boldsymbol{r}_1}{\partial \Delta \boldsymbol{\lambda}} \Big(\frac{\partial \boldsymbol{r}_2}{\partial \Delta \boldsymbol{\lambda}} \Big)^{-1} \frac{\partial \boldsymbol{r}_2}{\partial \Delta \bar{\boldsymbol{D}}} \Big\}^{-1} \Big\{ -\boldsymbol{r}_1 + \frac{\partial \boldsymbol{r}_1}{\partial \Delta \boldsymbol{\lambda}} \Big(\frac{\partial \boldsymbol{r}_2}{\partial \Delta \boldsymbol{\lambda}} \Big)^{-1} \boldsymbol{r}_2 \Big\} \tag{4.29}$$

where

$$\begin{aligned} \Big\{ \frac{\partial \boldsymbol{r}_1}{\partial \Delta \bar{\boldsymbol{D}}} - \frac{\partial \boldsymbol{r}_1}{\partial \Delta \boldsymbol{\lambda}} \Big(\frac{\partial \boldsymbol{r}_2}{\partial \Delta \boldsymbol{\lambda}} \Big)^{-1} \frac{\partial \boldsymbol{r}_2}{\partial \Delta \bar{\boldsymbol{D}}} \Big\}^{-1} &\in \mathbb{R}^{(N_x N_y N_z) \times (N_x N_y N_z)} \\ \Big\{ -\boldsymbol{r}_1 + \frac{\partial \boldsymbol{r}_1}{\partial \Delta \boldsymbol{\lambda}} \Big(\frac{\partial \boldsymbol{r}_2}{\partial \Delta \boldsymbol{\lambda}} \Big)^{-1} \boldsymbol{r}_2 \Big\} &\in \mathbb{R}^{(N_x N_y N_z)} \end{aligned} \tag{4.30}$$

By using the information of submatrices in Table 4.2, the Schur complement matrix can be simplified further:

$$\frac{\partial \boldsymbol{r}_1}{\partial \Delta \bar{\boldsymbol{D}}} - \frac{\partial \boldsymbol{r_1}}{\partial \Delta \boldsymbol{\lambda}} \Big(\frac{\partial \boldsymbol{r_2}}{\partial \Delta \boldsymbol{\lambda}} \Big)^{-1} \frac{\partial \boldsymbol{r_2}}{\partial \Delta \bar{\boldsymbol{D}}} = \frac{\partial \boldsymbol{r}_1}{\partial \Delta \bar{\boldsymbol{D}}} + H \Big(\frac{\partial \boldsymbol{r_2}}{\partial \Delta \boldsymbol{\lambda}} \Big)^{-1} \tag{4.31}$$

At the same time, $\Delta(\Delta\boldsymbol{\lambda})$ reads as follows:

$$\Delta(\Delta\boldsymbol{\lambda}) = -\Big(\frac{\partial \boldsymbol{r_2}}{\partial \Delta\boldsymbol{\lambda}}\Big)^{-1}\Big(\boldsymbol{r}_2 + \frac{\partial \boldsymbol{r_2}}{\partial \Delta\bar{\boldsymbol{D}}}\Delta(\Delta\bar{\boldsymbol{D}})\Big) \tag{4.32}$$

4.3.3.6 The General Case of a Damage Evolution

In general, every grid point does not necessarily go through a process of damage evolution at the same time. For a grid point with index (i, j, k) going through elastic deformation, the condition $r_{2,(i,j,k)} = 0$ is not valid according to the KKT conditions. $\Delta(\Delta\lambda)$ should be zero at that grid point. As a consequence, the Jacobian matrix and the residual vector in equation (4.16) should be modified accordingly. When an elastic process takes place at a grid point, $\Delta(\Delta\lambda)$ can be expressed as follows:

$$\begin{aligned} \Delta(\Delta\lambda_{(i,j,k)}) &= 0 \\ \Longleftrightarrow 0\Delta(\Delta\bar{D}_{(i,j,k)}) + 1\Delta(\Delta\lambda_{(i,j,k)}) &= 0 \end{aligned} \tag{4.33}$$

In the previous section, when there is a damage evolution at a grid point, the following relation is derived from $r_{2,(i,j,k)} = 0$

$$\frac{\partial r_{2,(i,j,k)}}{\partial \Delta\bar{D}_{(i,j,k)}}\Delta(\Delta\bar{D}_{(i,j,k)}) + \frac{\partial r_{2,(i,j,k)}}{\partial \Delta\lambda_{(i,j,k)}}\Delta(\Delta\lambda_{(i,j,k)}) = -r_{2,(i,j,k)} \tag{4.34}$$

This equation should be replaced by equation (4.33). Equation (4.33) can be regarded as a special case of equation (4.34) where $\frac{\partial r_2}{\partial \Delta D} = 0$, $r_2 = 0$, and $\frac{\partial r_2}{\partial \Delta\lambda} = 0$. The value of $\frac{\partial r_1}{\partial \Delta\lambda}$ at a grid point where an elastic process takes place can be set to zero because $\Delta(\Delta\lambda)$ is zero there. The following Table 4.4 summarizes the terms to be replaced at grid points under elastic processes

Terms to be replaced	Values
$\frac{\partial r_{2,(i,j,k)}}{\partial \Delta\bar{D}_{2,(i,j,k)}}$	0
$\frac{\partial r_{2,(i,j,k)}}{\partial \Delta\lambda_{2,(i,j,k)}}$	1
$r_{2,(i,j,k)}$	0

TABLE 4.4: Modifications of terms when an elastic-loading takes place at a grid point, (i, j, k).

On the contrary, the micromorphic balance equation is always valid in a domain. Therefore, the residual vector of the micromorphic balance equation should be constructed in the same manner.

4.3.3.7 The Choice of an Iterative Solver

The choice of the iterative solver depends on the type of the Schur complement matrix $\left\{\frac{\partial \boldsymbol{r}_1}{\partial \Delta \bar{\boldsymbol{D}}} - \frac{\partial \boldsymbol{r}_1}{\partial \Delta \boldsymbol{\lambda}}\left(\frac{\partial \boldsymbol{r}_2}{\partial \Delta \boldsymbol{\lambda}}\right)^{-1}\frac{\partial \boldsymbol{r}_2}{\partial \Delta \bar{\boldsymbol{D}}}\right\}$. In order to analyze the Schur complement matrix further, the approximation of the submatrix $\left(\frac{\partial \boldsymbol{r_2}}{\partial \Delta \boldsymbol{\lambda}}\right)$ should be investigated. As the penalty term H is a huge value compared to other terms in equation (4.27), K_{nloc} is approximately $-H$ at every grid point. When every grid point goes through a damage loading process, this approximation makes the submatrix $\left(\frac{\partial \boldsymbol{r_2}}{\partial \Delta \boldsymbol{\lambda}}\right)$ to be close to a scalar matrix $-H\mathbf{I}$. Accordingly, the Schur complement matrix in equation (4.31) can be approximated as

$$\frac{\partial \boldsymbol{r}_1}{\partial \Delta \bar{\boldsymbol{D}}} - \frac{\partial \boldsymbol{r_1}}{\partial \Delta \boldsymbol{\lambda}}\left(\frac{\partial \boldsymbol{r_2}}{\partial \Delta \boldsymbol{\lambda}}\right)^{-1}\frac{\partial \boldsymbol{r_2}}{\partial \Delta \bar{\boldsymbol{D}}} \approx \frac{\partial \boldsymbol{r}_1}{\partial \Delta \bar{\boldsymbol{D}}} - \mathbf{I} \tag{4.35}$$

From Table 4.2, it is known that

$$\frac{\partial \boldsymbol{r}_1}{\partial \Delta \bar{\boldsymbol{D}}} \approx \mathbf{I} - \alpha \nabla^2 \tag{4.36}$$

By combining relations (4.35) and (4.36), the following approximation of the Schur complement matrix is valid when the penalty term H is huge enough:

$$\frac{\partial \boldsymbol{r}_1}{\partial \Delta \bar{\boldsymbol{D}}} - \frac{\partial \boldsymbol{r_1}}{\partial \Delta \boldsymbol{\lambda}}\left(\frac{\partial \boldsymbol{r_2}}{\partial \Delta \boldsymbol{\lambda}}\right)^{-1}\frac{\partial \boldsymbol{r_2}}{\partial \Delta \bar{\boldsymbol{D}}} \approx -\alpha \nabla^2 \tag{4.37}$$

As a result, equation (4.37) demonstrates that the Schur complement matrix is approximately a symmetric and positive-definite matrix when the penalty term H is large enough.
In the case of the second scenario of general damage loading, the Schur complement matrix is still symmetric and positive-definite. In a general case, considering the approximation in equation (4.27) and Table 4.4, $(\frac{\partial \boldsymbol{r_1}}{\partial \Delta \boldsymbol{\lambda}}(\frac{\partial \boldsymbol{r_2}}{\partial \Delta \boldsymbol{\lambda}})^{-1}\frac{\partial \boldsymbol{r_2}}{\partial \Delta \bar{\boldsymbol{D}}})$ will have a zero or one in the diagonal entries when H is large enough. Then, this matrix is semi-positive-definite so that the Schur complement matrix is still a symmetric and positive-definite matrix.
The symmetric and positive-definite nature of the Schur complement matrix makes it possible to solve the linear equation (4.16) by means of the conjugate gradient method. In the case of a symmetric and positive-definite matrix, the conjugate gradient method is much faster than GMRES (Generalized Minimal Residual Method). Therefore, the conjugate gradient method is used in the simultaneous scheme in the current work.

4.3.3.8 The Algorithm of Simultaneous Scheme

In summary, the algorithm of the simultaneous scheme is summarized below:

Algorithm 10 Simultaneous Scheme for Coupling Damage Fields

procedure SIMULTANEOUS SCHEME

Initialization: Take the initial guesses from values at a previous loading step $D_0^{n+1} = D^n$, $\xi_{d,0}^{n+1} = \xi_d^n$, and $\bar{D}_0^{n+1} = \bar{D}^n$. Initialize the initial increments with zero, $\Delta\bar{D}_0 = 0$ and $\Delta\lambda_0 = 0$

Calculate and save $\frac{\partial \boldsymbol{r_1}}{\partial \Delta \bar{\boldsymbol{D}}}$ using the central finite difference scheme (4.21).

Repeat:

(a) Loop over every grid point to calculate damage loading function ϕ_d.

if (ϕ_d > tolerance) **then**

Assign $\frac{\partial r_1}{\partial \Delta\lambda} = -1$, $\frac{\partial r_2}{\partial \Delta\bar{D}} = H$, $\frac{\partial r_2}{\partial \Delta\lambda} = K_{nloc}$, and $r_2 = \phi_d$.

else

Assign $\frac{\partial r_1}{\partial \Delta\lambda} = 0$, $\frac{\partial r_2}{\partial \Delta\bar{D}} = 0$, $\frac{\partial r_2}{\partial \Delta\lambda} = 1$, and $r_2 = 0$.

(b) Calculate $\boldsymbol{r_1}$ using equation (4.21).

(c) Check the convergence of the simultaneous scheme.

if (Coupling condition: ϕ_d < tolerance at every grid point) **then**

return .

else

(d) Calculate the Schur complement matrix in equation (4.31).

(e) Solve the Schur complement matrix for $\Delta(\Delta\bar{\boldsymbol{D}})_i$

(f) Update $\Delta\bar{D}_{i+1} = \Delta\bar{D}_i + \Delta(\Delta\bar{D})_i$.

(g) Update $\bar{D}_{i+1}^{n+1} = \bar{D}_0^{n+1} + \Delta\bar{D}_{i+1}$.

(h) Calculate $\Delta(\Delta\boldsymbol{\lambda})_i$ using equation (4.32).

(i) Update $\Delta\lambda_{i+1} = \Delta\lambda_i + \Delta(\Delta\lambda)_i$.

(j) Update $D_{i+1}^{n+1} = D_0^{n+1} + \Delta\lambda_{i+1}$ and $\xi_{d,(i+1)}^{n+1} = \xi_{d,0}^{n+1} + \Delta\lambda_{i+1}$.

(k) $i = i + 1$ and repeat the algorithm from step (a).

4.4 Validations of the Implementations of the Coupling Schemes

In general, deriving an analytical solution of a coupled problem is intricate or impossible because of nonlinearities in geometries of inclusions and material models. There is one way to test whether an implementation is correct. When it comes to a homogeneous RVE, the nonlocal damage model should show exactly the same behavior as that of the local damage model. The micromorphic balance equation (3.29) is reformulated for a homogeneous domain

$$\begin{aligned} \bar{D} - \alpha\nabla^2\bar{D} = D, \quad \alpha = \frac{A}{H} \\ \Leftrightarrow \bar{D} = D \end{aligned} \tag{4.38}$$

In the above equation, the Laplacian $\alpha\nabla^2\bar{D}$ taking account of the nonlocality of $\bar{D}$ disappears since every grid point will have the same field quantities in a homogeneous RVE. Therefore, the nonlocal damage variable should be the same as the local one. In the following sections, the mechanical boundary-value problem of a homogeneous RVE is solved using each coupling scheme, and the results are compared to the result of the local damage model. To make the validation simple, a virtual experiment of uniaxial stretch is performed in 2D space. The macroscopic deformation gradient $\mathbf{F}_0$ during the uniaxial stretch reads as follows:

$$\mathbf{F}_0 = \begin{pmatrix} l_i & 0 & 0 \\ 0 & 1/l_i & 0 \\ 0 & 0 & 1 \end{pmatrix} \quad l_i \in [1, l_f] \tag{4.39}$$

where l_i is the stretch in x-direction at i-th loading step, and l_f is the stretch at the final step. l_i is monotonously increasing from 1 to its final value l_f. The elastic and damage parameters in Table 4.5 are used. The penalty constant H is chosen as 10^4 MPa, and the internal length scale α is 10^{-6} MPa mm^2. The parameters are summarized as follows:

	Symbol	Value	Unit
Lamé's first parameter	Λ	5000	MPa
Lamé's second parameter	μ	7500	MPa
Initial damage threshold	Y_0	5	MPa
Damage parameter	r	50	MPa
Exponential damage parameter	s	0.5	-
Penalty constant	H	10^4	MPa
Internal length scale	α	10^{-6}	MPa mm^2

TABLE 4.5: Elastic-damage material parameters

The penalty constant H should be large enough to firmly couple the local and the nonlocal damage fields. In this case, the internal length scale α does not have any influence on a homogeneous RVE.

4.4.1 Comparison of the Results

The results of the local damage model and the nonlocal damage model are presented in this section. They are put on the same graph to prove that they show consistent results. The comparison is shown in Figure 4.3

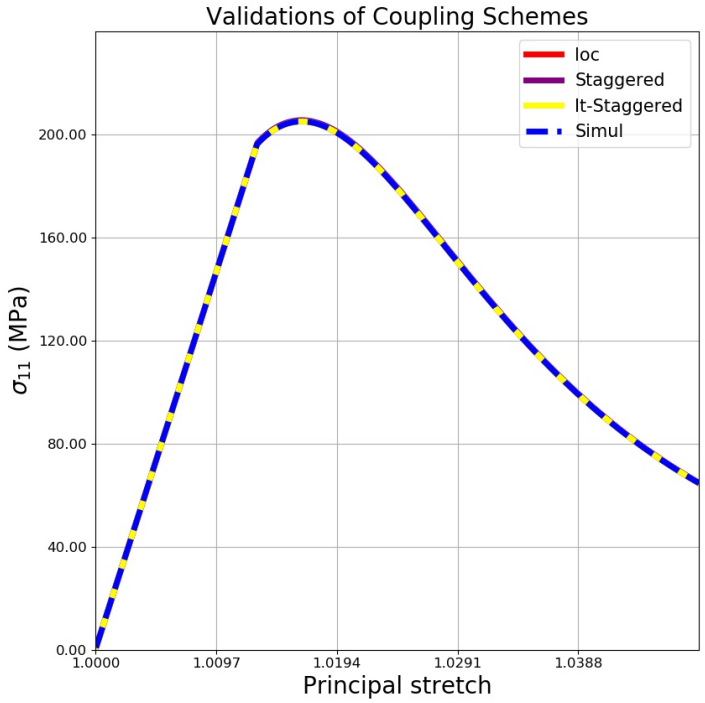

FIGURE 4.3: Comparison between the solution of the local damage model and that of the nonlocal damage model with different coupling schemes.

In Figure 4.3, only the results of the iteratively staggered scheme and the simultaneous one are visible. That is because results overlap each other. As a result, it is concluded that those schemes yield consistent results in the case of a homogeneous RVE.

Now, the runtime of each scheme matters from the practical point of view. The runtime of each scheme to get to the point of principal stretch being equal to 1.04855 is summarized in Table 4.6.

Numerical models	Local damage model	Nonlocal damage model		
		Staggered scheme	Iteratively staggered scheme	Simultaneous scheme
Time (s)	16	888	3395	18
Runtime ratio w.r.t. the local model	1.0	55.5	212.18	1.12

TABLE 4.6: The runtime of simulations with different schemes.

To compare the runtime clearly, the contents of Table 4.6 are visualized in the following Figure 4.4:

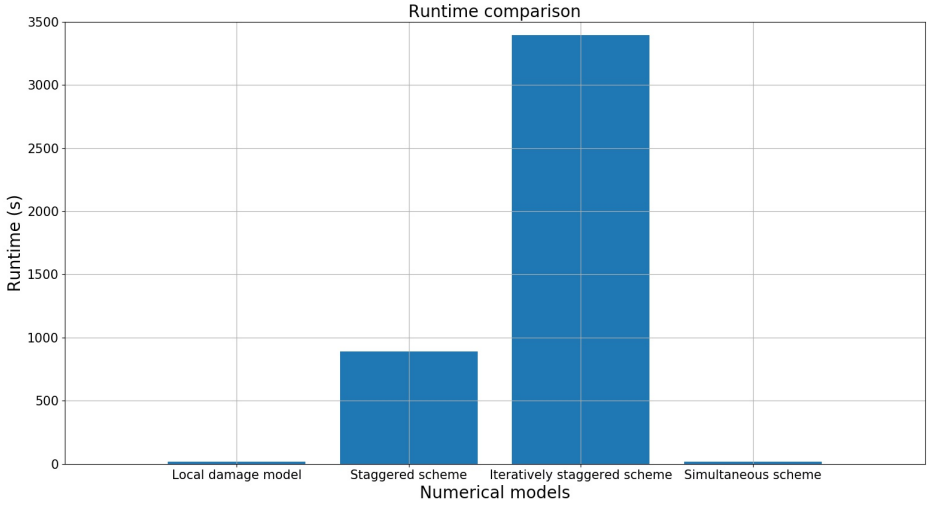

FIGURE 4.4: The iteratively staggered scheme takes up the largest amount of runtime. The simultaneous scheme is the fastest one among those coupling schemes.

In Table 4.6, the fastest coupling scheme is the simultaneous scheme which is 188.61 times faster than the iteratively staggered scheme. Moreover, the speed of the simultaneous scheme is comparable to that of the local damage model. In conclusion, as the simultaneous scheme is stable and the fastest one among those three coupling schemes, this scheme is adopted for running numerical examples in the following Chapter 5.

4.4.2 The Reason Why the Partitioned Approaches Are Slow

In previous section 4.1.2.1, the reason why a simultaneous scheme can be faster than a partitioned approach was described. However, this does not fully explain the reason why the partitioned approaches are much slower as shown in Figure 4.4.
The problem comes from the fact that $\bar{D}$ is not updated in the return-mapping algorithm 7 while D is updated. The cause of slow-down can be found from the return-mapping algorithm 7 for the partitioned approaches. An increment of the damage multiplier at each step in the return mapping algorithm reads as follows:

$$\Delta(\Delta\lambda) = \frac{\phi_{d,nloc}}{-K_{nloc}} = \frac{\phi_{d,loc} - H(D - \bar{D})}{-K_{loc} + H} \tag{4.40}$$

In order to make the expressions comparable to that of the local damage model, the damage loading function $\phi_{d,nloc}$ is expressed in terms of the local one $\phi_{d,loc}$. In the same manner, K_{nloc} is also expressed in terms of K_{loc} which is the corresponding term in the local damage model. By dividing the numerator and denominator in equation (4.40) by the penalty

constant H, the expression in equation (4.40) can be approximated as follows:

$$\Delta(\Delta\lambda) = \frac{\frac{1}{H}\phi_{d,nloc} - (D - \bar{D})}{\frac{-K_{loc}}{H} + 1} \approx \frac{-(D - \bar{D})}{1} << 1 \tag{4.41}$$

In the construction of the micromorphic approach, the penalty constant H ties D and $\bar{D}$ to become very close to each other, [4]. Consequently, $(D - \bar{D})$ will be an infinitesimal value in the equation (4.41). As an increment of $\Delta\lambda$ is infinitesimal in equation (4.41), each iteration in the return-mapping algorithm 7 results in an infinitesimal increment of D.
Even worse, an infinitesimal increment of D can make the damage loading function $\phi_{d,nloc}$ to be equal or less than zero, which lets the return-mapping algorithm 7 to converge without a sufficient increase in D. $\phi_{d,nloc}$ is highly affected by an infinitesimal increment of D because of the penalty term $-H(D - \bar{D})$ in $\phi_{d,nloc}$. While $\bar{D}$ is fixed in the return-mapping algorithm, an infinitesimal increment of D adds a large negative value to $\phi_{d,nloc}$. Thus, a huge value for H causes D to evolve less than it should. Returning a very small increment of D causes the overall iteratively staggered scheme 6 to run longer to yield a converged solution. It means that the FFT-based scheme and the spectral method for the micromorphic balance equation should run longer as well, which in turn leads to expensive FFT operations.

Chapter 5

Numerical Examples

In this chapter, parametric studies of the local damage model and applications of the local and the nonlocal damage models are presented. By investigating each parameter's influence on a damage evolution, proper choices can be made. On top of that, RVEs with a single and multiple inclusions are introduced to validate the local and the nonlocal damage model for general problems. Those damage models are used to simulate several damage loading scenarios on these RVEs.

5.1 Parametric Studies of the Local Damage Model

The influences of the damage parameter r and the exponential damage parameter s are investigated. It is obvious that the damage threshold Y_0 determines a loading step where an initial damage evolution takes place. For this reason, only the influences of r and s are investigated. Those three parameters are chosen, as follows:

	Symbol	Value
Initial damage threshold	Y_0	5 MPa
Damage parameter	r	50 MPa
Exponential damage parameter	s	0.5

TABLE 5.1: Elastic-damage material parameters

To begin with, the influence of an increase in r is investigated while Y_0 and s are fixed. Next, the influence of s is also investigated while the others are kept constant.

5.1.1 Effect of the damage parameter r

The influence of the damage parameter r is investigated. When only r varies, the comparison between different choices of r is shown in Figure 5.1

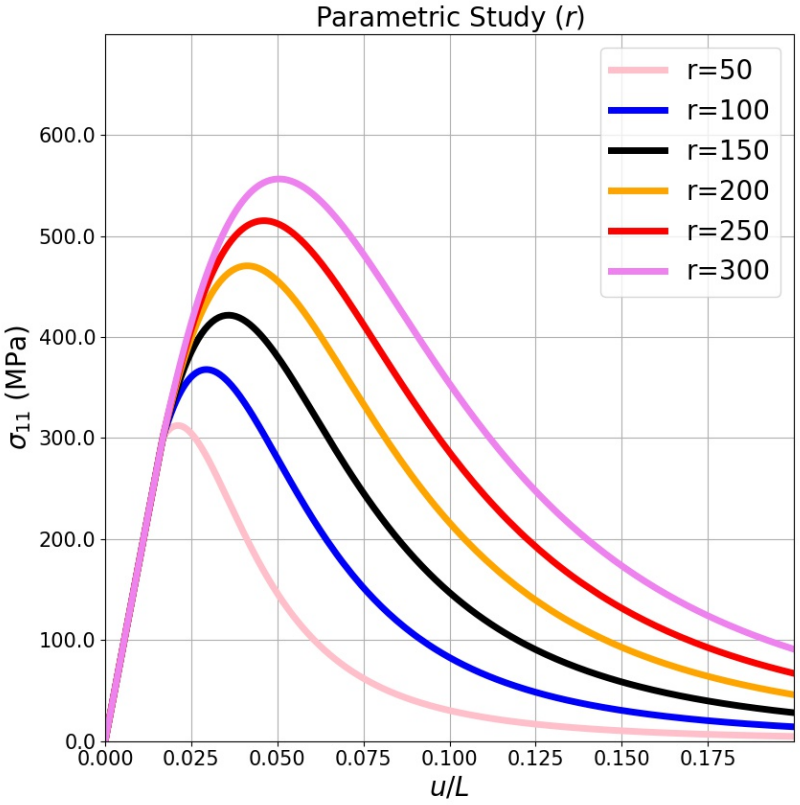

FIGURE 5.1: The influence of r on the effective material response at fixed Y_0 and s.

In Figure 5.1, as r increases, the curves of damage hardening/softening regions become higher and wider. Every curve has the same onset of the damage evolution since the same threshold Y_0 is used in every case. From Figure 5.1, it can be inferred that higher r makes a material to have slower damage evolution so that the maximum stress of its stress-strain curve becomes higher value. As a consequence, it is concluded that higher r makes a stress-strain curve to reach a higher peak and become wider.

5.1.2 Effect of the exponential damage parameter s

The case study of the influence of s is shown in Figure 5.2

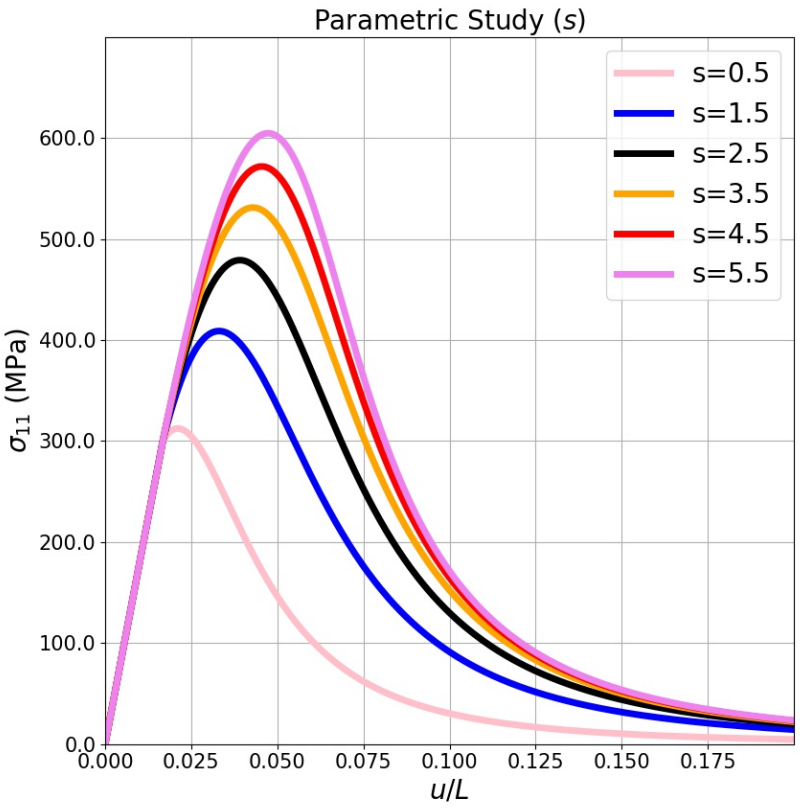

FIGURE 5.2: The influence of s while Y_0 and r are fixed.

As s increases, those graphs become higher as well. Apparently, increasing s seems to have the same effect of increasing r. Nevertheless, when s increases, the softening regions in Figure 5.2 do not become wider as much as the softening regions in Figure 5.1 do. In Figure 5.2, an increase in s not only increases a maximum stress but also makes a softening region to be steeper. In conclusion, by manipulating influences of those parameters r and s, one will have the flexibility of modeling a hardening/softening behavior of a material.

5.2 Problem of a Single Inclusion

In this section, the local and the nonlocal damage models are used to solve problems of a composite where its RVE has a single cylindrical inclusion at the center. The problem is defined as a plain-strain problem in 2D. The geometry of the composite's RVE is shown in Figure 5.3a and 5.3b

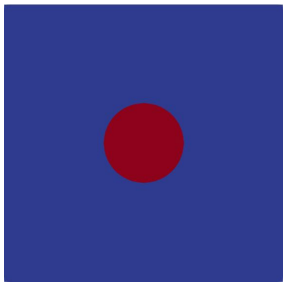

(A) An RVE having a cylindrical inclusion.

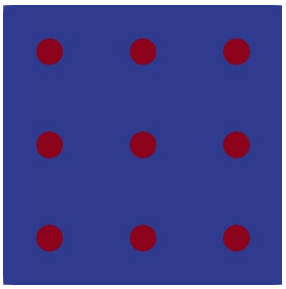

(B) Periodically distributed RVEs.

FIGURE 5.3: Visualizations of an RVE with a cylindrical inclusion.

The red color in Figure 5.3a and 5.3b represents the cylindrical inclusion, and blue matrix material is surrounding those inclusions. As the RVE is periodically distributed in a composite, the composite's microstructure will look like Figure 5.3b. The inclusion is presumed to be a purely elastic material as a inclusion is supposed to be much stiffer than a matrix material in most cases. The matrix material's elastic-damage behavior is described using the local damage model or the nonlocal one. The table of material parameters are summarized as follows:

	Symbol	Matrix	Inclusion
Lamé's first parameter	Λ	5000 MPa	5250 MPa
Lamé's second parameter	μ	7500 MPa	7875 MPa
Initial damage threshold	Y_0	5 MPa	∞
Damage parameter	r	50 MPa	-
Exponential damage parameter	s	0.5	-
Penalty term	H	10^4 MPa	-
Internal length scale	α	2.5×10^{-8} MPa mm^2	-

TABLE 5.2: Elastic-damage material parameters

In Table 5.2, the stiffness of the inclusion is 1.05 times as much as the stiffness of matrix. The material contrast ratio, 1.05, is set to be small for fast convergence of the FFT-based scheme. The virtual uniaxial stretch experiments are performed using the FFT-based scheme combined with those damage models. The macroscopic deformation gradient $\mathbf{F}_0$ at each loading step is defined as follows:

$$\mathbf{F}_0 = \begin{pmatrix} l_i & 0 & 0 \\ 0 & 1/l_i & 0 \\ 0 & 0 & 1 \end{pmatrix} \quad l_i \in [1, l_f] \tag{5.1}$$

where l_i is the principal stretch in x-direction at i-th loading step and monotonously increasing from 1 to l_f. l_f is the stretch at the final step.

5.2.1 Local Damage Model

In this section, the simulation results of the local damage model are presented. By using different discretizations, the grid convergence of those results is investigated. The comparison of simulations is presented in Figure 5.4

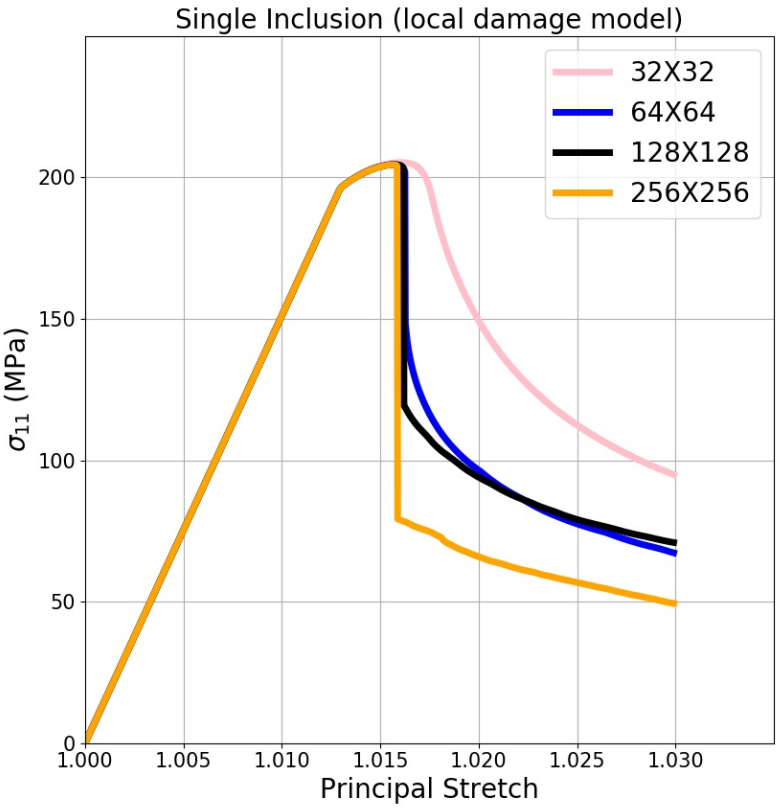

FIGURE 5.4: Simulations of the local damage model with different discretization.

In Figure 5.4, the number in each label indicates the level of discretization. For example, the pink curve in Figure 5.4 represents a grid having 32×32 grid points in two dimensional space. As it is shown in Figure 5.4, those curves in the figure have severe drop-down behaviors. The "snap-back" is possible to happen when a material goes through a process of strain localization, M. A. Crisfield [26]. As the principal stretch of the macroscopic deformation gradient $\mathbf{F}_0$ is always increasing, the loading condition in equation (5.1) cannot represent the phenomenon of snap-back. Consequently, at the drop-down points, the FFT-based had to calculate a solution while skipping a number of loading steps. The problem of the local damage model is that those points of drop-down do not converge towards a point. From the peak point, the localization of damage zone becomes severe so that fractured zones are generated in each RVE. Those graphs show individual softening behaviors after

the peak points. Even worse, they have totally different fractured profiles in Figure 5.5. In Figure 5.5, the results are arranged from the first quadrant to the fourth quadrant

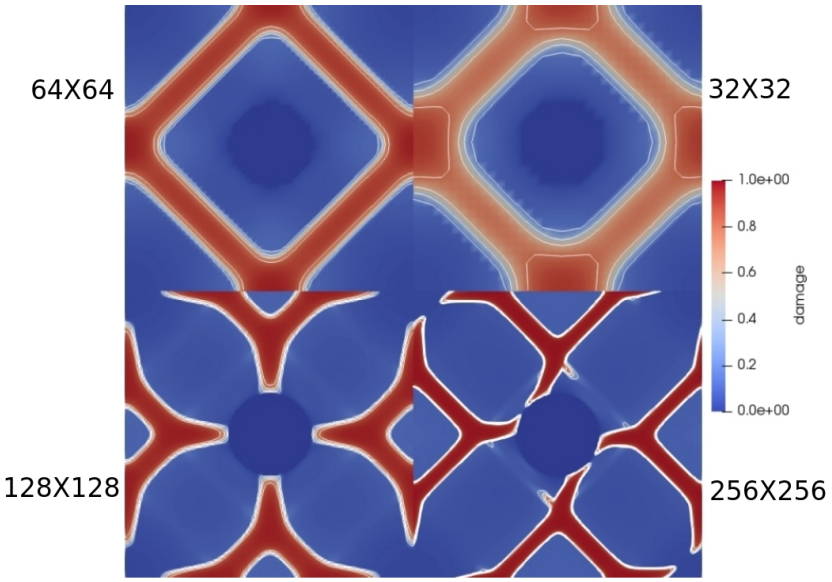

FIGURE 5.5: Fractured configurations of the local damage model. There are 32×32, 64×64, 128×128, and 256×256 grid points in each quadrant. The contour interval of the damage variable is 0.2.

Figure 5.5 shows that the spatial refinement does not lead to a convergence toward an unique solution. In conclusion, the local damage model does not have a converged solution in the softening region.

5.2.2 Nonlocal Damage Model

The defect of the local damage model that spatial refinement does not guarantee the existence of a unique solution motivates one to apply the nonlocal damage model. The results are displayed in Figure 5.6

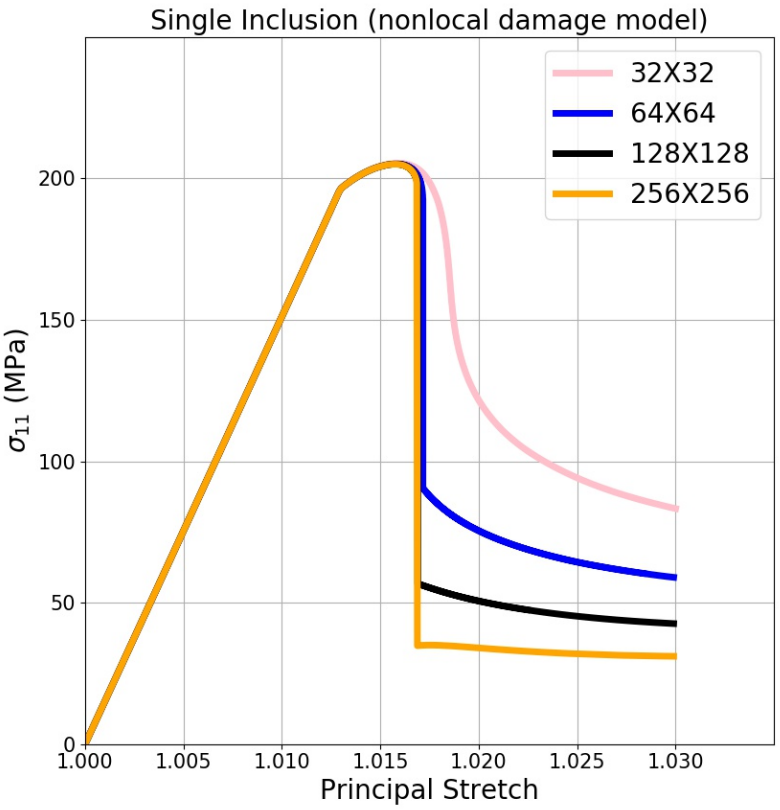

FIGURE 5.6: Simulations of the nonlocal damage model with different discretizations.

As it is shown in Figure 5.6, Those curves' points of drop-down converge toward one point $(1.01685, 198.314)$. However, simulations of the nonlocal damage model will show different softening-behavior depending on the level of discretization. For the construction of the simultaneous scheme, the Laplacian was approximated using the central finite-difference scheme, equation (4.20). Spatial resolution affects not only the FFT-based scheme but also the approximation of the Laplacian. This fact makes the diffusion of $\bar{D}$ to be dependent on a spatial resolution. For this reason, in Figure 5.6, the result of the coarsest grid shows the smoothest softening-behavior because the stencil of the central finite difference scheme, Figure 4.1, is the widest. Figure 5.7 backs up this investigation that the coarsest grid has the widest damage zone. As a consequence, the large damage zone in the coarsest grid could make strain localization to be less severe. On the other hand, finer ones show sharper transitions in softening regions. Nevertheless, in the case of the nonlocal damage model, it is promising that spatial refinement leads to closer softening regions in Figure 5.6.
Moreover, it is also promising that the fractured configurations of RVEs shown in Figure 5.7 have consistent fractures

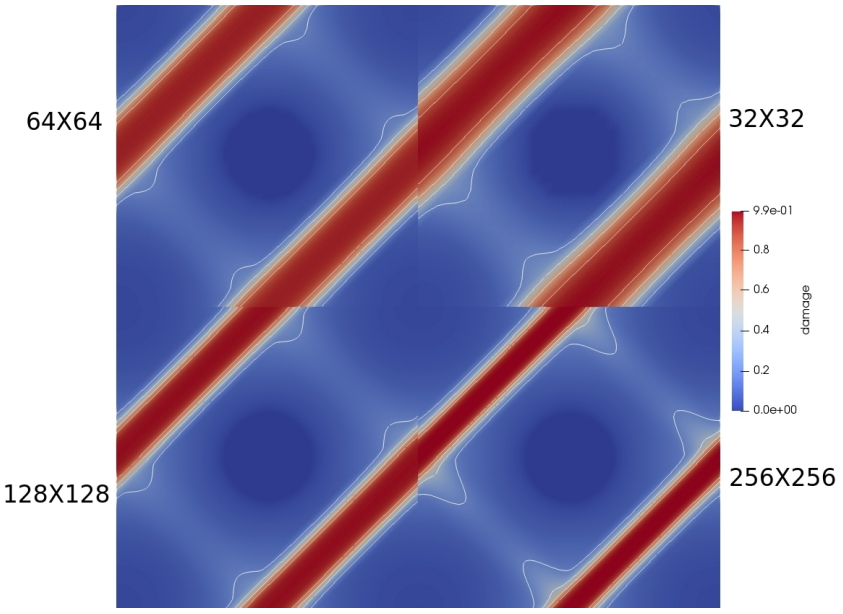

FIGURE 5.7: Fractured configurations of the nonlocal damage model. There are 32×32, 64×64, 128×128, and 256×256 grid points in each quadrant. The contour interval of damage variable is 0.2.

This is a good indication that the nonlocal damage model results in consistent results when the spatial discretization becomes finer. Figure 5.7 also supports the fact that the approximation of the Laplacian on a coarser grid results in more diffusive damage field.

5.3 Problem of Multiple Inclusions

In this section, an RVE consists of randomly distributed multiple inclusions is investigated. The RVEs containing multiple inclusions are visualized in Figure 5.8a and 5.8b

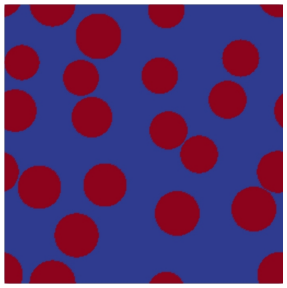

(A) An RVE having multiple cylindrical inclusions.

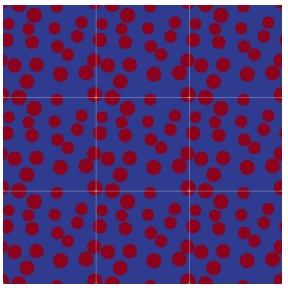

(B) Periodically distributed RVEs.

FIGURE 5.8: Visualizations of RVEs with multiple cylindrical inclusions.

In Figure 5.8b, it is shown that the RVE satisfies the geometric continuity across the boundaries. The RVE in Figure 5.8a is used to conduct virtual experiments of uniaxial stretches

in x and y directions and a shear deformation. The virtual experiments are conducted using the local and the nonlocal damage models to be compared to each other.

5.3.1 Uniaxial Stretch in X-Direction

Uniaxial stretch simulations are performed on the RVEs with different spatial discretizations. In this case, the macroscopic deformation gradient at each loading step is defined as it is for the single inclusion simulations, (5.1). First, the effective stress-principal stretch curves of grids are compared to investigate a grid convergence. Next, the fractured configurations at principal stretch 1.02 are compared to investigate the consistency in the fractured shapes.

5.3.1.1 Stress Curves

The stress-principal stretch curves of the local and the nonlocal damage models are shown in Figures 5.9a and 5.9b respectively

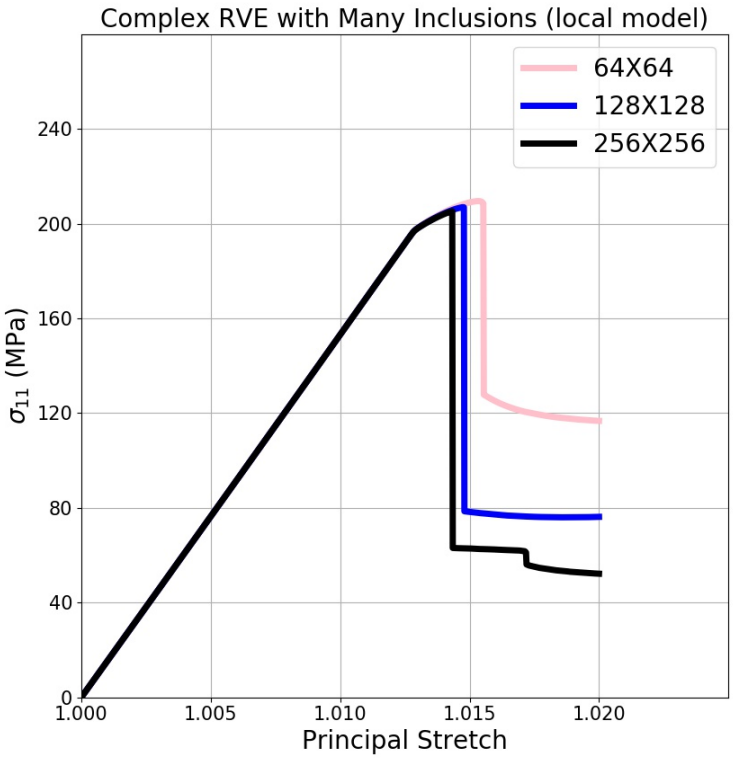

(A) The local damage model.

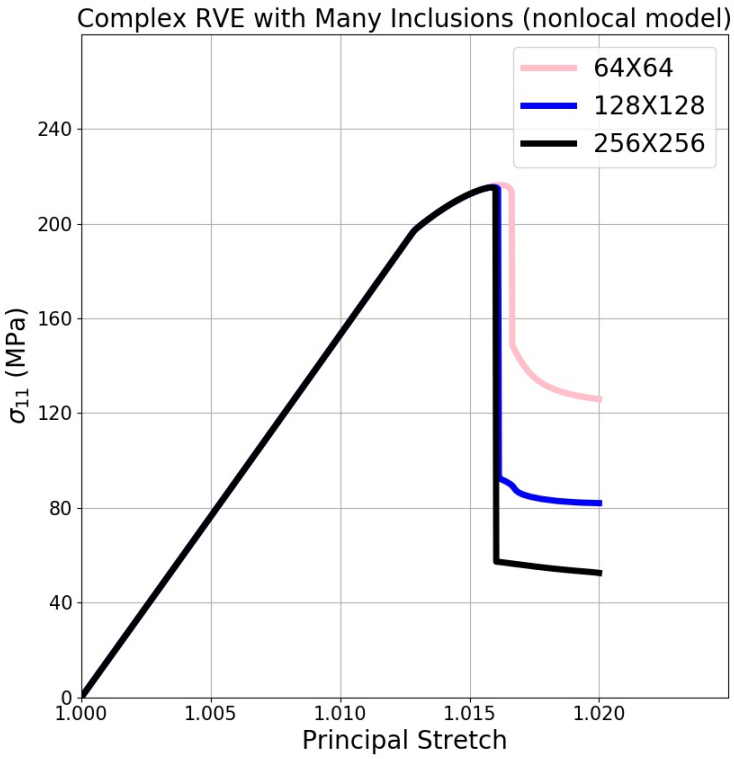

(B) The nonlocal damage model.

FIGURE 5.9: The effective response of the damage models under the uniaxial stretch in x-direction.

In Figure 5.9a, the spatial refinement for the local damage model does not lead to a converged solution. Specifically, those three curves' drop-down points differ from each other. As a result, it is hard to predict the loading step where a composite breaks down using the local damage model.
On the other hand, the drop-down points in Figure 5.9b converges toward the point $(1.016, 214.431)$. Still, curves in Figure 5.9b show individual profiles depending on the level of spatial discretizations.

5.3.1.2 Fractured Configurations

The fractured configurations of the local and the nonlocal damage models are shown in Figures 5.10a and 5.10b respectively. In Figure 5.10a, the results of the local damage model show inconsistent fractured configurations. The result of the finest grid is different from the others. On the other hand, the fractures of the nonlocal damage model are consistent. Fractured regions of different grids match each other at boundaries in Figure 5.10b. In conclusion, the nonlocal damage model yields the consistent fractures while the local one does not.

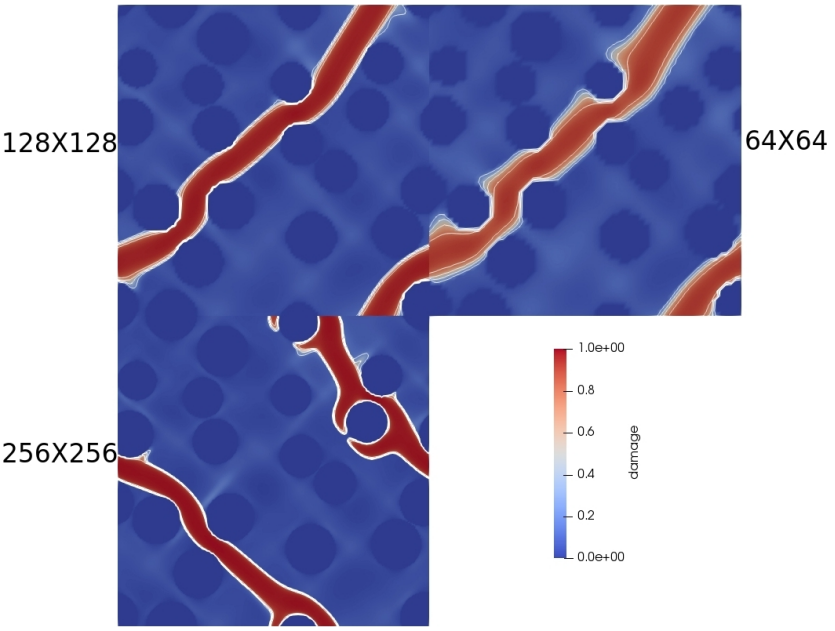

(A) The result of the local damage model under an uniaxial stretch in x-direction.

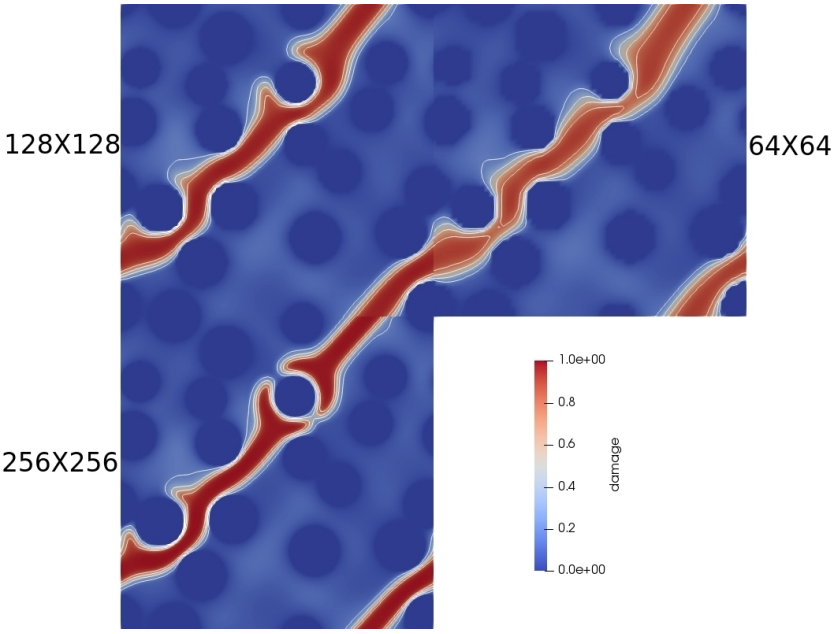

(B) The result of the nonlocal damage model under an uniaxial stretch in x-direction.

FIGURE 5.10: There are 64×64, 128×128, and 256×256 points in each quadrant. The principal stretch is 1.02. The contour interval of the damage variable is 0.2.

5.3.2 Uniaxial Stretch in Y-Direction

The macroscopic deformation gradient for the simulations in y-direction is given by:

$$\mathbf{F}_0 = \begin{pmatrix} 1/l_i & 0 & 0 \\ 0 & l_i & 0 \\ 0 & 0 & 1 \end{pmatrix} \quad l_i \in [1, l_f] \tag{5.2}$$

where l_i is the principal stretch in y-direction at i-th loading step and monotonously increasing from 1 to l_f. l_f is the principal stretch at the final loading step. Likewise, the local and the nonlocal damage models are used to simulate this loading condition 5.2.

5.3.2.1 Stress Curves

The effective responses of the local and the nonlocal damage models are described in Figure 5.11a and 5.11b respectively.

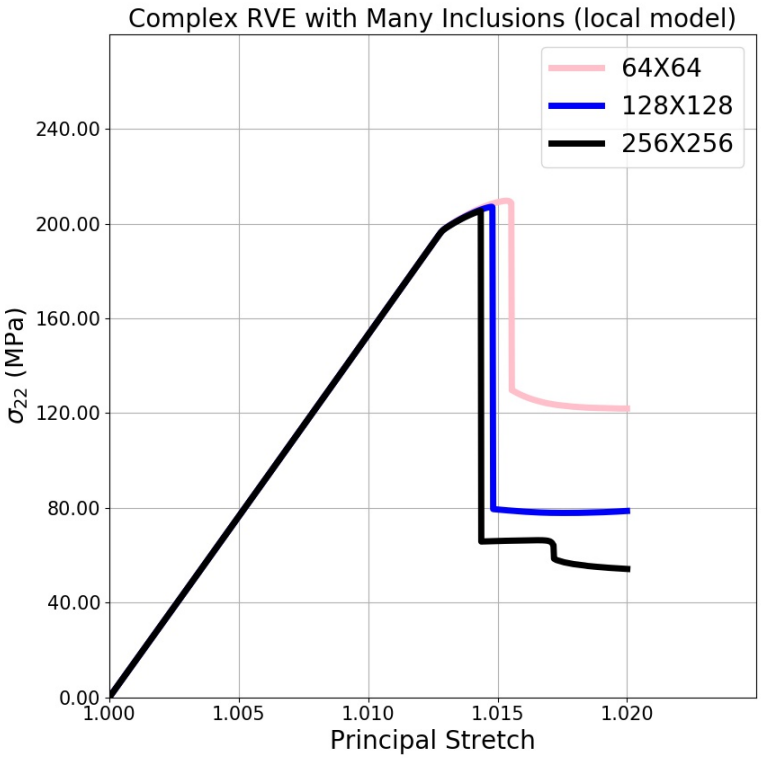

(A) The local damage model.

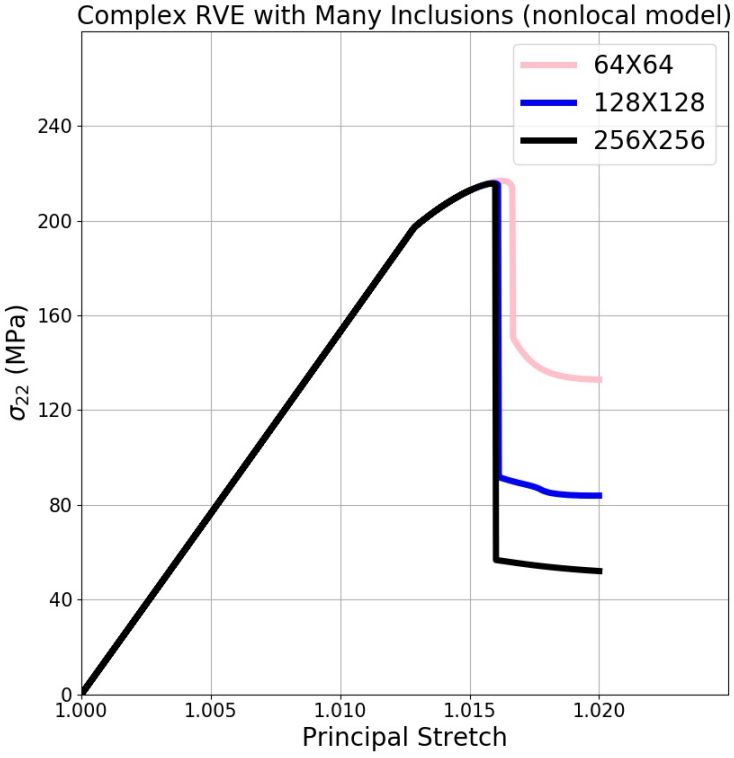

(B) The nonlocal damage model.

FIGURE 5.11: The effective response of the damage models under the uniaxial stretch in y-direction.

The effective responses under the stretch in y-direction are very similar to those in x-direction, Figures 5.9a and 5.9b. The similarity implies that the RVE 5.8a has an isotropic effective response. This can happen because the RVE is made of randomly distributed circular inclusions. Also, the isotropic Neo-Hooken solid model is used for both the matrix material and the inclusions. According to I. M. Gitman et al. [27], an RVE does not necessarily have to be uniquely defined for an arbitrary heterogeneous microstructure. If the RVE in Figure 5.8a is rotated 90 degrees clockwise, the rotated RVE still has similar statistical properties. First, the rotated one has the same amount of density of the inclusions. Second, since those inclusions are randomly distributed, the rotated one has the similar standard variation in the distribution of those inclusions. As a consequence, the rotated one is eligible to be an RVE of the microstructure as well, Figure 5.8b. Therefore, this inference leads to the conclusion that the effective response of the RVE is isotropic.

5.3.2.2 Fractured Configurations

The fractured configurations of the local and the nonlocal damage models are shown in Figures 5.12a and 5.12b respectively.

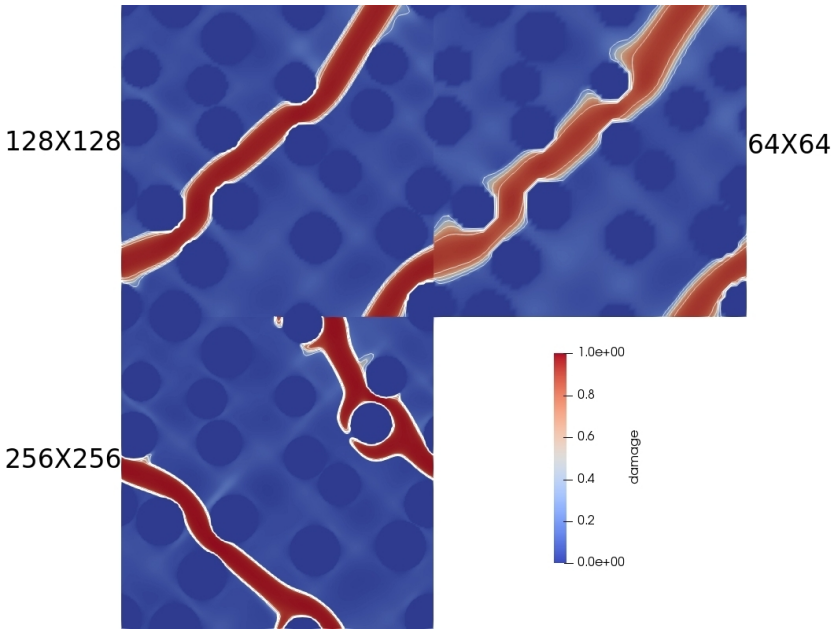

(A) The result of the local damage model under an uniaxial stretch in y-direction.

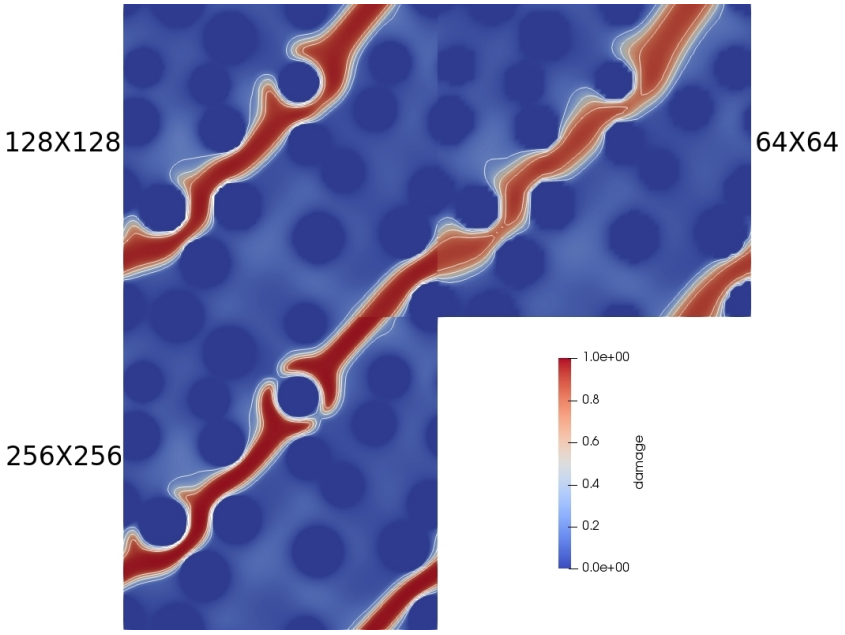

(B) The result of the nonlocal damage model under an uniaxial stretch in y-direction.

FIGURE 5.12: There are 64×64, 128×128, and 256×256 points in each quadrant. The principal stretch is 1.02. The contour interval of the damage variable is 0.2.

As it is discussed in previous section 5.3.2.1, because of the isotropic response, the fractured configurations of the local and the nonlocal damage models are almost same to those under the loading in the x-direction.

5.3.3 Shear Deformation

The macroscopic deformation gradient under a shear deformation is defined in the following manner:

$$\mathbf{F}_0 = \begin{pmatrix} 1 & l_i & 0 \\ l_i & 1 & 0 \\ 0 & 0 & 1 \end{pmatrix} \quad l_i \in [1, l_f] \tag{5.3}$$

where l_i is the amount of shear deformation at i-th loading step and monotonously increasing from 1 to l_f. When l_i is small enough, $\mathbf{F}_0$ becomes the deformation gradient of a pure shear problem. The macroscopic small strain tensor $\boldsymbol{\epsilon}_0$ can be expressed in terms of $\mathbf{F}_0$ in the following manner:

$$\boldsymbol{\epsilon}_0 = \frac{1}{2}(\mathbf{F}_0 + \mathbf{F}_0^T) - \mathbf{I} \tag{5.4}$$

When $\mathbf{F}_0$ is given as equation (5.3), $\boldsymbol{\epsilon}_0$ reads as follows:

$$\boldsymbol{\epsilon}_0 = \begin{pmatrix} 0 & l_i & 0 \\ l_i & 0 & 0 \\ 0 & 0 & 0 \end{pmatrix} \quad l_i \in [1, l_f] \tag{5.5}$$

When l_i is small enough, $\mathbf{F}_0$ in equation (5.3) becomes the deformation gradient of a pure shear deformation. Finally, the results of the local and the nonlocal damage models are introduced in the following sections.

5.3.3.1 Stress Curves

The effective responses of the microstructure under the shear deformation are calculated using the local and the nonlocal damage models. These responses are described in Figures 5.13a and 5.13b

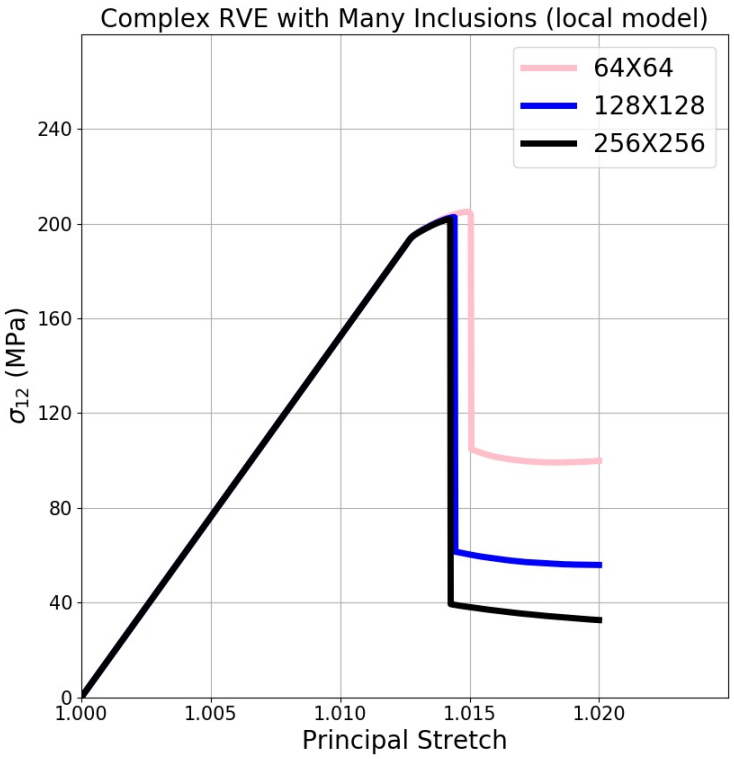

(A) The local damage model.

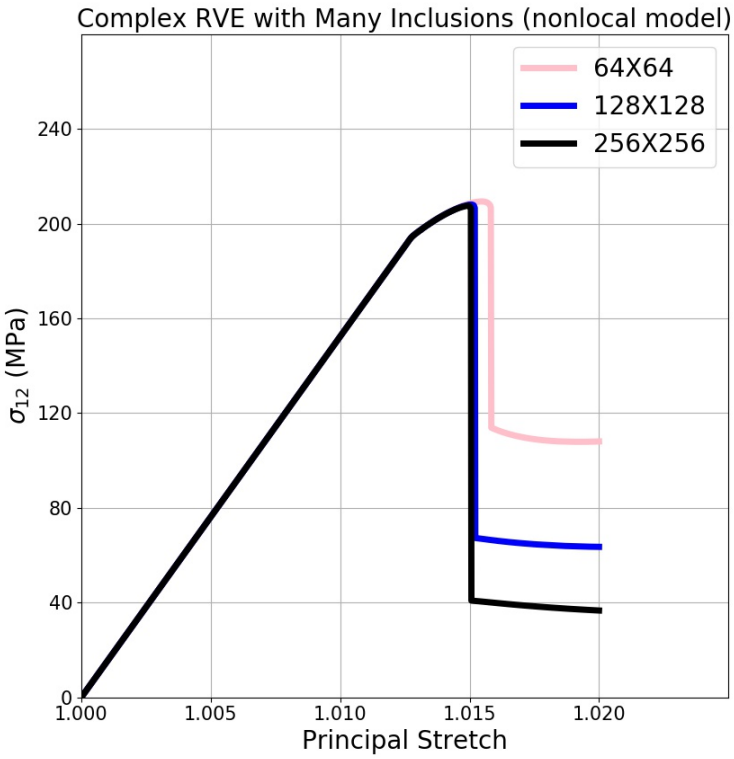

(B) The nonlocal damage model.

FIGURE 5.13: The effective response of the damage models under the shear deformation.

Those two graphs of the local and the nonlocal damage models look very similar to each other. This similarity can be explained by examining the fractured configurations.

5.3.3.2 Fractured Configurations

The fractured configurations are shown in Figures 5.12a and 5.14b respectively. Both figures have vertical fractures. In this case, the local damage model shows consistent fractured configurations. In the previous case studies on the RVE with a single inclusion, the fractured configurations generated from the local damage model are individual in Figure 5.5. That is because there are multiple possibilities of fractures to be generated in the matrix. However, certain weak regions in an RVE can be determined from its microstructure and a loading condition. Considering the microstructure of the RVE, it is obvious that fractures will be generated in the matrix located between inclusions because inclusions are purely elastic. Since weak regions are obvious in the RVE, the problem of the local damage model may be well-posed on the RVE under the shear deformation. Therefore, the local and the nonlocal damage models yield similar the consistent results in this special case

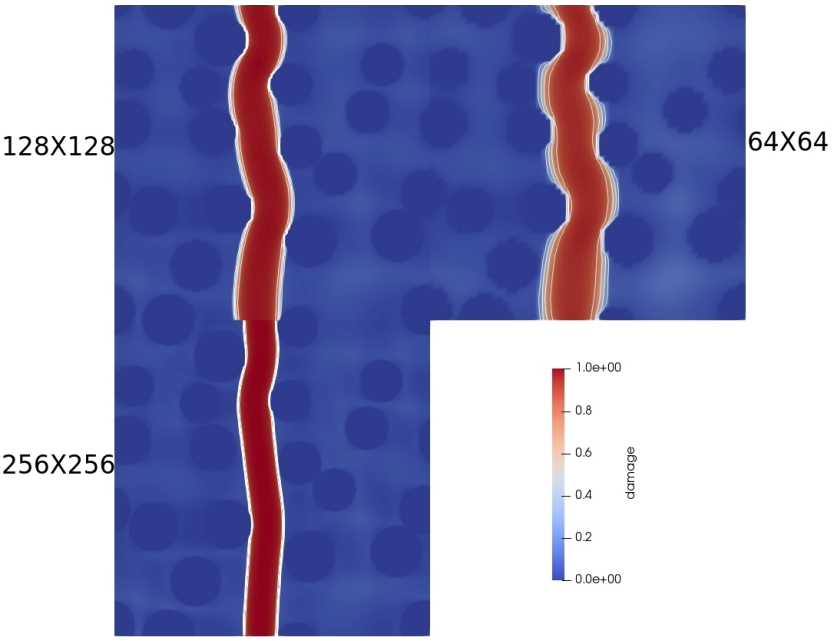

(A) The result of the local damage model under a shear deformation.

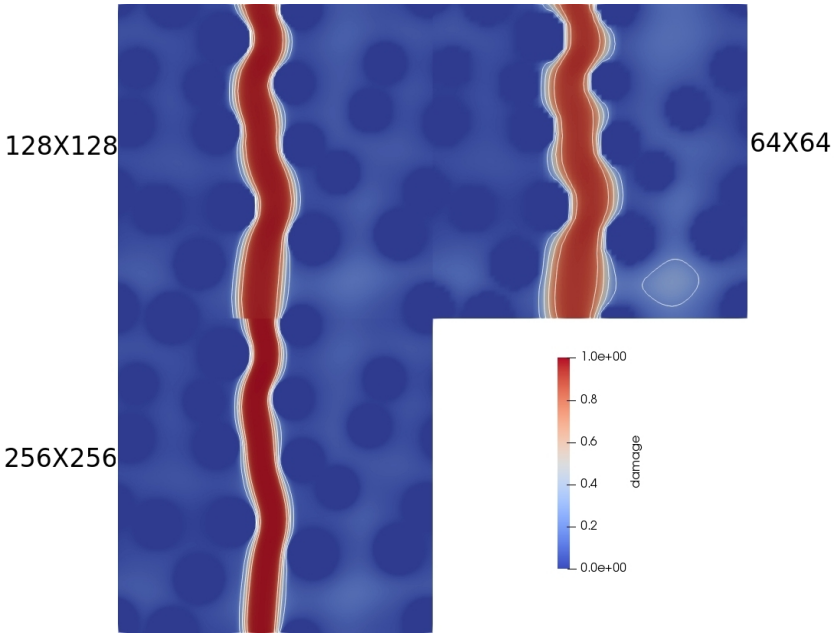

(B) The result of the nonlocal damage model under a shear deformation.

FIGURE 5.14: There are 64×64, 128×128, and 256×256 points in each quadrant. The principal stretch is 1.02. The contour interval of the damage variable is 0.2.

Chapter 6

Conclusions

6.1 Summary of Major Investigations

In summary, the implementation of the gradient-extended damage model in the FFT-based scheme and its numerical examples are investigated in this thesis. In conclusion, the nonlocal damage model (3.29) implemented using the simultaneous scheme's algorithm 10, is recommended to replace the local damage model. One reason is that the nonlocal damage model shows the grid convergence until a severe strain localization takes place. Furthermore, the nonlocal damage model yields consistent fractured configurations for different spatial discretizations. The investigations and remarks in this paper are summarized as follows:

- According to Figures 4.3 and 4.4 in Chapter 4, it is shown that the simultaneous scheme is stable and the fastest coupling scheme for the current research.
- The RVE having cylindrical inclusions, Figure 5.8a, shows almost isotropic effective behavior. That is because those inclusions are circular in 2D and randomly distributed. If the inclusions are other geometric objects like a triangle or elliptic curves, the effective response of an RVE might be anisotropic.
- The local damage model shows non-unique fractured configurations in the softening regions depending on the level of spatial discretizations, shown in Figures 5.5, 5.10a, and 5.12a. Nevertheless, it does not necessarily mean that the local damage model always fails to have a unique solution. Depending on a combination of the geometry of an RVE and loading conditions, the problem of the local damage model in softening regions can be well-posed in certain cases, shown in Figure 5.14a.
- The nonlocal damage model has shown consistent fractured configurations in every case study, Figures 5.7, 5.10a, 5.12a, and 5.14a.

- When it comes to hardening or softening regions, both damage models show drop-down phenomena of effective behaviors. For example, Figures 5.9a and 5.9b.

The following topics are suggested to develop more robust and realistic simulations in the future.

- For ductile simulations, plasticity models can be also taken into account since plasticity and damage evolution are likely to take place at the same time.
- The Newton-Raphson based methods can be more stable and accelerate the speed of computations by means of the quadratic convergence, M. Kabel [3]. It can be used to run simulations with higher spatial resolution or 3D problems.
- In order to heal the drop-down phenomena possibly arising from the snap-back problems, artificial-viscosity can be applied.
- The gradient-extended damage model with the micromorphic approach can be also implemented in an FEA software. The concept of the homogenization technique can be applied in an FEA software. In each loading step, the periodic boundary condition and a macroscopic deformation gradient can be used to define boundary conditions in FEA. For structural inclusions, the spatial discretization using finite elements can represent a geometry of an inclusion neatly. FEA can be more stable and efficient platform than the FFT-based scheme in that case.

Appendix A

The Sparse Matrix Format

In order to reduce hardware memory occupancy for expressing a huge size matrix, sparse matrix formats are devised to express only nonzero entries in a matrix. The Compressed Sparse Row (CSR) and Compressed Sparse Column (CSC) formats are widely used. Those sparse matrix formats are very useful when an iterative solver is used to solve a linear equation. In that case, a matrix does not need to be directly inverted, but only matrix-vector multiplications are necessary to solve a linear problem. In C/C++, a multidimensional array is represented in a row-major format. On the other hand, in Fortran, that is done in a column-major format. To keep the consistency with the standard data storage format in C/C++, the CSR format is employed. This consistency is advantageous when a matrix in a dense form is converted into the CSR format since it is possible to utilize cache-hit. On top of that, each row of the approximation of the Laplacian using the central finite difference scheme (4.20) is calculated sequentially, it is easier to construct the approximation (4.20) in the CSR format. From the development reference for Intel Math Kernel Library 2018 - Fortran (Beta) [28], descriptions and an example of the CSR format can be found. It is supposed that a matrix has m rows, n columns, and nnz nonzero entries. The arrays in terms of the nonzero values, row, and column positions of a matrix are described in the following Table:

values	This array contains every nonzero values in a matrix. In the CSR format, nonzero values are saved in this array in the row-major sequence. The size of the array is equal to the number of nonzero values nnz.
columns	Column indexes of nonzero values are stored in this array. The size of the array is equal to the number of nonzero values nnz.
rowIndex	Locations of first elements in each row are saved in this array. Basically, this array has size of m. On top of that, the last entry of this array saves $(nnz + 1)$. As a result, this array has size of $(m + 1)$.

For an instance, a matrix in the dense format is given as an example

$$\mathbf{B} = \begin{pmatrix} -1 & 1 & * & -3 & * \\ -2 & 5 & * & * & * \\ * & * & 4 & 6 & 4 \\ -4 & * & 2 & 7 & * \\ * & 8 & * & * & -5 \end{pmatrix} \tag{A.1}$$

The matrix B can be represented in the CSR format in the following manner in Table A.1:

Storage arrays for a Matrix in the CSR Format														
one-based indexing														
Values	=	(-1	1	-3	-2	5	4	6	4	-4	2	7	8	-5)
Columns	=	(1	2	4	1	2	3	4	5	1	3	4	2	5)
RowIndex	=	(1	4	6	9	12	14)							
zero-based indexing														
Values	=	(-1	1	-3	-2	5	4	6	4	-4	2	7	8	-5)
Columns	=	(0	1	3	0	1	2	3	4	0	2	3	1	4)
RowIndex	=	(0	3	5	8	11	13)							

TABLE A.1: The representation of the matrix B in the CSR format.

Bibliography

[1] H. Moulinec and P. Suquet. A numerical method for computing the overall response of nonlinear composites with complex microstructure. *Computer Methods in Applied Mechanics and Engineering*, 157(1):69 – 94, 1998. ISSN 0045-7825. doi: https://doi.org/10.1016/S0045-7825(97)00218-1. URL http://www.sciencedirect.com/science/article/pii/S0045782597002181.

[2] P. Eisenlohr, M. Diehl, R.A. Lebensohn, and F. Roters. A spectral method solution to crystal elasto-viscoplasticity at finite strains. *International Journal of Plasticity*, 46:37 – 53, 2013. ISSN 0749-6419. doi: https://doi.org/10.1016/j.ijplas.2012.09.012. URL http://www.sciencedirect.com/science/article/pii/S0749641912001428. Microstructure-based Models of Plastic Deformation.

[3] Matthias Kabel, Thomas Böhlke, and Matti Schneider. Efficient fixed point and newton–krylov solvers for fft-based homogenization of elasticity at large deformations. *Computational Mechanics*, 54(6):1497–1514, Dec 2014. ISSN 1432-0924. doi: 10.1007/s00466-014-1071-8. URL https://doi.org/10.1007/s00466-014-1071-8.

[4] Samuel Forest. Micromorphic approach for gradient elasticity, viscoplasticity, and damage. *Journal of Engineering Mechanics*, 135(3):117–131, 2009. doi: 10.1061/(ASCE)0733-9399(2009)135:3(117). URL http://ascelibrary.org/doi/abs/10.1061/.

[5] Tim Brepols, Stephan Wulfinghoff, and Stefanie Reese. Gradient-extended two-surface damage-plasticity: Micromorphic formulation and numerical aspects. *International Journal of Plasticity*, 97(Supplement C):64 – 106, 2017. ISSN 0749-6419. doi: https://doi.org/10.1016/j.ijplas.2017.05.010. URL http://www.sciencedirect.com/science/article/pii/S0749641916303461.

[6] The determination of the elastic field of an ellipsoidal inclusion, and related problems. *Proceedings of the Royal Society of London A: Mathematical, Physical and Engineering Sciences*, 241(1226):376–396, 1957. ISSN 0080-4630. doi: 10.1098/rspa.1957.0133. URL http://rspa.royalsocietypublishing.org/content/241/1226/376.

[7] P. H. Dederichs and R. Zeller. Variational treatment of the elastic constants of disordered materials. *Zeitschrift für Physik A Hadrons and nuclei*, 259(2):103–116, Apr 1973. ISSN 0939-7922. doi: 10.1007/BF01392841. URL https://doi.org/10.1007/BF01392841.

[8] Johannes Spahn. *An Efficient Multiscale Method for Modeling Progressive Damage in Composite Materials*. PhD thesis, 2015. URL http://nbn-resolving.de/urn/resolver.pl?urn:nbn:de:hbz:386-kluedo-39800.

[9] B. A. Lippmann and Julian Schwinger. Variational principles for scattering processes. i. *Phys. Rev.*, 79:469–480, Aug 1950. doi: 10.1103/PhysRev.79.469. URL https://link.aps.org/doi/10.1103/PhysRev.79.469.

[10] M. Frigo and S. G. Johnson. The design and implementation of fftw3. *Proceedings of the IEEE*, 93(2):216–231, Feb 2005. ISSN 0018-9219. doi: 10.1109/JPROC.2004.840301.

[11] A. Vidyasagar, W.L. Tan, and D.M. Kochmann. Predicting the effective response of bulk polycrystalline ferroelectric ceramics via improved spectral phase field methods. *Journal of the Mechanics and Physics of Solids*, 106(Supplement C):133 – 151, 2017. ISSN 0022-5096. doi: https://doi.org/10.1016/j.jmps.2017.05.017. URL http://www.sciencedirect.com/science/article/pii/S0022509617300595.

[12] W. H. Müller. Fourier transforms and their application to the formation of textures and changes of morphology in solids. In Yehia A. Bahei-El-Din and George J. Dvorak, editors, *IUTAM Symposium on Transformation Problems in Composite and Active Materials*, pages 61–72, Dordrecht, 2002. Springer Netherlands. ISBN 978-0-306-46935-0.

[13] J.C. Simo and J.W. Ju. Strain- and stress-based continuum damage models—i. formulation. *International Journal of Solids and Structures*, 23(7):821 – 840, 1987. ISSN 0020-7683. doi: https://doi.org/10.1016/0020-7683(87)90083-7. URL http://www.sciencedirect.com/science/article/pii/0020768387900837.

[14] Raymond P. Canale Steven C. Chapra. *Numerical Methods for Engineers*, pages 147–151. Mc Graw Hill, 2010. ISBN 978–0–07–340106–5.

[15] Zdeněk P. Bažant, Ted B. Belytschko, and Ta-Peng Chang. Continuum theory for strain-softening. *Journal of Engineering Mechanics*, 110(12):1666–1692, 1984. doi: 10.1061/(ASCE)0733-9399(1984)110:12(1666). URL https://ascelibrary.org/doi/abs/10.1061/%28ASCE%290733-9399%281984%29110%3A12%281666%29.

[16] N. Triantafyllidis and Elias C. Aifantis. A gradient approach to localization of deformation. i. hyperelastic materials. *Journal of Elasticity*, 16(3):225–237, Sep 1986.

ISSN 1573-2681. doi: 10.1007/BF00040814. URL https://doi.org/10.1007/BF00040814.

[17] H. L. Schreyer and Z. Chen. One-dimensional softening with localization. *Journal of Applied Mechanics*, 53:791–797, Dec 1986.

[18] David Lasry and Ted Belytschko. Localization limiters in transient problems. *International Journal of Solids and Structures*, 24(6):581 – 597, 1988. ISSN 0020-7683. doi: https://doi.org/10.1016/0020-7683(88)90059-5. URL http://www.sciencedirect.com/science/article/pii/0020768388900595.

[19] R. H. J. PEERLINGS, R. DE BORST, W. A. M. BREKELMANS, and J. H. P. DE VREE. Gradient enhanced damage for quasi-brittle materials. *International Journal for Numerical Methods in Engineering*, 39(19):3391–3403, 1996. ISSN 1097-0207. doi: 10.1002/(SICI)1097-0207(19961015)39:19<3391::AID-NME7>3.0.CO;2-D. URL http://dx.doi.org/10.1002/(SICI)1097-0207(19961015)39:19<3391::AID-NME7>3.0.CO;2-D.

[20] Mikhail Itskov. *Tensor Algebra and Tensor Analysis for Engineers*, pages 51–53. Springer-Verlag Berlin Heidelberg, 2007. ISBN 978-3-540-36047-6. doi: 10.1007/978-3-540-36047-6.

[21] Carlos A. Felippa, K.C. Park, and Charbel Farhat. Partitioned analysis of coupled mechanical systems. *Computer Methods in Applied Mechanics and Engineering*, 190(24–25):3247 – 3270, 2001. ISSN 0045-7825. doi: https://doi.org/10.1016/S0045-7825(00)00391-1. URL https://www.sciencedirect.com/science/article/pii/S0045782500003911. Advances in Computational Methods for Fluid-Structure Interaction.

[22] *The artificial added mass effect in sequential staggered fluid-structure interaction algorithms*, 2006. Delft University of Technology. ISBN 90-9020970-0.

[23] K. Hameyer, J. Driesen, H. De Gersem, and R. Belmans. The classification of coupled field problems. *IEEE Transactions on Magnetics*, 35(3):1618–1621, May 1999. ISSN 0018-9464. doi: 10.1109/20.767304.

[24] Martin Boeff, Florian Gutknecht, Philipp S. Engels, Anxin Ma, and Alexander Hartmaier. Formulation of nonlocal damage models based on spectral methods for application to complex microstructures. *Engineering Fracture Mechanics*, 147:373 – 387, 2015. ISSN 0013-7944. doi: https://doi.org/10.1016/j.engfracmech.2015.06.030. URL http://www.sciencedirect.com/science/article/pii/S0013794415002933.

[25] Paul M. Darbyshire. 3d visualisation of tumour-induced angiogenesis using the cuda programming model and opengl interoperability. *Journal of Cancer Treatment and Research*, 3:56 – 65, 2015. ISSN 0013-7944. doi: 10.11648/j.jctr.20150305.11. URL http://www.sciencepublishinggroup.com/journal/paperinfo?journalid=654&doi=10.11648/j.jctr.20150305.11.

[26] M. A. Crisfield. Snap-through and snap-back response in concrete structures and the dangers of under-integration. *International Journal for Numerical Methods in Engineering*, 22(3):751–767, 1986. ISSN 1097-0207. doi: 10.1002/nme.1620220314. URL http://dx.doi.org/10.1002/nme.1620220314.

[27] I.M. Gitman, H. Askes, and L.J. Sluys. Representative volume: Existence and size determination. *Engineering Fracture Mechanics*, 74(16):2518 – 2534, 2007. ISSN 0013-7944. doi: https://doi.org/10.1016/j.engfracmech.2006.12.021. URL http://www.sciencedirect.com/science/article/pii/S0013794406004772.

[28] INTEL. Sparse blas csr matrix storage format. URL https://software.intel.com/en-us/mkl-developer-reference-fortran-2018-beta-sparse-blas-csr-matrix-storage-for